https://ntrs.nasa.gov/search.jsp?R=19690002805 2020-03-12T05:56:24+00:00Z

General Disclaimer

One or more of the Following Statements may affect this Document

- This document has been reproduced from the best copy furnished by the organizational source. It is being released in the interest of making available as much information as possible.

- This document may contain data, which exceeds the sheet parameters. It was furnished in this condition by the organizational source and is the best copy available.

- This document may contain tone-on-tone or color graphs, charts and/or pictures, which have been reproduced in black and white.

- This document is paginated as submitted by the original source.

- Portions of this document are not fully legible due to the historical nature of some of the material. However, it is the best reproduction available from the original submission.

Produced by the NASA Center for Aerospace Information (CASI)

ELECTRO-OPTICAL SYSTEMS, INC.
A XEROX COMPANY
PASADENA, CALIFORNIA 91107 • 213/351-2351

N69-12136

FACILITY FORM 602

(ACCESSION NUMBER)	(THRU)
179 (PAGES)	1 (CODE)
CR-97810 (NASA CR OR TMX OR AD NUMBER)	03 (CATEGORY)

RECEIVED
NASA STI FACILITY
INPUT BRANCH
DEC 1968

Final Report

THERMIONIC RESEARCH AND DEVELOPMENT PROGRAM

Prepared for
National Aeronautics and Space Administration
Jet Propulsion Laboratory
California Institute of Technology
4800 Oak Grove Drive
Pasadena, California

Contract NAS7-514

EOS Report 7118-Final 25 September 1968

Prepared by
A. E. Campbell
D. L. Jacobson

Approved by

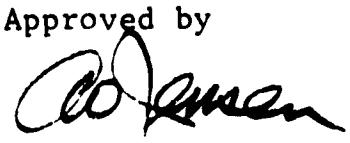

A. O. Jensen, Manager
Electro-Optical and
Solid State Technology Division

ELECTRO-OPTICAL SYSTEMS, INC.
A XEROX COMPANY

ACKNOWLEDGMENTS

The authors of this report would like to thank the following for their contributions and assistance throughout this program and in the preparation of this final report: Dr. A. O. Jensen, Dr. D. G. Worden (now at North Dakota State University), Dr. R. A. Missman, and Mr. R. W. Hamerdinger.

This program was technically directed for NASA by Mr. O. Merrill of the Jet Propulsion Laboratory, California Institute of Technology, Pasadena, California.

CONTENTS

CONTENTS (contd)

ILLUSTRATIONS

ILLUSTRATIONS (contd)

ILLUSTRATIONS (contd)

ILLUSTRATIONS (contd)

SECTION 1

INTRODUCTION

1.1 REVIEW OF PROGRAM OBJECTIVES

This is the final report of a research program to improve the output performance of low emitter temperature, cesium-vapor thermionic converters. The program was conducted by Electro-Optical Systems, Inc., for NASA Headquarters under contract NAS7-514 and covered the period from 15 July 1966 to 15 January 1968.

The major objectives of the program were: (1) to measure the vacuum emissions of several candidate electrodes and examine their surface structures as a function of various preparation techniques, (2) to select electrodes from these investigations and demonstrate their thermionic performance in test vehicles as well as converters, and (3) to analyze all these data in a theoretical study for the purpose of acquiring a better understanding of thermionic converter physics.

Task I involved the design and fabrication of two ultrahigh vacuum instruments in which electron emission (vacuum), surface uniformity, secondary recrystallization, and electrode preparation techniques of planar emitters could be measured or evaluated. One instrument, the EOS thermionic electron emission microscope, was modified to permit high magnification viewing of electrode surface detail. The modification also included the design and installation of a Faraday cage for work function evaluation of individual grains and the microstructure within the grains. Task I included a limited metallurgical investigation of crystallographic orientation, material purity and density, and surface structure.

Task II comprised the fabrication and operation of variable parameter test vehicles for the purpose of measuring cesium vapor converter output performance at low emitter temperatures. These vehicles were operated at emitter temperatures from 1300°C to 2200°C, collector temperatures from 650°C to 1000°C, and cesium reservoir temperatures from 290°C to 500°C. The interelectrode spacings were varied from 0.0001 to 0.026 inch and were accurately reproducible over hundreds of hours of testing time. Two variable parameter test vehicles were operated, and parametric studies were conducted employing a vapor-deposited rhenium emitter/vapor-deposited rhenium collector (selected from Task I) and a polycrystalline rhenium emitter/molybdenum collector. Two planar converters were fabricated and tested to demonstrate performance of the vapor-deposited rhenium system and to correlate research data from the test vehicles.

Task III encompassed the interpretation of experimental results, particularly regarding the variable parameter test vehicle operation. The very-close spaced, cesium vapor diode was analyzed and the results compared with the experimental data. Theoretical studies also disclosed that an arc-mode converter obeys the laws of similarity to operate at optimum output.

1.2 REVIEW OF PROGRAM ACCOMPLISHMENTS

Vapor-deposited rhenium was selected as the principal electrode material for investigation. This selection was based on two considerations: First, the deposition process lends itself to the fabrication of complex geometries or shapes of the refractory metals, and second, the preferred orientation of vapor depositions results in a higher bare work function. Figure 1 illustrates the significance of a high bare work function. The relationship suggests the basic thesis that increased bare work function values result in decreased minimum cesiated work function values and implies higher thermionic converter output. EOS has provided

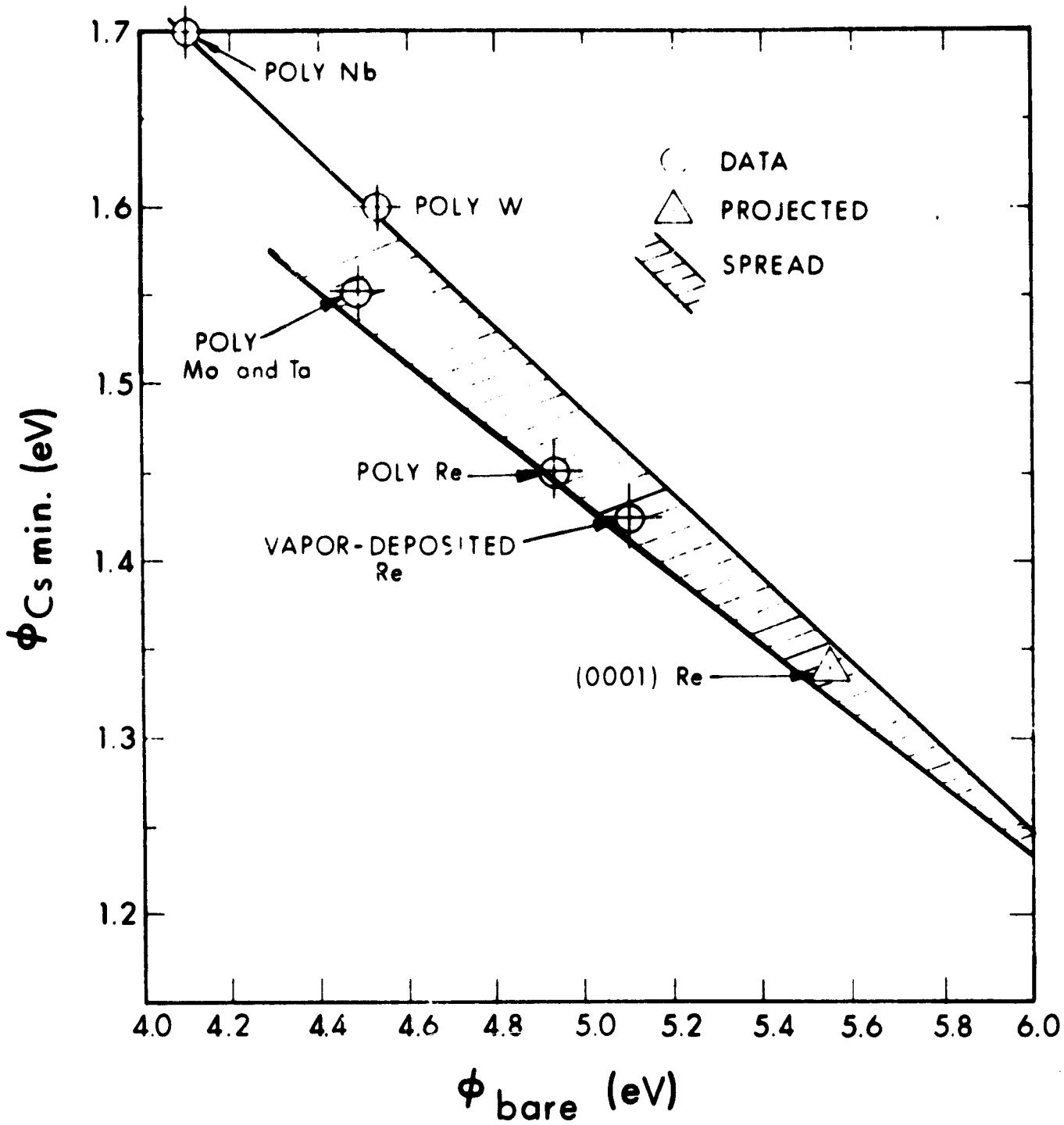

Figure 1. Empirical Relationship Between Bare Work Function and Minimum Cesiated Work Function

50

experimental proof for this thesis in the case of polycrystalline rhenium (4.95 eV) and molybdenum (4.5 eV). However, for polycrystalline rhenium (4.95 eV) and vapor-deposited rhenium (5.15 eV) the bare work function values are sufficiently close to be within the overall data spread and may not provide any significant difference in minimum cesiated work function.

The operation of the thermionic electron emission microscope was the highlight of the materials investigation task. It provided simultaneous emission images and emission measurements that were heretofore unavailable to the field of thermionics.

The operation of the variable parameter test vehicles and thermionic converters established several important results:

- Maximum power output of an arc-mode converter occurs at a cesium pressure-interelectrode spacing, or pd, product of 16 ±0.8 torr-mils independently of the emitter temperature, emitter work function, collector work function, or current level.
- A low work function collector provides increased voltage and power output from a thermionic converter.
- The thermionic converter power output from vapor-deposited rhenium is within the data spread of polycrystalline rhenium.

Another program highlight was the continued high reliability of fabricating converter hardware. The method of fabrication is twofold: First, all subassemblies, including metal-ceramic seals, are brazed and leak checked; second, the subassemblies are electron-beam welded together to form the final assembly. Since welding, especially electron-beam welding, provides maximum control and reproducibility among the joining processes, this two-step method of fabrication has resulted in greatly improved converter technology and performance.

SECTION 2

ELECTRODE MATERIALS INVESTIGATION (TASK I)

An investigation of vapor-deposited rhenium electrodes was conducted to evaluate thermionic properties, such as bare work function and surface uniformity. Vapor-deposited rhenium was an a priori selection, since in the vapor deposition form, it was presumed to have the highest bare work function among the common refractory metals. Polycrystalline rhenium was selected as a substrate for the deposited layer of rhenium to avoid incompatibility of dissimilar materials during high temperature operation for prolonged periods of time.

The three phases of investigation were: (1) a metallurgical study which included metallographic, spectrographic, and X-ray analyses; (2) a vacuum emission study of several emitters; and (3) an examination of surface uniformity via a thermionic emission microscope. Combined, these studies offer a rather complete investigation of vapor-deposited rhenium.

2.1 METALLURGICAL INVESTIGATION OF ELECTRODE MATERIALS

The ultimate performance of any thermionic device is closely associated with the physical and chemical properties of the electrode materials. Therefore, detailed studies were made to ascertain these essential properties. Metallographic, spectrographic, and X-ray analyses of vapor-deposited and polycrystalline rhenium have been performed to evaluate the properties of these materials.

Quantitative spectrographic analyses of both polycrystalline and vapor-deposited rhenium showed that the purity is very high and nearly the same for each. X-ray analyses showed that vapor-deposited rhenium has a very strong texture with the basal plane oriented parallel to the electrode surface, indicating that work function enhancement should result from the vapor deposition process. Metallographic examinations of polycrystalline and vapor-deposited rhenium have revealed the existence and probable cause of surface irregularities. It has been found experimentally that a high metallurgical polish results in removal of the irregularities and that they do not reappear with subsequent chemical or thermal treatments. Metallurgical examinations of electro-etched vapor-deposited rhenium indicated that etching does not significantly increase the amount of high work function material at the surface by preferentially attacking low work function planes exposed at the surface. This observation is supported by crystal symmetry arguments in comparing the cubic and hexagonal close-packed structures.

The density of the vapor-deposited rhenium is essentially the same as that of polycrystalline rhenium. An ultrasonic scan of 0.5 mil resolution revealed no voids across the interface of vapor-deposited rhenium on a polycrystalline substrate. Metallographic examination (5-10μ resolution) of the interface substantiated this observation.

2.1.1 SPECTROGRAPHIC ANALYSIS

Cleveland Refractory Metals,* performed a complete quantitative spectrographic analysis of both polycrystalline rhenium and vapor-deposited rhenium. This was the only complete and accurate analysis that was found. The rhenium was dissolved from the surface of a sample, one side of which was vapor-deposited and the other polycrystalline. A solution from each side was subsequently evaporated in a porous electrode and sparked. The total analysis is given in Table I.

*Analysis performed at Chase Brass & Copper Company Research and Development Laboratory, Waterbury, Connecticut.

TABLE 1

SPECTROGRAPHIC ANALYSIS OF VAPOR-DEPOSITED ("V") RHENIUM AND POLYCRYSTALLINE ("P") RHENIUM, REPORTED IN PARTS PER MILLION. ND INDICATES NONE DETECTED.

Element	"V"	"P"	Element	"V"	"P"	Element	"V"	"P"
Ag	ND	ND	Fe	53	51	Pb	ND	ND
Al	< 1	< 1	K	< 1	< 1	Si	< 1	< 1
B	ND	ND	Li	ND	ND	Sn	ND	ND
Be	ND	ND	Mg	< 1	< 1	Ti	ND	ND
Bi	ND	ND	Mn	ND	ND	V	ND	ND
Ca	< 1	< 1	Mo	< 1	10	W	ND	ND
Cd	ND	ND	Na	< 1	< 1	Zn	ND	ND
Co	ND	ND	Nb	ND	ND	Zr	ND	ND
Cr	5	< 1	Ni	7	3	Th	ND	ND
Cu	< 1	< 1	P	ND	ND			

With the exception of Cr, Mo, Ni, the analysis shows that the purity of the vapor-deposited rhenium is not significantly different from the polycrystalline rhenium substrate upon which it was deposited.

2.1.2 SURFACE TEXTURE

To ascertain the degree of preferred orientation of vapor-deposited rhenium, a direct method utilizing a Geiger counter X-ray spectrometer (Ref. 1) was used. An X-ray beam reflected from the sample surface was measured for a particular crystallographic plane as the specimen was rotated about an axis defined by the intersection of the sample surface and the diffractometer axis. The variation of density of a particular plane as a function of angle, measured from the surface normal, indicated a strong texture.

Two vapor-deposited rhenium samples were evaluated: sample I in the "as-received" vapor-deposited condition; sample II with a prior vacuum outgassing at 2300°C for three hours.

Table II shows the results of a simple symmetrical scan of the sample surface indicating the intensity of the various reflections. These results show a very strong texture with the (002) planes parallel to the surface, where (002) is the basal plane in abbreviated Miller-Bravais symbols (Ref. 2).

Table III shows the variation of density of (002) planes as a function of angle, measured from the surface normal. Table III may be analyzed by assuming that the intensity is proportional to the volume of diffraction material, and calculating the volume of material within a given angle.

TABLE II

SURFACE SCAN INTENSITIES, I, NORMALIZED TO (002) PLANE

Sample I		Sample II	
hkl	I	hkl	I
100	3	100	5.5
002	100	002	100
101	25	101	4.4
102	6	102	2.2
110	0.5	110	~ 0
103	10	103	2.7
112	2	200	~ 0
201	~ 0	112	~ 0
004	10	201	~ 0
104	1	004	4.4
203	~ 0		
210	~ 0		

Cu Kα radiation used

TABLE III

SURFACE VARIATION OF SCAN INTENSITIES OF (002) PLANES NORMALIZED TO ZERO DEGREE TILT ANGLE

Sample I		Sample II	
Tilt Angle	I	Tilt Angle	I
0	100	0	100
5	73	5	95
10	35	10	65
15	16	15	38
20	10	20	22
25	6	25	14
30	4	30	4
35	3	40	0.4
40	2.5		
50	2		

Cu Kα radiation used

In sample I, 39.8 percent of the material is oriented with the (002) plane parallel to the surface and 82.8 percent is within 10 degrees of the surface. Sample II contains 29.6 percent with (002) orientation parallel to the surface and 77 percent within 10 degrees. The heat treatment caused only a 5.8 percent decrease in (002) surface oriented material over a 10 degree tilt angle. This is a good indication that vapor-deposited rhenium retains a high degree of (002) texture through high temperature outgassing.

The experimental analyses for this investigation were performed by Prof. C. R. Barrett at the Stanford University Materials Science Department in Palo Alto, California.

2.1.3 METALLOGRAPHIC EXAMINATION

Vapor-deposited rhenium electrode surfaces were subjected to various mechanical and thermal treatments with subsequent work function measurements in an effort to determine the relationship of surface condition to thermionic performance. The presence of surface irregularities on vapor-deposited rhenium have been observed and the basic question arose as to whether the irregularities were inherent to the vapor deposition process or were a result of subsequent preparation or treatment. Figure 2 is a photomicrograph of vapor-deposited rhenium, sample II. The surface was first ground flat with a diamond wheel, then given a diamond lapping, and then diamond scribed with a set of orthogonal axes which were used for identification and location of grains on the sample surface. The sample was then vacuum outgassed at 2300°C for 2 hours and operated at 1900°C for 60 hours. The surface irregularities are evident on either side of the scribe mark. It can be seen that the scribing operation work-hardened the surface, which subsequently recrystallized when the emitter was brought to the annealing temperature. It is interesting to note that this abrasion exposed a surface essentially free of irregularities.

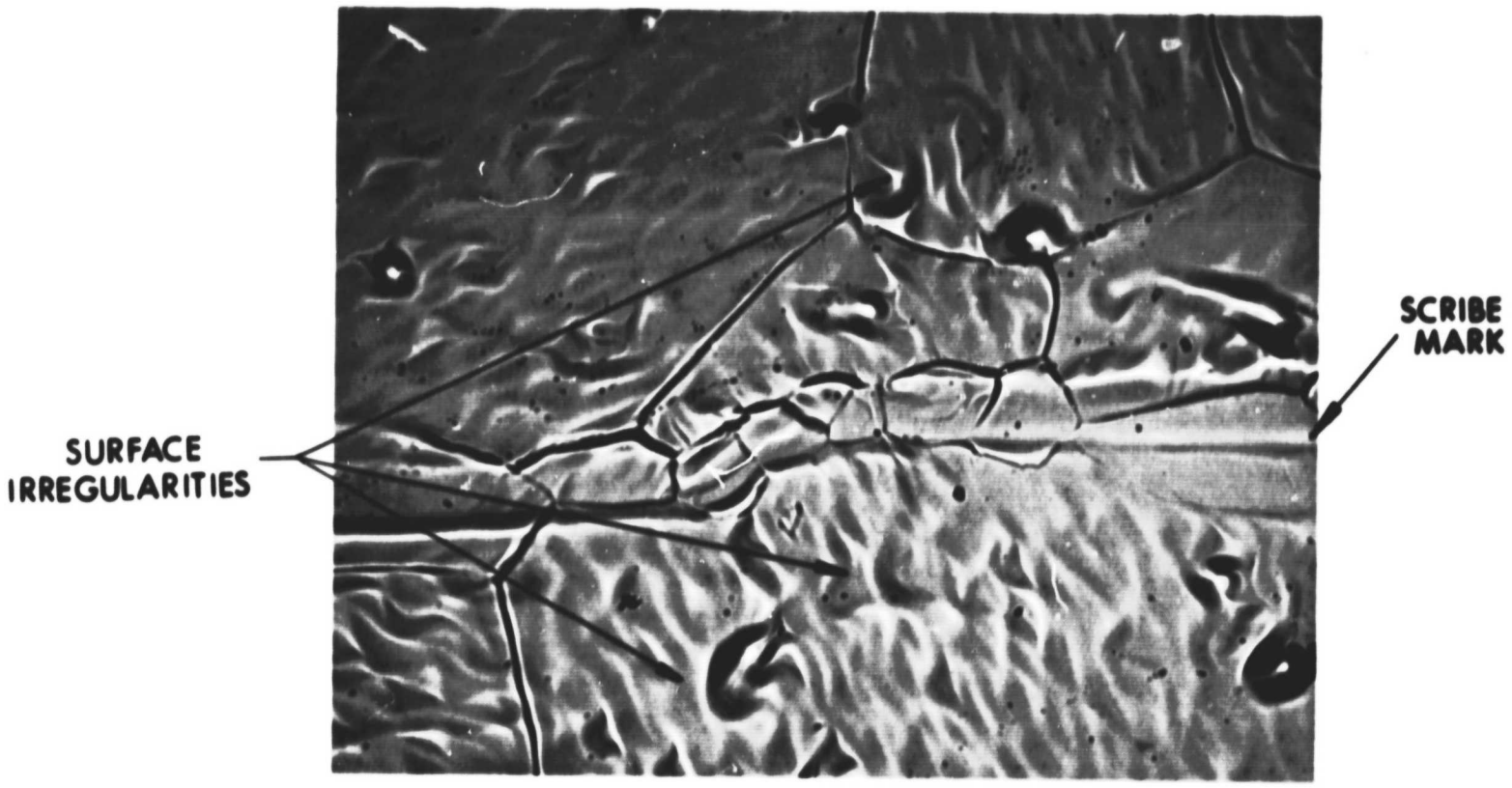

Figure 2. 500X Photomicrograph of Diamond Lapped Vapor-Deposited Rhenium, Sample II, After 2 Hours of Vacuum Outgassing at 2300°C and 60 Hours of Operation at 1900°C

The vapor-deposited rhenium surface was then polished to a mirror finish with Linde A, B, and C alumina powders on a Lapmaster. The surface was free of scratches and was fixtured to prevent rounding of the edges. After polishing, the sample was chemically cleaned in hydrochloric acid and in Oakite, and then boiled in distilled water. The sample was vacuum outgassed at 2300°C for 2 hours and operated at 1900°C for 58 hours. In Fig. 3 the resulting surface gives evidence of the removal of surface irregularities. Some grain growth is displayed near grain boundary intersections. The results of the polishing and annealing treatment indicate that the surface irregularities are not due to thermal etching, as first suspected, but rather are a condition remaining from the relatively coarse diamond lapping in the first process.

The surface irregularities described above have been observed on polycrystalline rhenium and have been removed through subsequent fine polishing in the same manner as that described for vapor-deposited rhenium.

Electro-etching was then performed, first on the vapor-deposited rhenium, to determine the effect on surface irregularities. Figure 4 is a photomicrograph (500X) of the diamond lapped, vacuum outgassed vapor-deposited rhenium surface before electro-etching. Surface irregularities are present as before. The sample was vacuum outgassed at 2300°C for 2 hours, and then operated at 1900°C for 40 hours.

Sample II was electro-etched with the vapor-deposited rhenium as the anode in an electrolytic solution of 350 ml perchloric acid, 175 ml methanol, and 50 ml butoxyethanol. A rhenium rod was used as a cathode. A potential of between 2 to 5 volts was used, with a current density of about 0.1 A/cm^2. The electrolytic bath was stirred constantly and the temperature was maintained at about 20°C. Figure 5 is

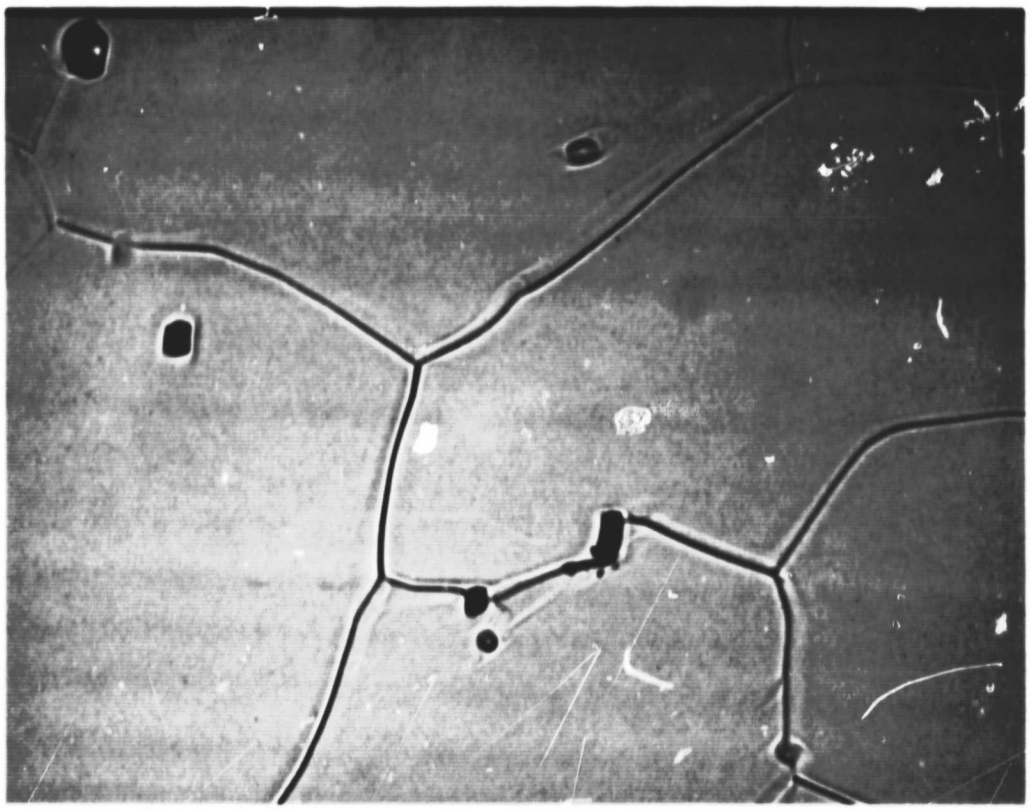

Figure 3. 500X Photomicrograph of Fine-Polished, Vapor-Deposited Rhenium after 2 Hours of Vacuum Outgassing at 2300°C and 58 Hours of Operation at 1900°C

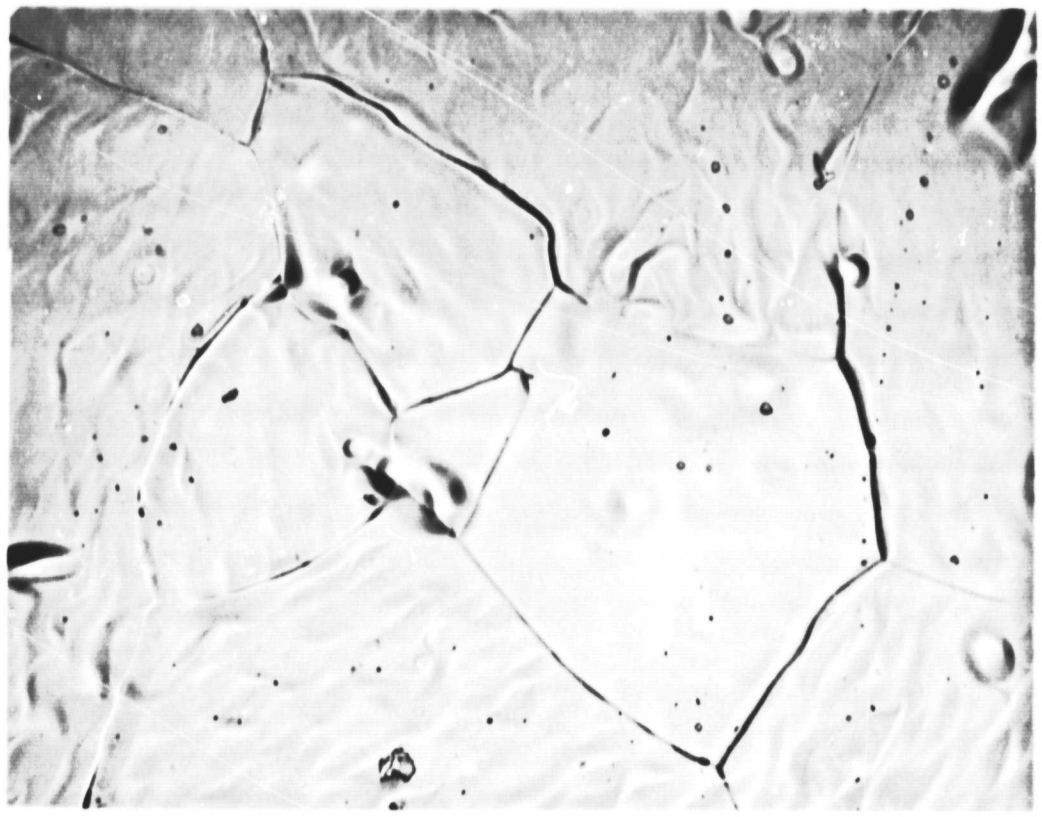

Figure 4. 500X Photomicrograph of Rough Diamond Lapped Vapor-Deposited Rhenium after 2 Hours of Vacuum Outgassing at 2300°C and 40 Hours of Operation at 1900°C

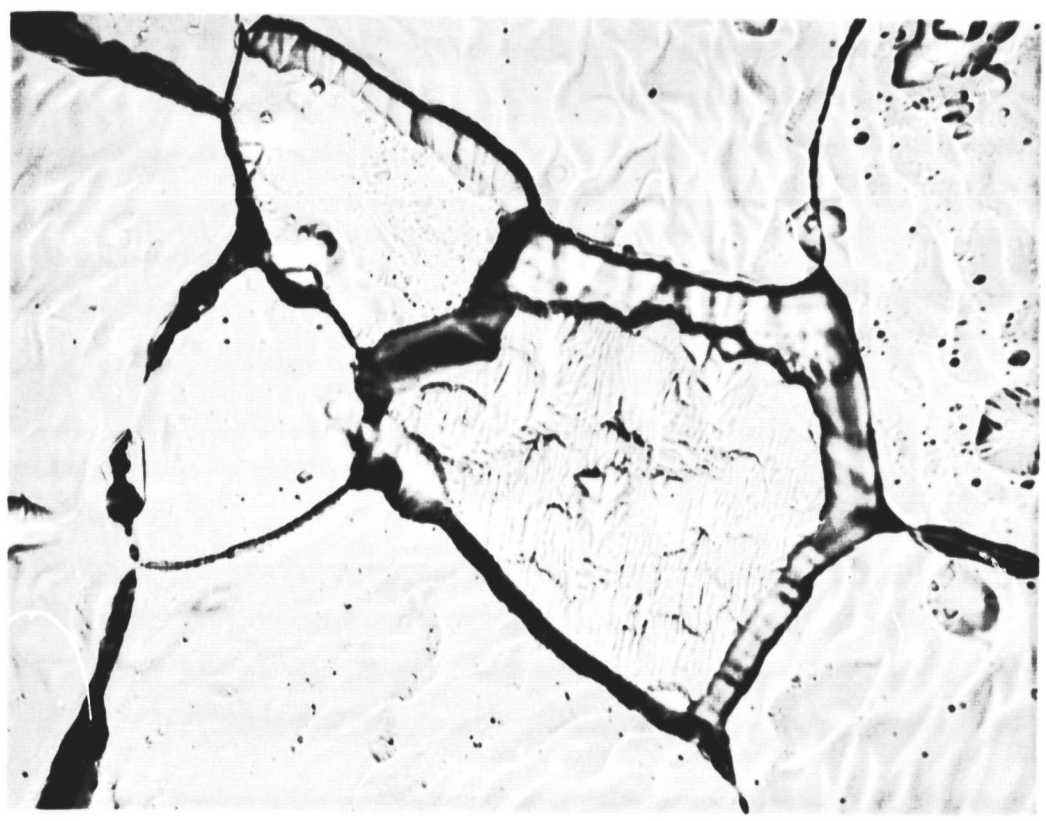

Figure 5. 500X Photomicrograph of Rough Diamond Lapped Vapor-Deposited Rhenium after Electroetching (see Fig. 4)

a photomicrograph of this surface after the electro-etching operation. As expected, the removal of rhenium from the surface was not uniform. This process transformed the surface, which was initially smooth in appearance, to a jagged surface bound by sharp edges. Grain boundaries were excessively etched and etch pits were observed. The relative heights of the grains changed, some well below those of neighboring grains. It can be seen in Fig. 5 that the etching process did not remove the surface irregularities.

Figure 6 is a photomicrograph showing the results of electro-etching a previously fine-polished, vapor-deposited rhenium surface. The sample shown in Fig. 6 was etched for a longer period of time than that of Fig. 5. This procedure shows that the surface irregularities do not originate either by electro-etching or vacuum heat treatment when the surface has had a prior fine polish.

The main purpose of the electro-etching process was to determine if the overall work function of the vapor-deposited material could be enhanced by preferential removal of material with low work function crystallographic planes oriented at the surface. Since rhenium is a hexagonal close-packed material, the basal plane when parallel to the sample surface exhibits the highest possible work function. Since the basal plane is the densest atomically, it will resist the attack of an etchant more than a less dense crystallographic plane. H. F. Webster (Ref. 3) has shown that in materials with cubic symmetry, etching can, in essence, bare a uniform crystallographic plane, the densest plane, on a single grain. Because of the symmetry inherent in the cubic system this uniformity of a particular crystallographic plane is possible. For example, in a body centered cubic material with (110) surfaces being the most dense, the minimum symmetry elements are four 3-fold rotation axes. In a hexagonal material with the (0001), or basal plane, being the most dense, the only symmetry element reproducing the (0001) plane

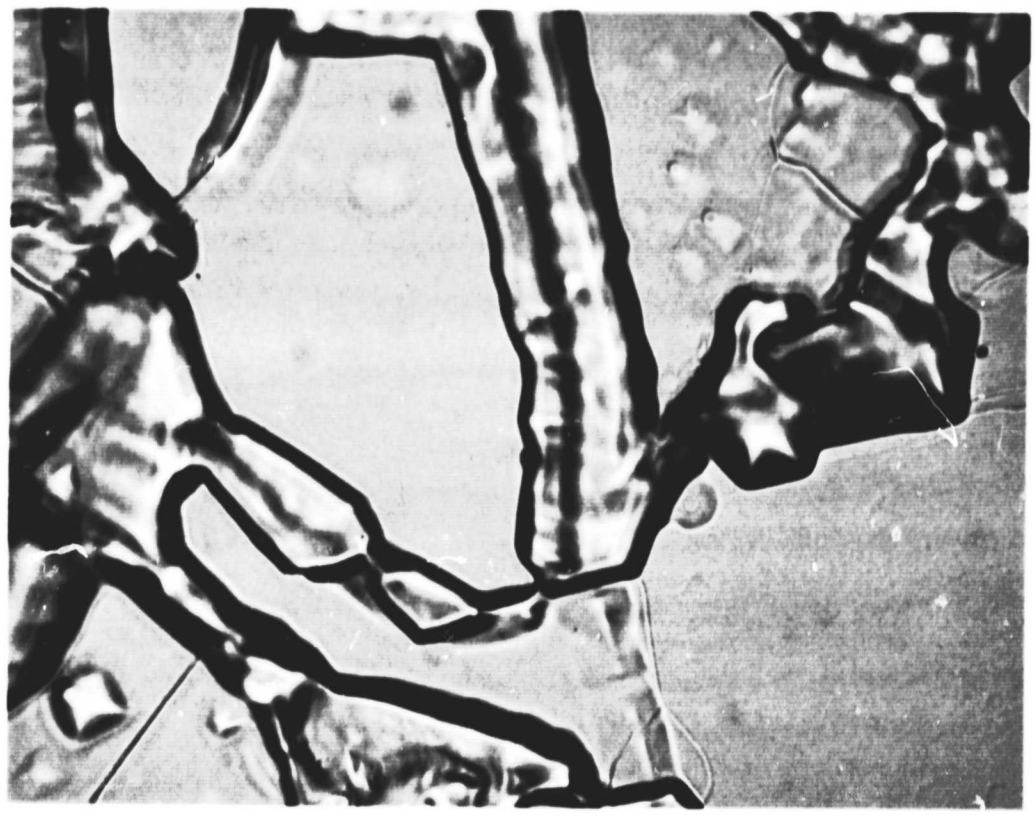

Figure 6. 500X Photomicrograph of Fine-Polished and Electro-Etched Vapor-Deposited Rhenium

is one 2-fold rotation axis. Thus, it is evident that etching a hexagonal close-packed material will not be as successful as etching a cubically symmetric material in revealing more density packed planes. Figure 7 is a photomicrograph taken at 100X of the same sample as shown in Fig. 6. Little surface faceting is in evidence, but etch pits in the grains are clearly seen. Surface facets should reveal the crystallographic structure. However, etching of rhenium appears mainly to increase the total surface area through the removal of material at the grain boundaries.

2.2 VACUUM EMISSION TEST VEHICLE

The second phase in this electrode materials investigation was devoted to measuring the vacuum thermionic emission from vapor-deposited and polycrystalline rhenium. These measurements were performed in a guard ringed, planar emission vehicle operated in a high vacuum environment. From the emission measurements, average Richardson and effective bare work function values were computed.

The following paragraphs describe the emission test vehicle design, the equipment and methods employed for emission measurements, and the sources of experimental error. A summary of average effective work function values for vapor-deposited and polycrystalline rhenium is contained in Subsection 2.2.2. Finally, there is a discussion of various electrode processing techniques, such as electro-etching, lapping, high temperature recrystallization, etc., and their influence on the bare work function value of vapor-deposited rhenium.

2.2.1 VACUUM EMISSION TEST VEHICLE DESIGN AND OPERATION

The vacuum emission test vehicle consists of four major components: emitter, electron bombardment heater, collector, and guard ring. Figure 8 shows these components in relation to each other.

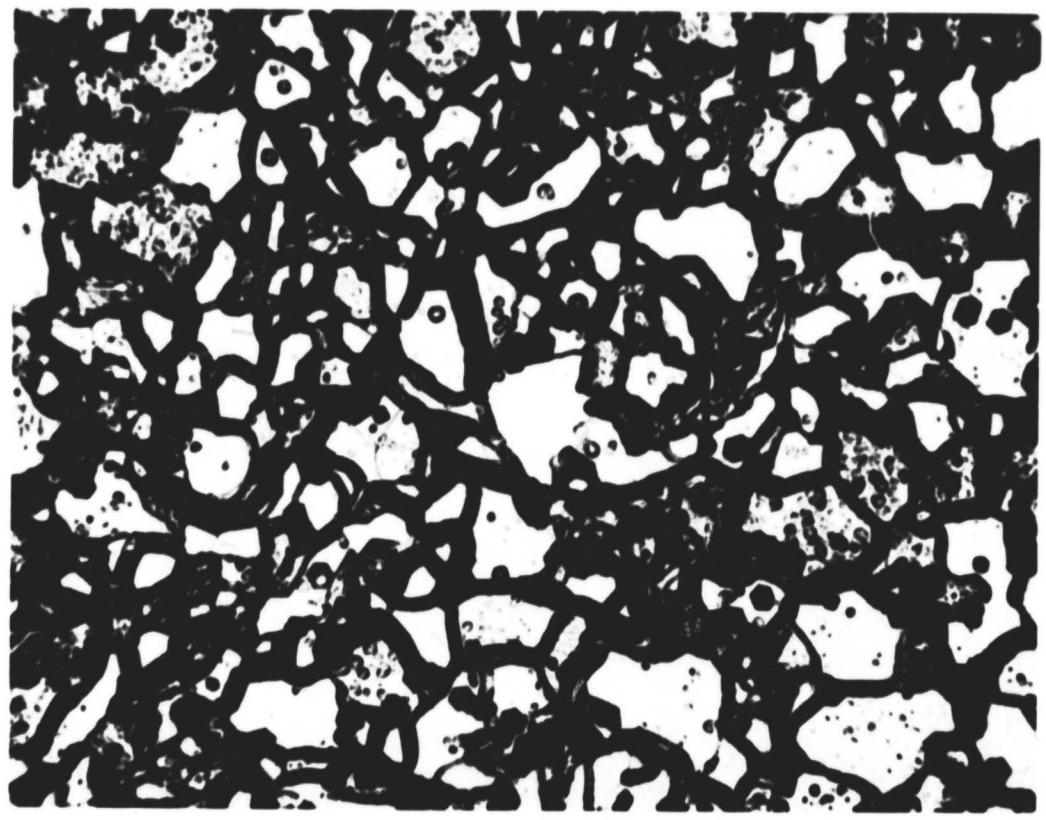

Figure 7. 100X Photomicrograph of Polished and Electro-Etched Vapor-Deposited Rhenium (see Fig. 6)

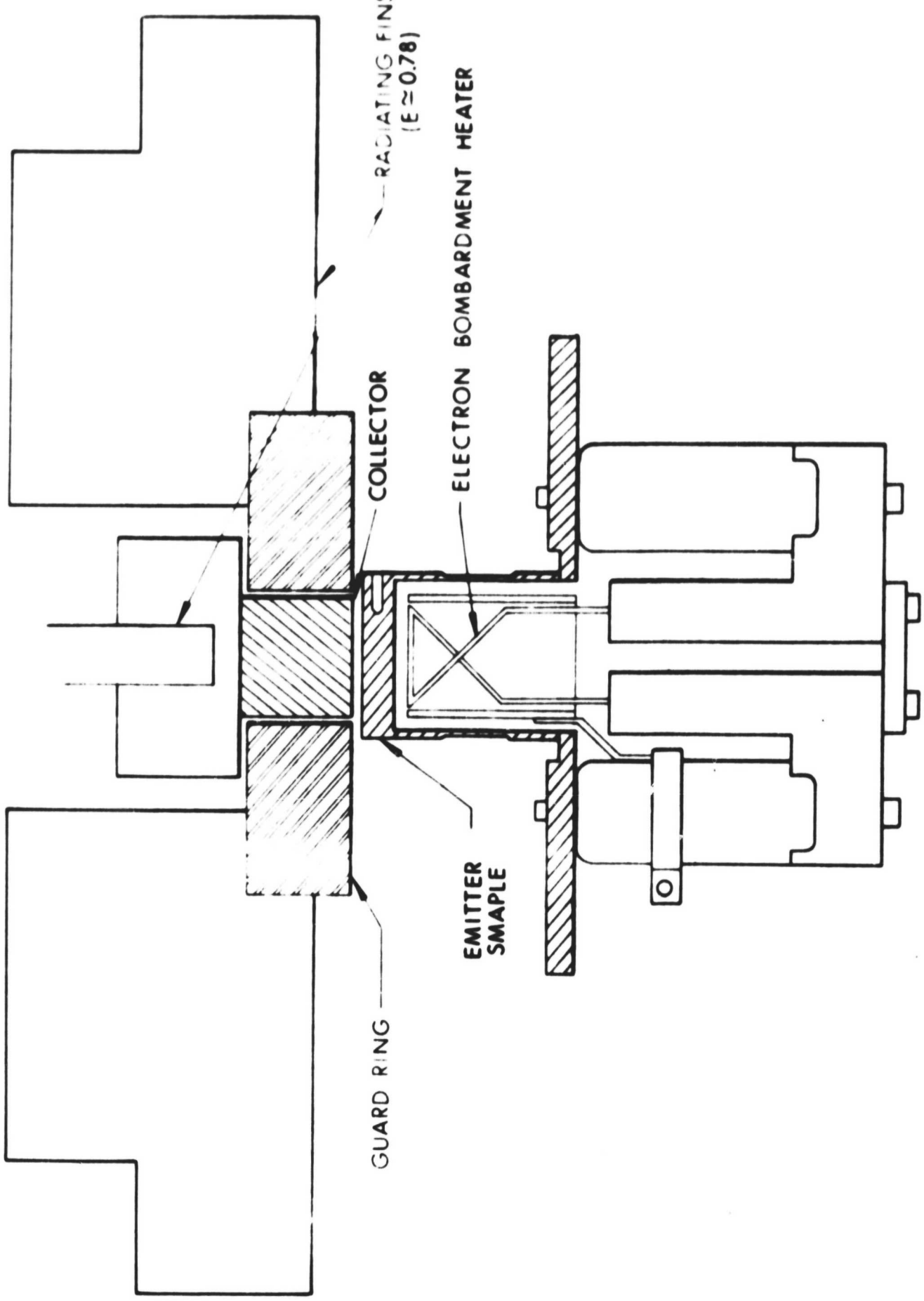

Figure 8. Schematic of Vacuum Emission Test Vehicle

The emitter and electron bombardment heater is an integral unit which may be removed and reinstalled by a simple bolting arrangement. The emitter can be heated to a temperature of 2400°K without the supporting base temperature exceeding 700°K.

Emitter temperatures are measured with a micro-optical pyrometer focused on a 10:1 hohlraum located in the side of the sample and parallel with the emitting surface. The emitter is electron-beam-welded onto a tubular support structure which is heat-choked to minimize heat conduction losses. The tube, in turn, is vanadium-brazed into a molybdenum plate which serves as a holding base for the sample, as well as the electron bombardment heater. Figure 9 shows the collector and guard ring mounted in a stainless steel holding fixture. The molybdenum collector is mounted parallel to the emitter at an ambient spacing of 0.040 ±0.001 inch and intercepts the electron emission from the central 1.83 square centimeters of the 4.0 square centimeter emitting surface. The collector structure includes a radiator fin of approximately 80 square centimeters. The fin is coated with Rokide "C" to adjust its emittance to 0.78. The collector is heated directly by radiation from the emitter and by collected electrons dissipating energy acquired from the applied field between emitter and collector. At the highest voltage and highest current levels, the collector thermal input is over 50 watts which is rejected by the radiating fin. The collector surface operates at temperatures of less than 500°C.

High purity standoff ceramic insulators (AL 995), precision ground in length and diameter to within 0.0003 inch, are used to electrically insulate and accurately position the collector assembly with respect to both the emitter and guard ring. The molybdenum guard ring is concentric to the collector within 0.0015 inch and serves as a guard for the collector surface as well as the collector body. The guard ring, which receives heat input in the same manner as the collector, also has radiator fins.

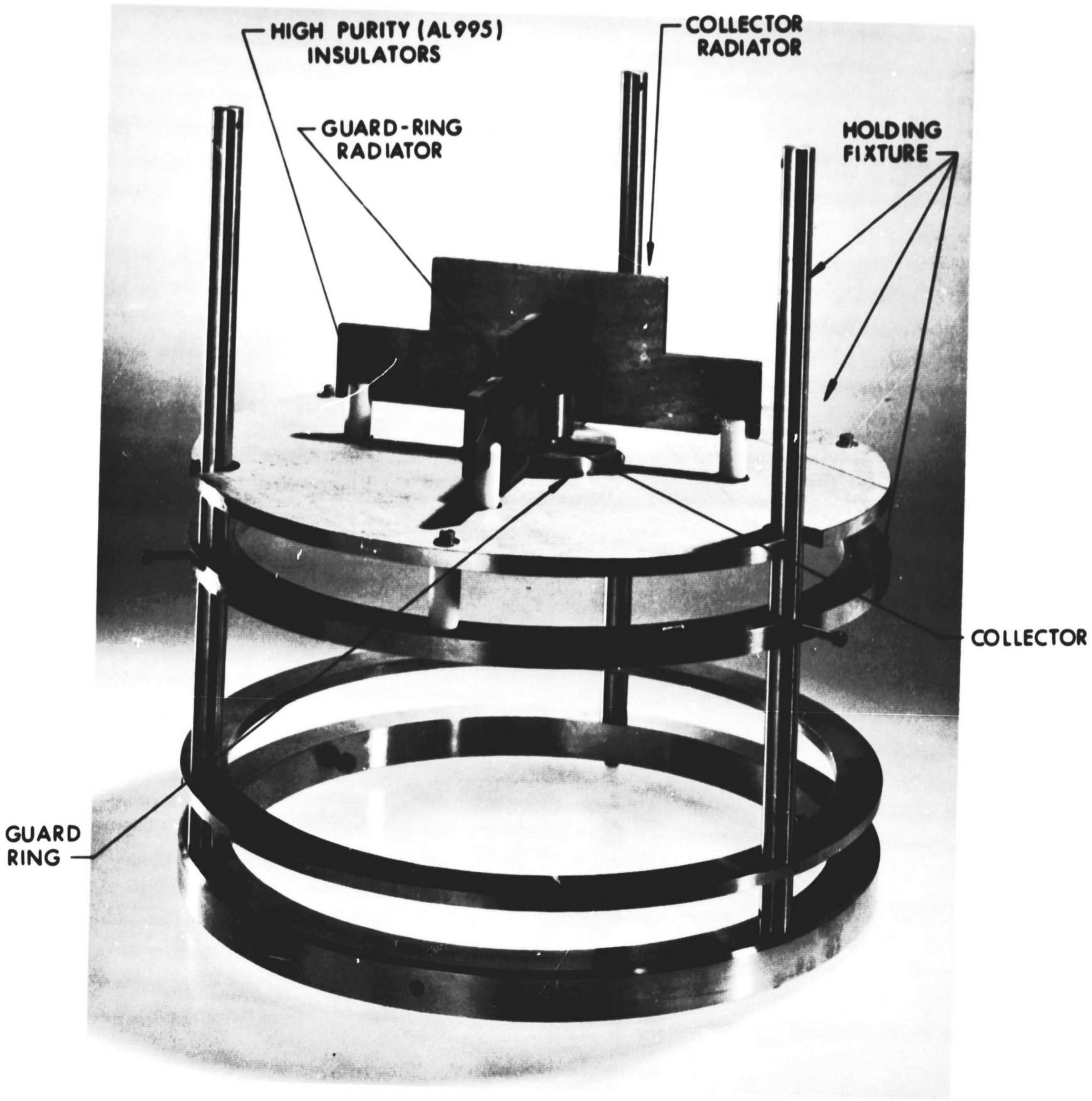

Figure 9. Vacuum Emission Vehicle

Figure 10 is a schematic of the electrical test setup for the vacuum emission vehicle. A Keithly 610R micro-microammeter measures collector current. It has an accuracy of 3 percent from 3 amperes to 10^{-10} ampere and 4 percent for 10^{-10} to 10^{-13} ampere. A Boonton 95A micro-microammeter (4 percent accurate at 10^{-13}), measures the current flow between the collector and guard ring. In operation this current flow is maintained two to three decades below the current level measured in the collector circuit. For practical purposes, the potential of the guard ring under these conditions is considered to be equal to that of the collector. All emission measurements were taken in a vacion pumped environment at pressures of 4 to 9 x 10^{-8} torr after the holding fixture, emission vehicle components, and vacuum bell jar were baked out. Two Fluke model 408B power supplies were used to maintain and adjust the potentials of the collector and guard ring. The output of these supplies is adjusted by a precision Kelvin Varley divider, providing an accuracy of 1/4 percent and a repeatability of 0.1 percent.

The emitter temperature measurement is repeatable, by experienced operators, within $\pm 3^{\circ}K$; however, the absolute determination of temperatures in the $2000^{\circ}K$ to $2500^{\circ}K$ range is $\pm 7^{\circ}K$, a value consistent with the Bureau of Standards certification of strip-filament lamps (Ref. 4). EOS micro-optical pyrometers have been continuously checked and calibrated against these lamps for four years without any detectable variation, as displayed in Fig. 11. In addition, corrections for optical transmission loss through the Pyrex viewing windows were determined over the temperature range, as indicated in Table IV.

The combined experimental accuracy for determining work function values derived from the experimental measurements of electron current, emitter temperatures, emission area and applied field is estimated to be a maximum ± 0.04 eV.

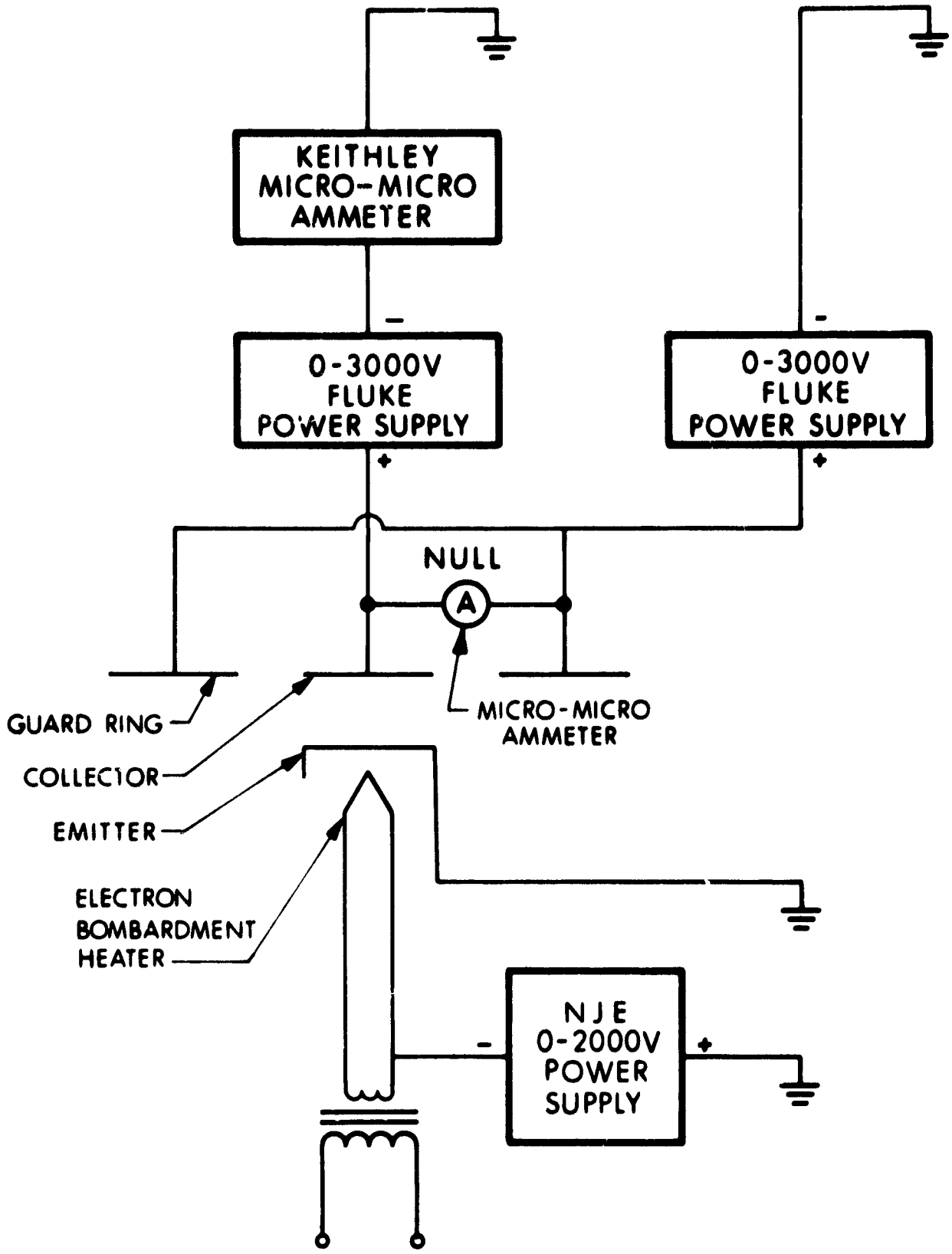

Figure 10. Schematic of Electrical Circuit for Vacuum Emission Measurements

27484

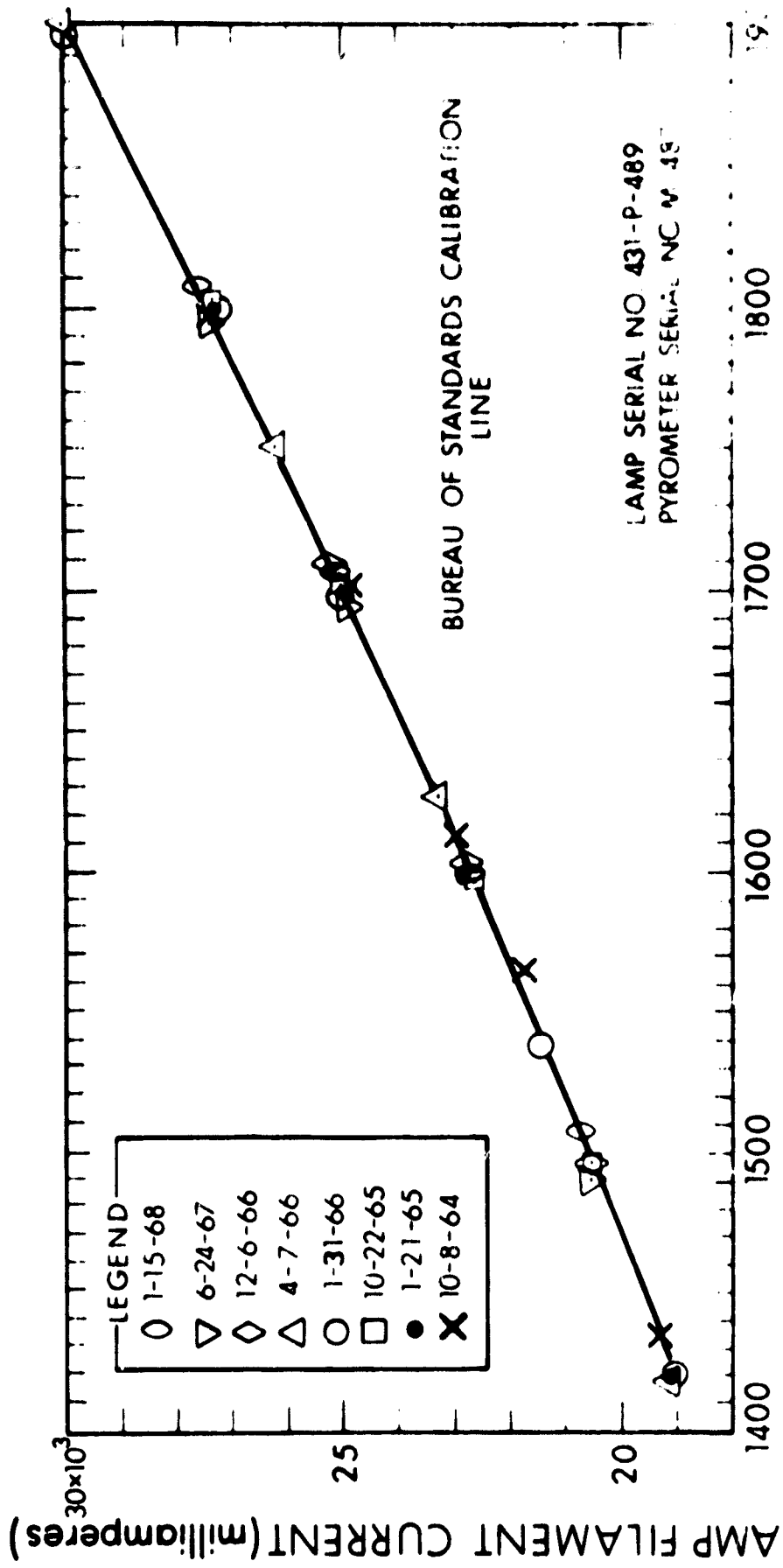

Figure 11. Calibration Record of Micro-Optical Pyrometer Used for Vacuum Emission and Converter Performance Testing

TABLE IV

WINDOW TRANSMISSION CORRECTIONS FOR
MICRO-OPTICAL PYROMETER MEASUREMENTS

True Temperature (^{o}C)	ΔT (^{o}C) (Transmission Loss Through 1/4 in. thick Pyrex)
1227	13
1427	16
1627	19
1905	23

2.2.2 EFFECTIVE WORK FUNCTION (A = 120 amp/cm^2 - $^{o}K^2$) OF VAPOR-DEPOSITED AND POLYCRYSTALLINE RHENIUM

Electron emission measurements were obtained from several emitters in the temperature range from 1700^{o}K to 2400^{o}K. At each temperature the emission was measured as a function of the applied voltage between the emitter and collector to establish the field-dependent Schottky region. Applied voltages from 1 volt to 3 kilovolts were used to obtain these measurements, although it was found that the Schottky line could be adequately determined at applied voltage levels of less than 1 kilovolt. Since the Schottky line is used to obtain the field-free, or saturated, emission from which the work function is determined, it was critically important to maintain a constant emitter temperature and electric field during the measurements. Consequently, before each set of data was taken, all components of the emission vehicle were allowed to reach steady-state temperature. In this manner thermal expansion of the emitter subassembly, collector subassembly, and mounting fixture was held constant to establish a constant interelectrode spacing and applied field. The spacing was measured, at temperature, by a positive method accurate to within 0.0003 inch.

Figure 12 is a Schottky plot of electron emission from vapor-deposited rhenium sample I. The solid line is drawn through the experimental data points and results in a measured slope within 1.7 percent of the theoretically predicted value. Other Schottky plots yielded similar agreement between measurements and theory....the average among 20 such plots was 2.1 percent. The noticeably slight periodic-type deviation of the data points about the solid line was examined in more detail, as shown in Fig. 13 and found to be more pronounced at lower emission levels. The data is in general agreement with quantum-theory predictions (Refs. 5 and 6) and other recent experimental investigations by Coomes and others (Ref. 7).

With extrapolated or zero-field saturated emission values, the effective work function may be calculated from the expression

$$\phi_{effective} = (1.98 \times 10^{-4})\, T \log[120\, S_o T^2 / I(0)] \qquad (1)$$

where S_o is the emission area (in square centimeters) defined by the collector-guard ring geometry; T is the emitter temperature (in ^oK); and I(0) is the zero field saturated emission (in amperes). The constant, 1.98×10^{-4}, is appropriate for $\phi_{effective}$ in units of electron volts and for logarithms to the base 10. Table V is a summary of the effective work function values for five vapor-deposited rhenium emitters.

In addition to the effective work function, Richardson plots were constructed to obtain Richardson work functions and Richardson A values. Figure 14 is a Richardson plot for vapor-deposited rhenium emitter I. From the slope of the line the Richardson work function is measured to be 4.93 eV and the Richardson intercept, A_R, is 49 amps/cm^2 - $^oK^2$. Since the Richardson line and the effective work function value are merely alternate ways of presenting the same experimental data, there

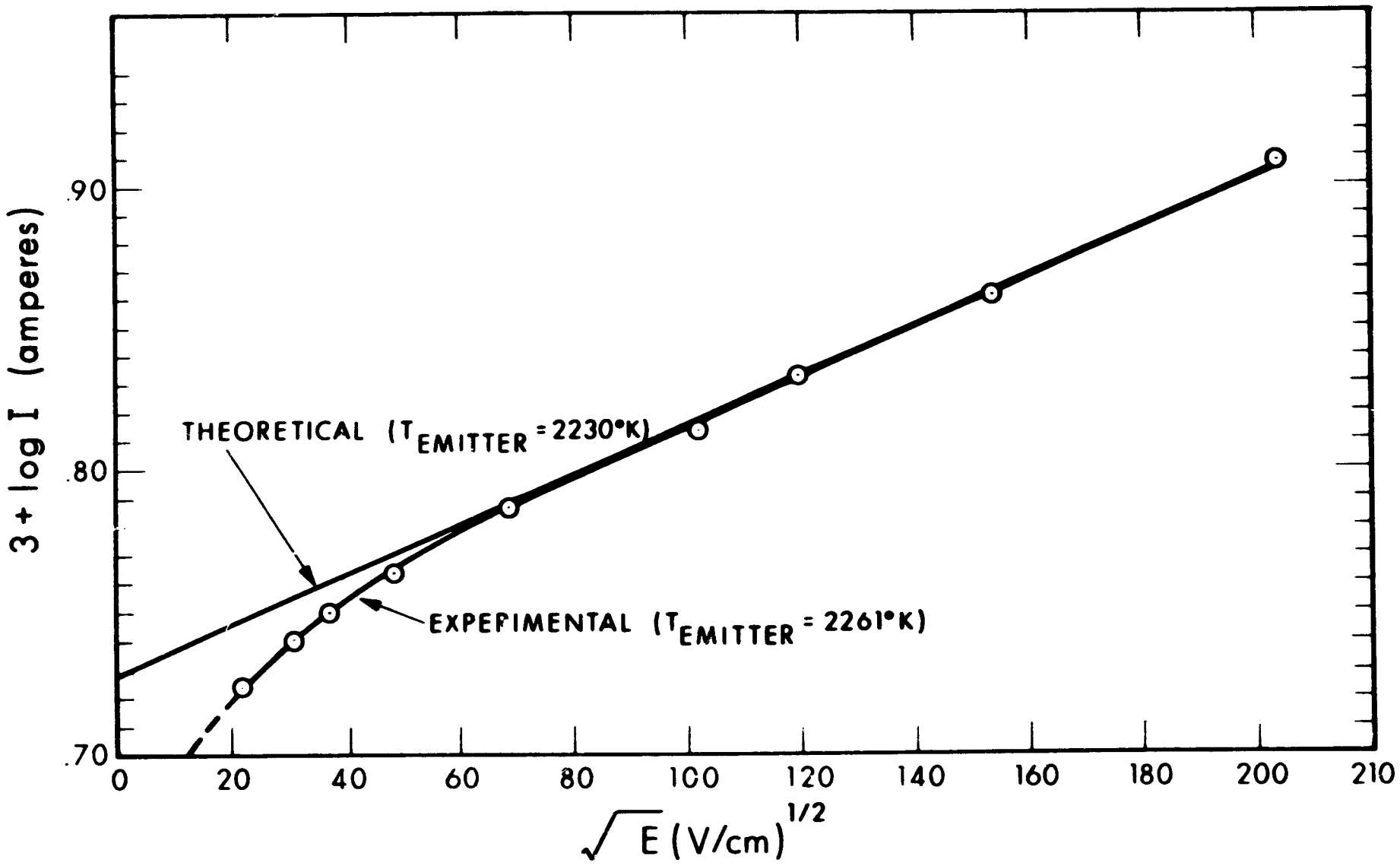

Figure 12. Schottky Plot of Emission from Vapor-Deposited Rhenium Sample I, at an Emitter Temperature of 2261°K

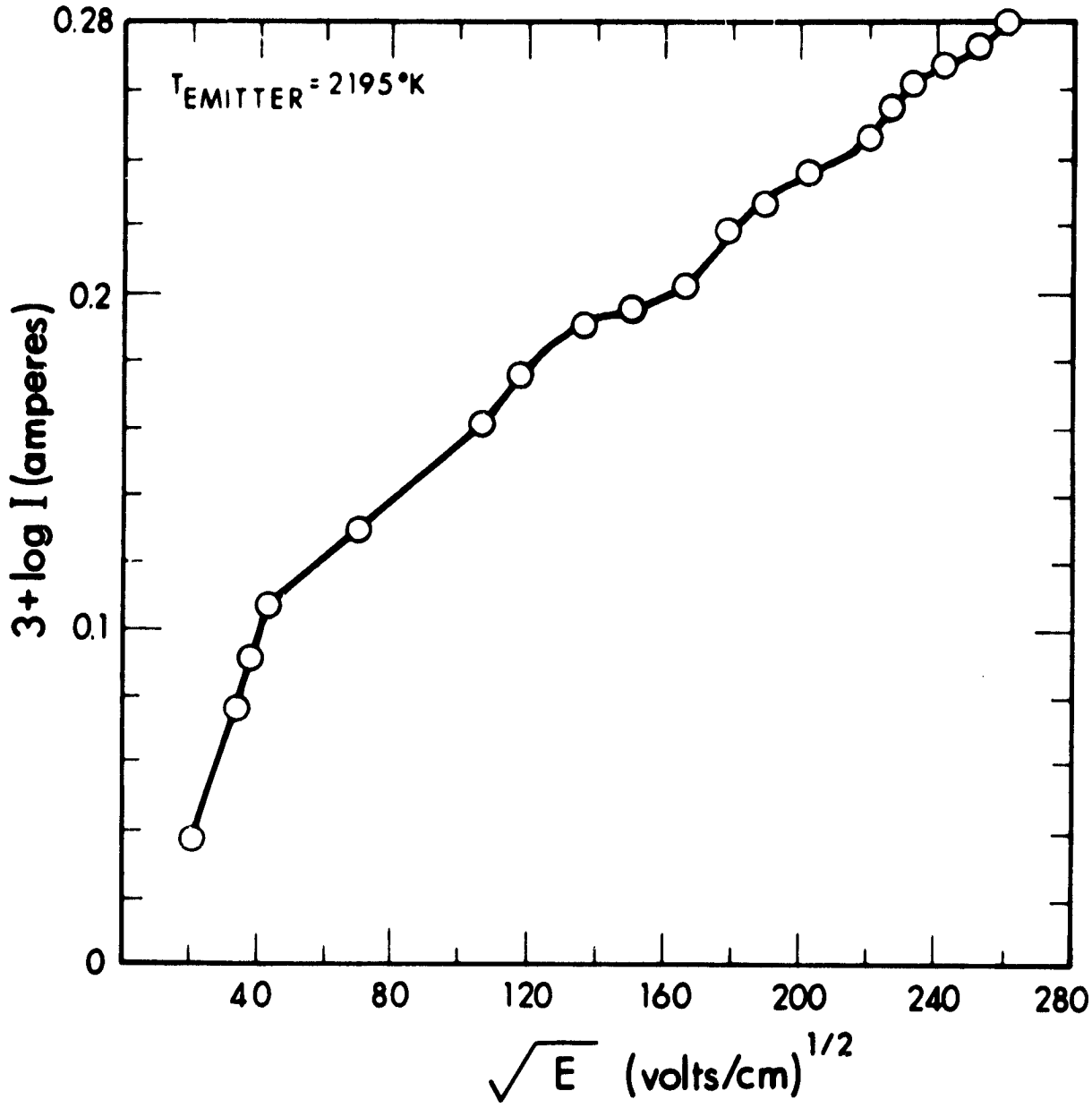

Figure 13. Periodic-Type Variations in a Schottky Plot of Electron Emission

TABLE V

SUMMARY OF EFFECTIVE WORK FUNCTION VALUES,
ϕ_{eff} ±0.04 eV, VAPOR-DEPOSITED RHENIUM EMITTERS

Emitter Temp (°K)	Emitter I	Emitter II	Emitter III	Emitter IV	Emitter V
1698	(5.05)*	5.09	—	—	—
1792	(5.06)	5.12	—	—	—
1855	(5.07)	5.12	—	—	—
1857	5.08	—	—	—	—
1876	—	—	5.07	—	—
1943	—	—	5.07	5.12	—
1947	5.06	—	—	—	5.08
2003	(5.08)	5.13	—	—	—
2008	5.08	—	—	—	—
2046	—	—	5.09	5.14	—
2051	(5.08)	5.15	—	—	5.10
2096	—	—	—	5.13	—
2105	5.08	5.16	5.10	—	5.09
2150	—	5.14	—	5.15	—
2160	—	5.10	—	—	5.11
2195	—	—	—	5.17	—
2205	—	5.11	5.13	—	—
2262	5.09	5.15	—	—	5.16
2336	5.10	5.15	—	—	—

* Refer to p. 31 for explanation of values in parentheses.

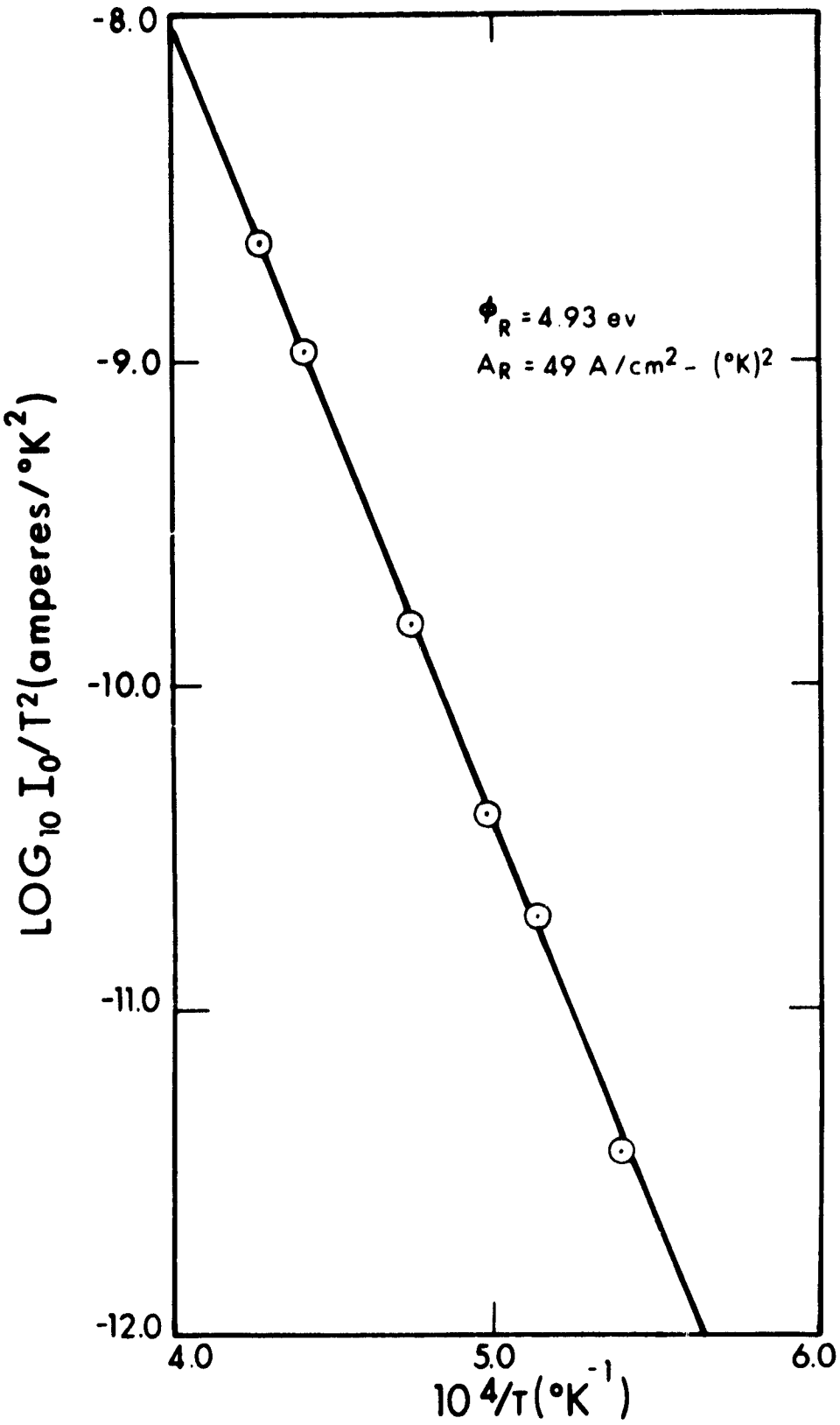

Figure 14. Richardson Plot for Vapor-Deposited Rhenium Emitter I

25752

is a relationship between the effective work function, sample temperature, Richardson work function, and Richardson intercept. These parameters are related by

$$\phi_{effective} = \phi_R + 1.98 \times 10^{-4}\ T \log(120/A_R) \qquad (2)$$

for work functions in units of electron volts, and A_R in $A/cm^2 - {}^oK^2$. Thus, using the experimentally determined Richardson work function and intercept, $\phi_{effective}$ should vary linearly with temperature according to the above equation if the data analysis is consistent.

The data points in Fig. 15 are a plot of effective work function versus emitter temperature for emitter I. The solid line in this figure is computed from Eq. 2 using the ϕ_R and A_R determined from the Richardson plot in Fig. 14. The effective work functions shown in parentheses in Table V were obtained from the line of Fig. 15.

For comparison purposes, a polycrystalline rhenium emitter was examined for effective work function. Using the previously described equipment, experimental methods and analyses, the effective work function for polycrystalline rhenium was determined and is listed in Table VI. The values agree quite well with those reported elsewhere in the literature (Refs. 8 and 9). Table VI also includes the average of the effective work function values from Table V to provide a ready comparison between vapor-deposited and polycrystalline rhenium.

TABLE VI

COMPARISON OF EFFECTIVE WORK FUNCTION VALUES, ϕ_{eff} ±0.04 eV, FOR POLYCRYSTALLINE AND VAPOR-DEPOSITED RHENIUM

$T_E({}^oK)$	ϕ_{eff} (polycrystalline rhenium)	ϕ_{eff} (vapor-deposited rhenium)
1850	4.81	5.08
1952	4.70	5.10
2052	4.80	5.11
2152	5.01	5.12
2207	5.03	5.14

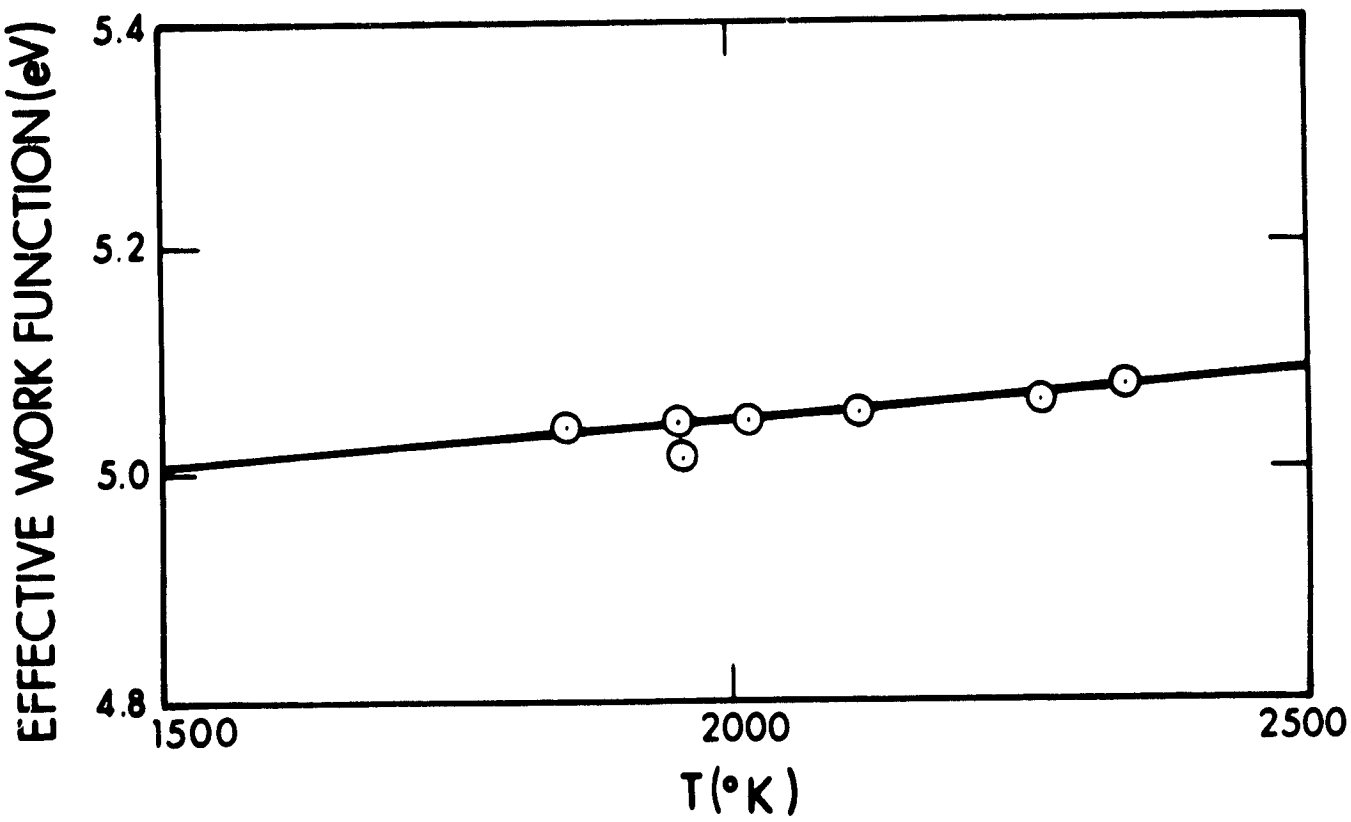

Figure 15. Effective Work Function versus Emitter Temperature for Vapor-Deposited Rhenium Emitter I

2.2.3 ELECTRODE PREPARATION

The effective work function for vapor-deposited rhenium has been determined experimentally by vacuum emission measurements after various surface preparations to determine if such preparations might enhance the bare work function. Three different surface preparations were examined and are reiterated here for sake of clarity: (1) diamond-dust lapped to achieve a final surface smoothness of less than 10 microinches as indicated by a profilometer; (2) finally polished with Linde A, B, and C alumina powders to a mirror finish; and (3) heavily electro-etched in a solution of 350 ml perchloric acid, 175 ml methanol, and 50 ml butoxyethanol. After all surface preparations, the samples were chemically cleaned, in hydrochloric acid and in Oakite, and then boiled in distilled water. Figure 16 shows representative curves of vacuum emission measurements before and after electro-etching of vapor-deposited rhenium sample II. This reveals that the bare work function value did not change significantly. Tables VII and VIII compare the results of vacuum emission measurements of effective work function for vapor-deposited rhenium samples II and V, respectively.

In nearly every case, at a given temperature, the difference in effective work function for different surface preparations is within experimental error. Tables VII and VIII also show that the difference in effective work function, at different temperatures, for any given surface preparation, is within experimental error. In conclusion, elaborate surface preparations such as fine polishing, electro-etching, or high temperature processing (at 2700^{o}K for 2 hours) appear to have no measurable effect on the bare work function of vapor-deposited rhenium.

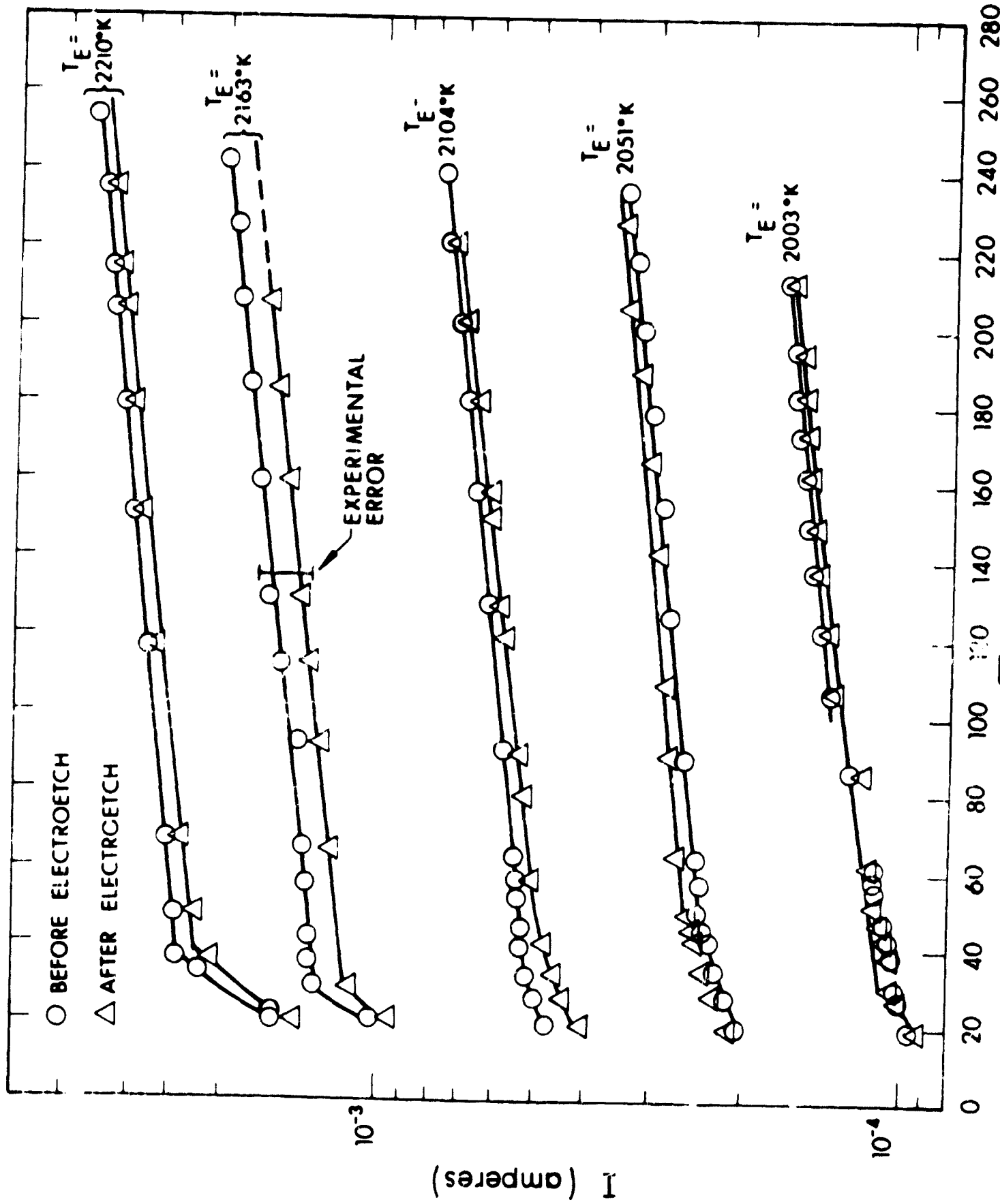

Figure 16. Vacuum Emission Measurements Before and After Electroetching Vapor-Deposited Rhenium (Sample II), with Emitter Temperatures as the parameter

TABLE VII

EFFECTIVE WORK FUNCTION VALUES, ϕ_{eff} ±0.04 eV,
FOR VAPOR-DEPOSITED RHENIUM SAMPLE II

	Effective Work Function (eV)		
$T_{emitter}$ (^{o}K)	Diamond Lap	Fine-Polish	Electro-Etch
2206	5.11	5.19	5.04
2148	5.09	5.18	5.04
2093	5.12	5.18	5.03
2043	5.09	5.17	5.04
1993	5.11	5.17	5.05

TABLE VIII

EFFECTIVE WORK FUNCTION VALUES, ϕ_{eff} ±0.04 eV,
FOR VAPOR-DEPOSITED RHENIUM SAMPLE V

	Effective Work Function (eV)	
$T_{emitter}$ (^{o}K)	Diamond Lap	Fine-Polish
2157	5.12	5.12
2106	5.16	5.09
2055	5.15	5.10
1952	5.13	5.08

2.3 THERMIONIC ELECTRON EMISSION MICROSCOPE

Electrons, thermionically emitted from a metal at high temperature, can be used to provide a magnified image of the surface by accelerating them through an electrostatic lens system and focusing them on a phosphor screen. An imaging device designed for this purpose is called a thermionic electron emission microscope.

A thermionic emission microscope is normally operated so that the light intensity emitted by a region of the image on the phosphor screen is proportional to the electron current emitted by the corresponding region of the emitter surface. Thus the pattern displayed by the image and the contrast in the pattern are the result of selective electron emission from the emitter. Since the electron emission from a region of the emitter surface is determined by the local electron work function, the pattern displayed by the image is basically the work function pattern of the emitter surface.

The work function pattern is due to the distribution of exposed crystal faces developed within the surface grains. Each face of a crystal has a characteristic work function, and those exposed on the emitter surface appear on the phosphor screen with an intensity inversely related to their work function values, i.e., high work function faces appear as low intensity or dark regions and low work function faces as high intensity or light regions.

The following paragraphs in this section describe the EOS thermionic electron emission microscope design, the design modifications necessary for examining vapor-deposited rhenium, and microscope data concerning observations and measurements of vapor-deposited and polycrystalline rhenium.

In summary, the microscope proved invaluable as a third approach (complementing the metallurgical and vacuum emission studies), and perhaps the most useful of all instruments employed for surface investigations of thermionic electrodes.

2.3.1 MICROSCOPE DESIGN MODIFICATIONS

It was anticipated that many of the vapor-deposited rhenium grains could have dimensions as small as 0.002 inch or less. This was known to be true, at least, for vapor-deposited tungsten. Based on these considerations, a microscope magnification of 1000X was selected to present a readily discernible image on a 3-inch-diameter screen. In conjunction with this, it was felt desirable to have a resolution of 0.1μ to 0.2μ so that microstructure within an individual grain could be examined. Having established these criteria, the EOS thermionic electron emission microscope required the following modifications:

a. A two-lens system to achieve a minimum of 1000X magnification.

b. A 30 kV accelerating potential to achieve 0.1μ resolution.

c. A high temperature grid and grid support system to permit emitter samples to operate at temperatures of 1900°C to 2000°C. These temperatures were projected as necessary for sufficient screen illumination from such a high work function surface.

d. A Faraday cage to provide an <u>in situ</u> measure of electron emission from individual grains and assorted microstructures.

The five basic components of the microscope are the emitter mount and heater; emitter positioning mechanism; lenses; screen; and vacuum system. The design and operation of these components, especially the lens section, determine the quality of the image and the versatility of the instrument. Figure 17 is an assembly drawing of the modified microscope indicating the location of these components.

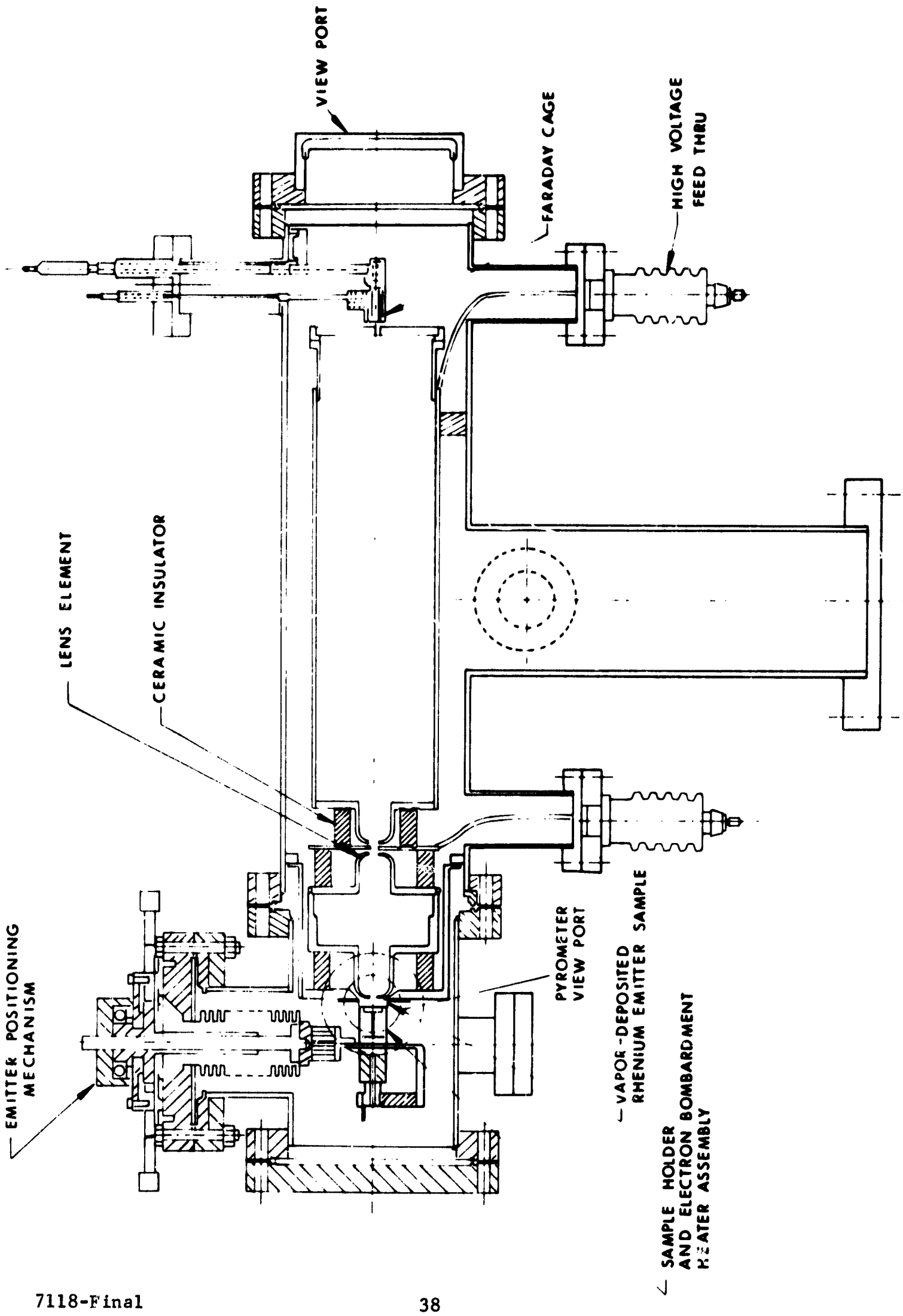

Figure 17. Thermionic Emission Microscope, Assembly Detail

The emitter and electron bombardment heater assembly is an integral unit retained from the vacuum emission vehicle studies, as discussed in Subsection 2.2.1. It is therefore possible to transfer an emitter from the emission vehicle to the emission microscope without any intermediate steps of welding, brazing, or processing. In this manner, the emitter surface remains free from distortion or contamination. It is also important to recall that the heater unit remains exactly in place with respect to the emitter, hence providing a means of heating the emitter in exactly the same manner each time.

Emitter temperatures were determined by measuring the temperature of a hohlraum drilled into the side of the sample with a depth-to-diameter ratio of 10 to 1. The hohlraum was observed through a view port located on the side of the vacuum chamber of the microscope. All temperature measurements were conducted with the same calibrated micro-optical pyrometer used to measure emitter temperatures in the emission vehicle. Corrections for view port losses were slightly less than the bell jar losses listed in Table IV.

The sample mount and heater assembly are mounted in the microscope chamber on a three-axis traverse mechanism which is controlled by a 0.0001 inch micrometer outside the chamber. Excursions of approximately 1/2 inch along the microscope axis and 3/8 inch in both directions perpendicular to the axis are possible, thus permitting a precision scan of an emitter surface.

The two electrostatic lenses, the immersion objective lens and the projection lens, are three-element lenses adapted from a design by Johannson and discussed in detail in his paper (Ref. 10). Figure 18 depicts the axial potential distribution of the modified lens system. Each lens yields an approximate magnification of 33X; therefore, the two lenses can achieve 1000X magnification. Since the image quality is extremely sensitive to the lens alignment and ellipticity of the

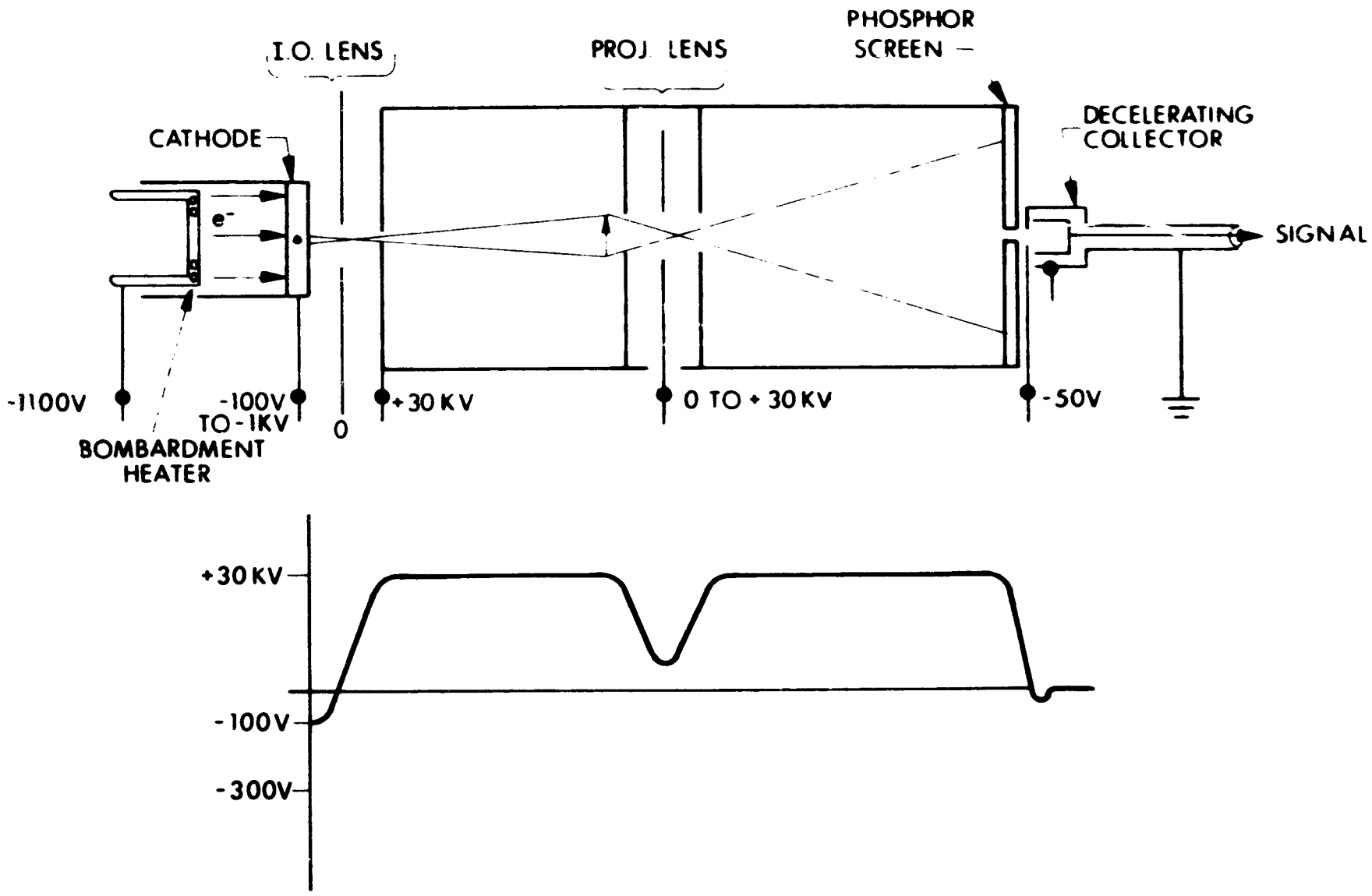

Figure 18. Schematic of Thermionic Electron Emission Microscope Showing Axial Potential Distribution

individual lens apertures, the lens elements were assembled and aligned axially to within 0.0005 inch. The individual aperture ellipticity exceeded the design specification of 0.0004-inch roundness. The final alignment and inspections were conducted after the lenses were vacuum heat treated at temperatures 200 to 300°C higher than their intended operation temperatures in the microscope.

Because of the high emitter temperatures and the close spacing between the immersion objective lens and emitter, the objective lens element intercepts a considerable amount of radiant heat (approximately 80 watts). To avoid excessive temperature of the lens and to reduce the possibility of warpage and misalignment, it is made from arc-case molybdenum and mounted firmly on an arc-cast molybdenum plate (see Fig. 19), which is in turn mounted firmly onto the vacuum chamber walls. Because of this arrangement, the immersion objective lens is necessarily operated at ground potential. The remaining lenses are specially-shaped stainless steel elements which are electrically insulated from the chamber. The last element of the projection lens is in contact with a cylindrical tube which supports a phosphor screen. This tube provides a field-free drift space and subsequent target area for electrons emerging from the lens system (see Fig. 18).

The phosphor screen simply converts the electron image to a visual image which is viewed through a 4-1/2 inch Pyrex port at one end of the microscope chamber. The screen is a 3-1/4 inch diameter nonbrowning glass aluminized for 30 kV operation and is coated with P31 phosphor. The screen center contains a 1/8 inch hole which in turn is used to locate a precision metal insert of 0.040 ±0.0004 inch diameter which serves as the aperture for electron emission measurements. Figure 20 is a sketch of the apparatus used to measure the electron flux through the screen aperture. It is commonly referred to as a Faraday cup or Faraday cage and is designed to permit electron emission measurements within the

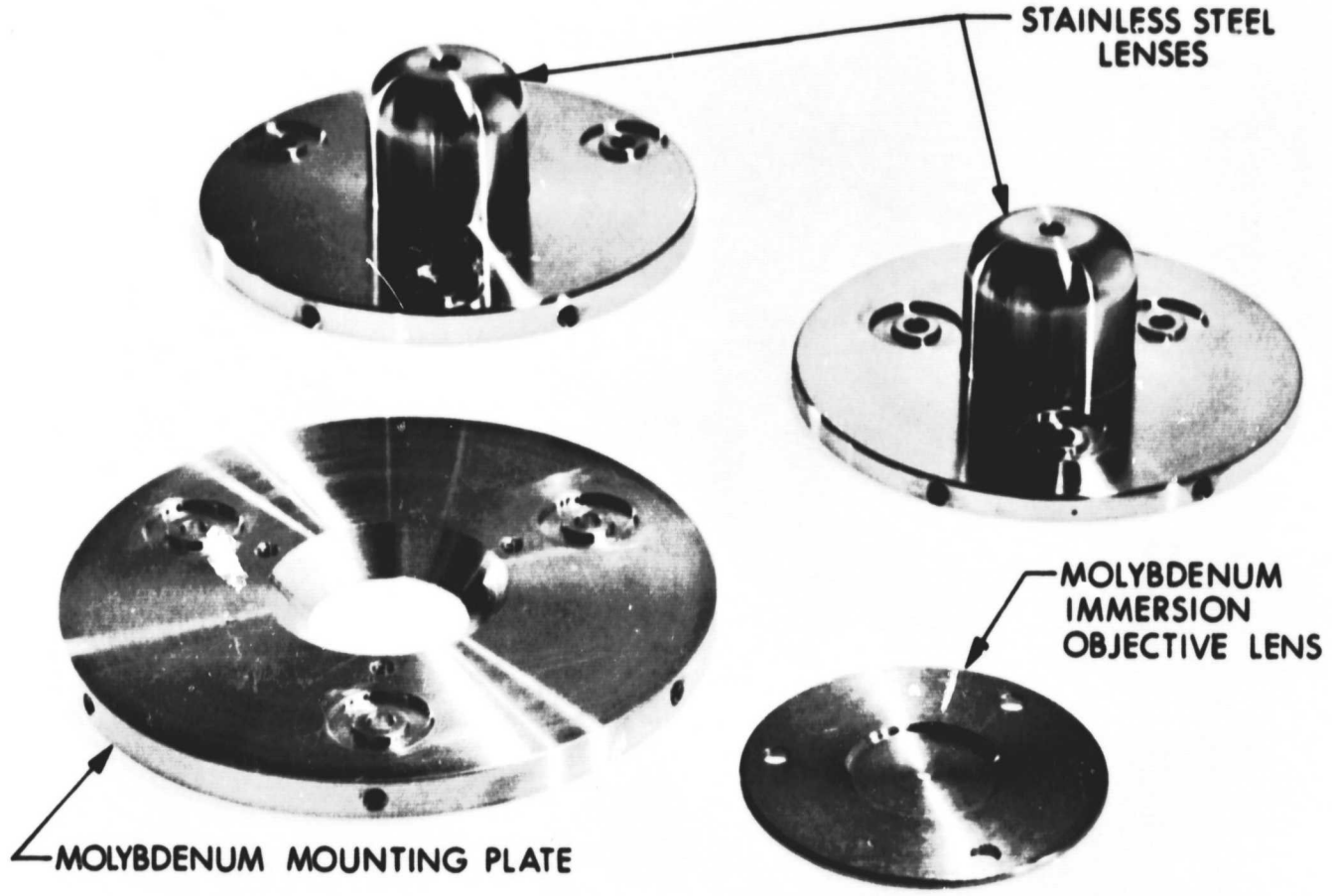

Figure 19. Lenses and Mounting Plate for Thermionic Electron Emission Microscope

126682

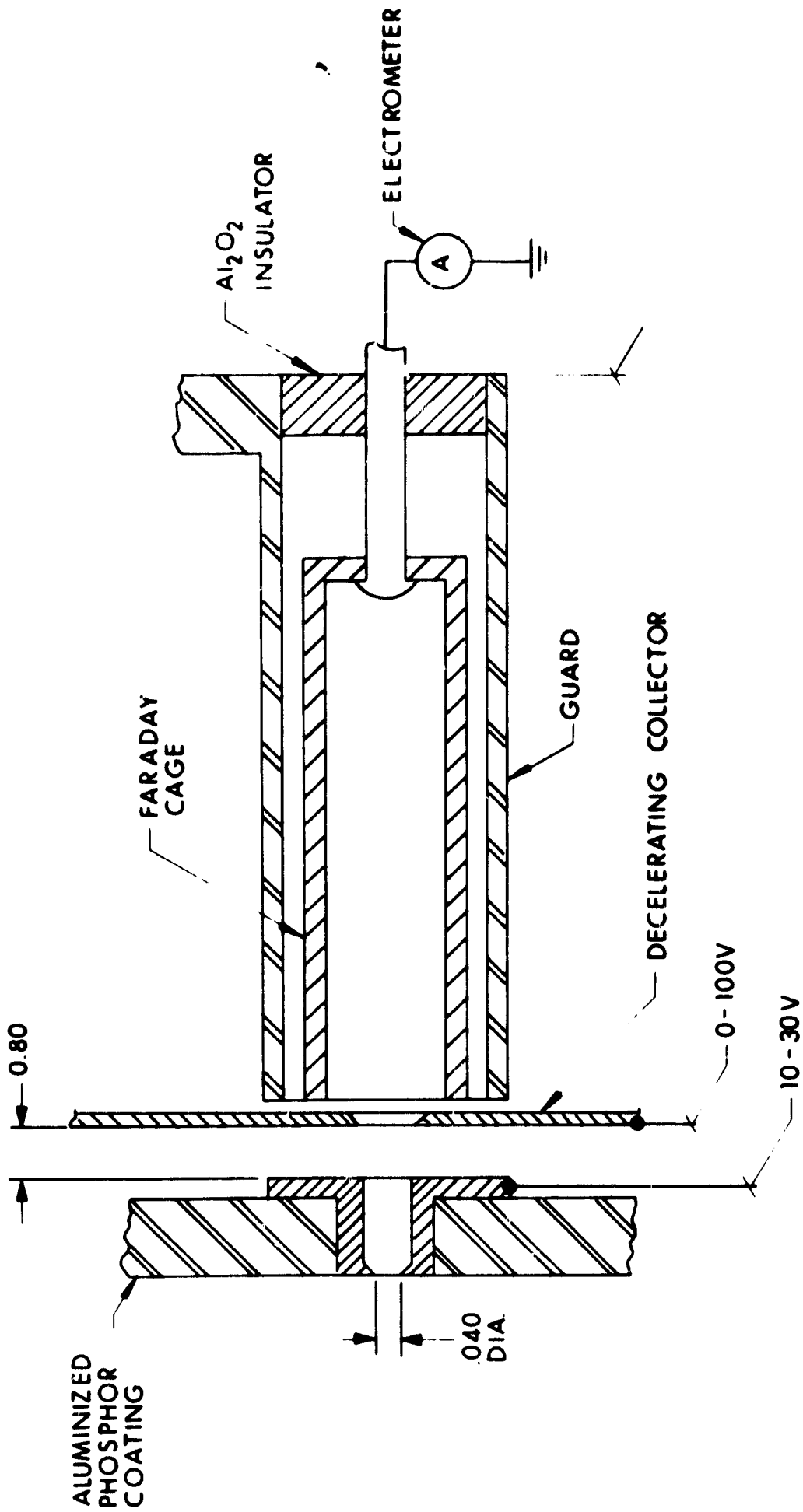

Figure 20. Faraday Cage Detail

individual grains of vapor-deposited and polycrystalline rhenium. This Faraday cage is installed with its axis common to the preceding lens system axis. The cage is located behind a decelerating collector which prohibits the formation of secondary electrons (Ref. 11).

The cup current lead is guarded in such a manner as to compensate for the current meter voltage drop. A dc battery equalizes the potential across the holding ceramic, thus ensuring that no potential differences cause small current shunts external to the measuring circuit. At current levels of 10^{-11} ampere and below, the problems of ac pickup and other electrical disturbances are minimized by electrostatically screening the meters and metering leads. The noise level measured from 1 to 5 $\times 10^{-14}$ ampere at operating conditions.

The entire microscope chamber is designed to be capable of ultrahigh vacuum operation. All components are fabricated from materials capable of high temperature vacuum processing. Copper gasket seals are used on all flanges and the seals of the view ports are fused-metal-to-glass seals. The entire unit may be processed at 400°C, although this temperature was not required in practice. It was found that a 250°C bakeout for six to eight hours was sufficient to obtain a pressure of 1×10^{-9} torr with a 140 liter/sec vac-ion pump. Since the presence of a 2 or 3 gauss magnetic field could disturb the electron beam trajectory in the low voltage section of the microscope, nonmagnetic stainless steels are used in its construction. Moreover, the vac-ion pump magnets are shielded with mu-metal. A gauss meter measurement in the microscope interior indicated a 0.15 to 0.25 gauss field (which is essentially the earth's magnetic field at Los Angeles). Figure 21 is a photograph of the microscope exterior identifying the various voltage feedthroughs and vacuum plumbing.

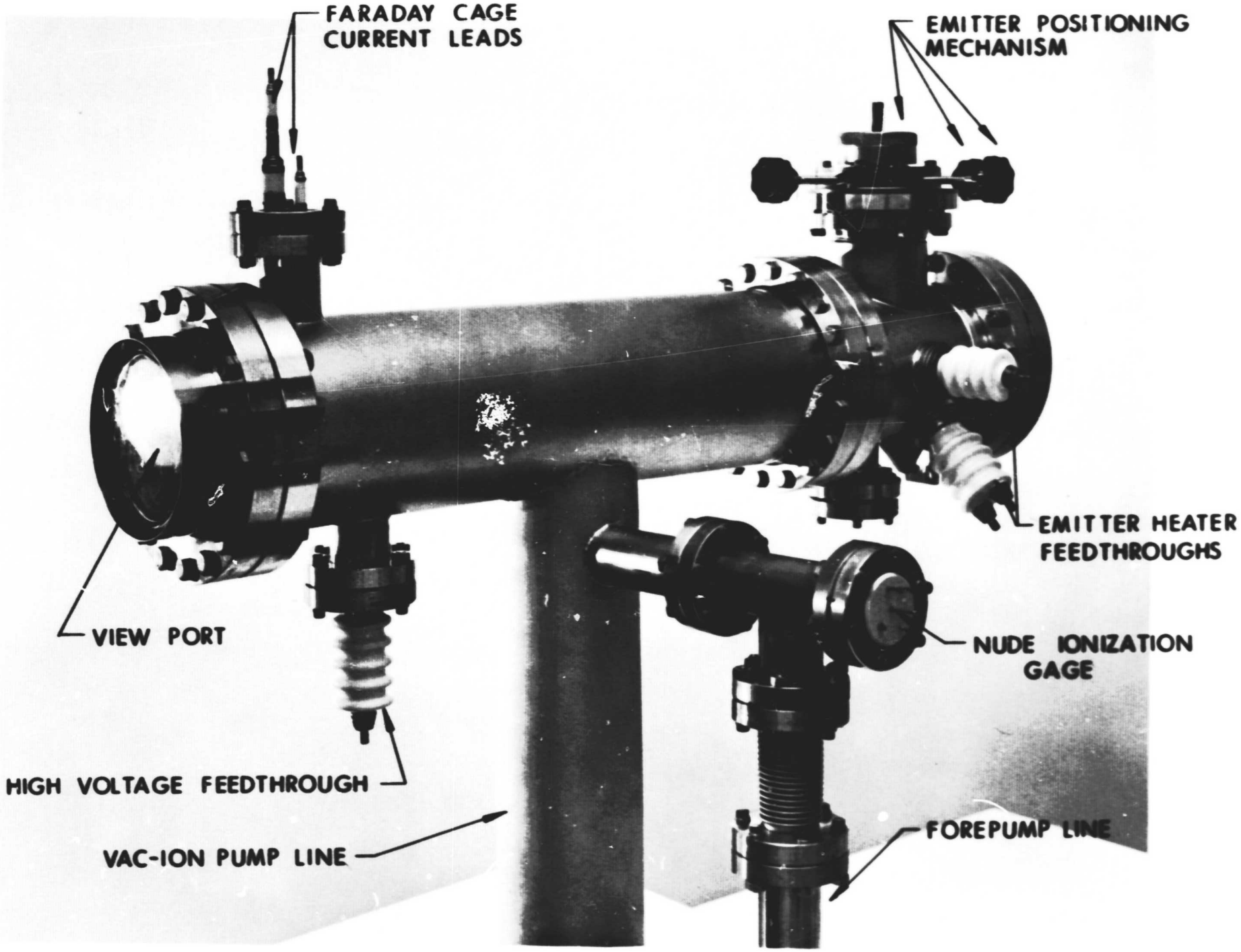

Figure 21. Thermionic Electron Emission Microscope, Exterior View

All of the observations and emission measurements discussed in this section were made with the microscope evacuated to 1×10^{-8} torr and lower.

The thermionic electron emission microscope, in operation, satisfied or exceeded all the design goals. The operational parameters are enumerated below.

Magnification	Variable from 600X to 1400X
Resolution	Approximately 0.15 micron
High temperature emitter operation	1900 to 2300^{o}K (as measured by a micro-optical pyrometer sighted in a blackbody hohlraum)
Faraday cage	5×10^{-13} ampere and above
Drive mechanism	Scans (X-Y plane) central 3 cm^2 of emitter sample. 1/4 inch excursion (Z-axis) along optical axis

Figure 22 depicts the microscope in operation with an image of (~ 425X) of a vapor-deposited rhenium emitter on the phosphor screen as seen through the viewing port.

2.3.2 EMISSION MICROGRAPH OBSERVATIONS

Optical micrographs have been taken of electrode surfaces of vapor-deposited and polycrystalline rhenium in the thermionic emission microscope in conjunction with certain metallographic preparations of the surfaces, including rough diamond lapping, fine polishing, electro-etching, and high temperature treatment in vacuum. The presence of surface irregularities on vapor-deposited and polycrystalline rhenium has been observed in the thermionic emission microscope as well as metallographically.

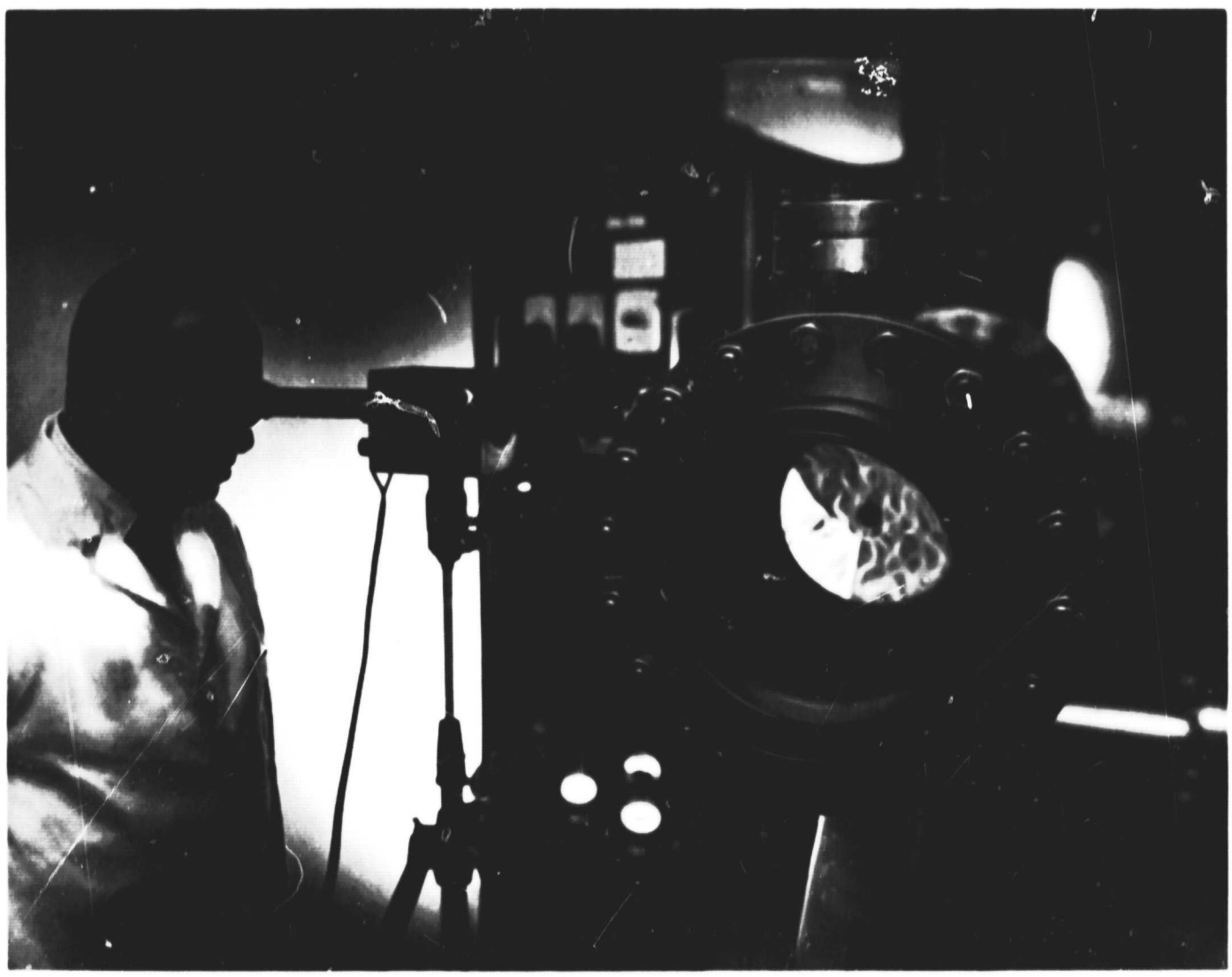

Figure 22. Thermionic Electron Emission Microscope in Operation

PM 567118

Vapor-deposited rhenium sample II was selected for study in the thermionic emission microscope. It represents an average sample of vapor-deposited rhenium (with respect to thermal treatment, grain size, and work function). A randomly selected area of sample II was photographed, and a composite picture of this area is shown in Fig. 23. The bright grain located in the upper center of the picture is indicative of a low work function grain surrounded by higher work function grains (gray and black areas). The dark center of each photograph is the hole insert of the Faraday cage which was later mounted for emission measurements. The surface seen in Fig. 23 received a rough diamond lapping and the emission micrographs making up the composite were taken after about 25 hours at 1885°C operation. The surface irregularities, or striations, are vividly evident in this photograph. The area outlined in Fig. 23 corresponds to the optical micrographs of the same area in Fig. 4. A comparison of these indicates the enhanced clarity of surface irregularities possible with the emission micrographs.

Subsequently, the sample was diamond scribed with a set of orthogonal axes which were used for identification and location of grains on the sample surface. Figures 24a, 24c, and 24e are emission micrographs showing the scribe marks as they originally appeared on the emitting sample surface. It can be seen that the scribing operation work-hardened or stressed the surface, which was subsequently recrystallized when the emitter was brought to operating temperature. In some areas this abrasion also exposed a more ordered surface, as evidenced in Fig. 24c where the surface irregularities have been "removed" from the dark grains.

Figures 24b, 24d, and 24f are emission micrographs showing scribe lines after about 60 hours operation at 1800°C to 1900°C. These photographs show that the lines have been totally stress relieved and that secondary or preferential recrystallization has taken place. This is consistent with emission microscope observations made on other materials such as

Figure 23. Vapor-Deposited Rhenium Sample II; Composite of Emission Micrographs (425X)

BEFORE ↓

AFTER ↓

a.

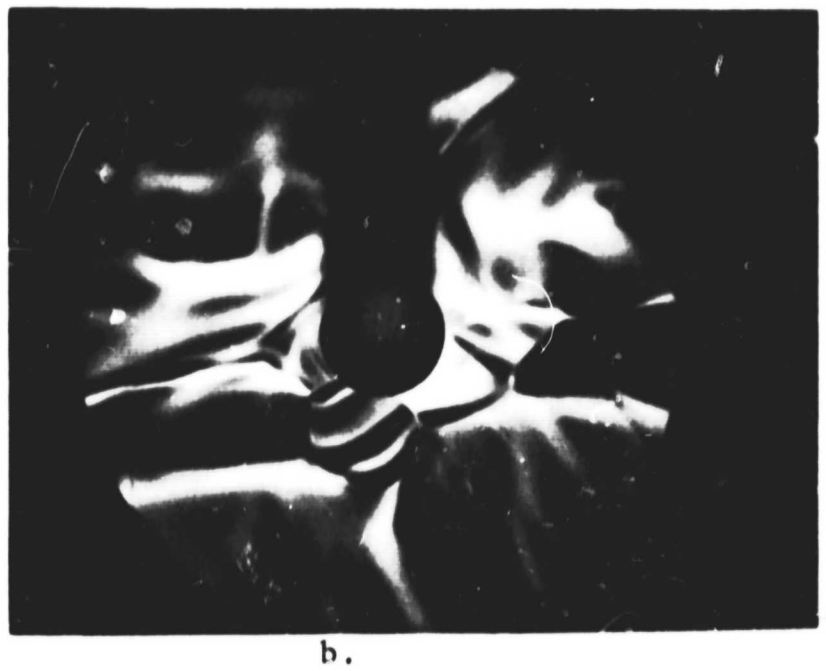

b.

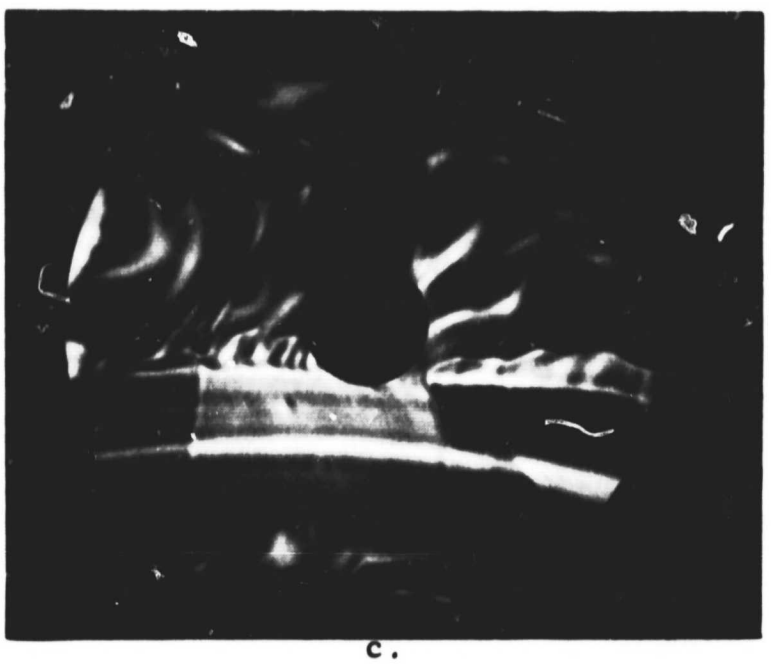

c.

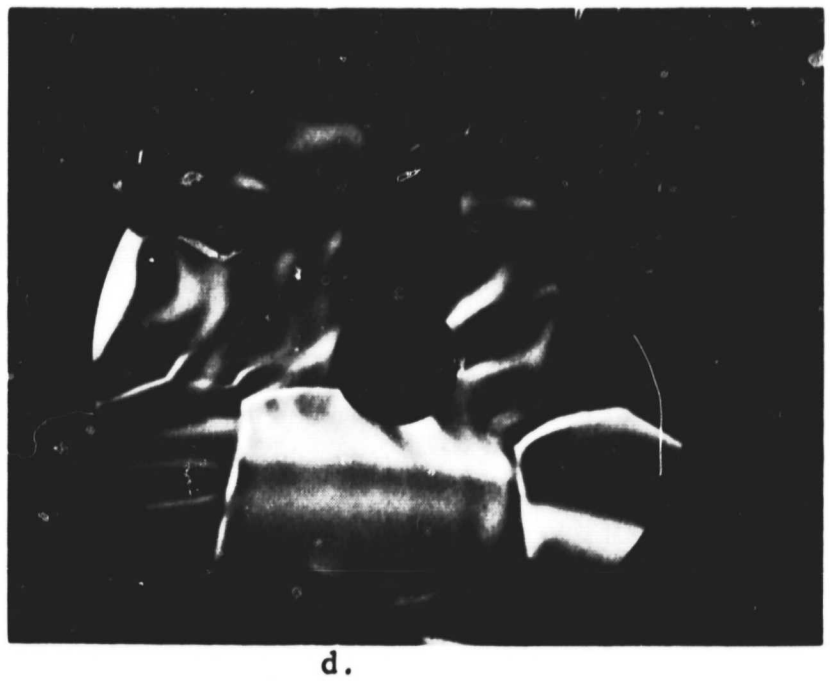

d.

e.

f.

319

7118-Final

Figure 24. Recrystallization History of Selected Areas Along a Scribed Surface Before (a, c and e) and After (b, d and f) Secondary (Preferential) Recrystallization of Vapor-Deposited Rhenium (662X)

molybdenum (Ref. 12). The central portion of the photograph is obscured by the Faraday cage which was placed in front of the screen aperture for emission measurements.

Figures 25 and 26 compare optical micrographs to the corresponding electron emission micrographs of the same locations on the sample surface. The optical micrographs contain a wider field of view and lack the field distortions at the picture edges which are apparent in the emission micrographs. On the basis of comparing several such corresponding sets of photographs, it was concluded that grains with similar microstructure and surface detail yield the same electron emission. It is worth noting that the surface structure observed in Fig. 25 was also identified in the other samples.

Figure 27 shows surface irregularities typical of the sample. These irregularities are similar in appearance to chemical or dislocation "etch" pits observed on the surfaces of other materials. However, they lack the number density usually associated with such etch pits (Ref. 13).

Vapor deposited sample II was electro-etched by methods described in Subsection 2.1.3. Figure 28 shows a composite of the microstructure after etching; this is the same area as the composite of Fig. 23. The outlined area is the same as that shown in the photomicrograph, Fig. 5. The surface irregularities are still present but appear less clearly in Fig. 28 than in Fig. 23 because of deep etching and rounding at the grain boundaries. The light areas appear to have been etched more severely than the dark areas although a precise visual evaluation is not possible.

Vapor-deposited sample II was then removed from the emission microscope and polished to a mirror finish with Linde alumina powders A, B, and C. Figures 29a, 30a and 31a are three randomly selected areas taken at 1800^{o}C. Figures 29b, 30b, and 31b show the same areas as Figs. 29a, 30a, and 31a after 75 hours at 1800^{o}C. Thermal etching at the grain

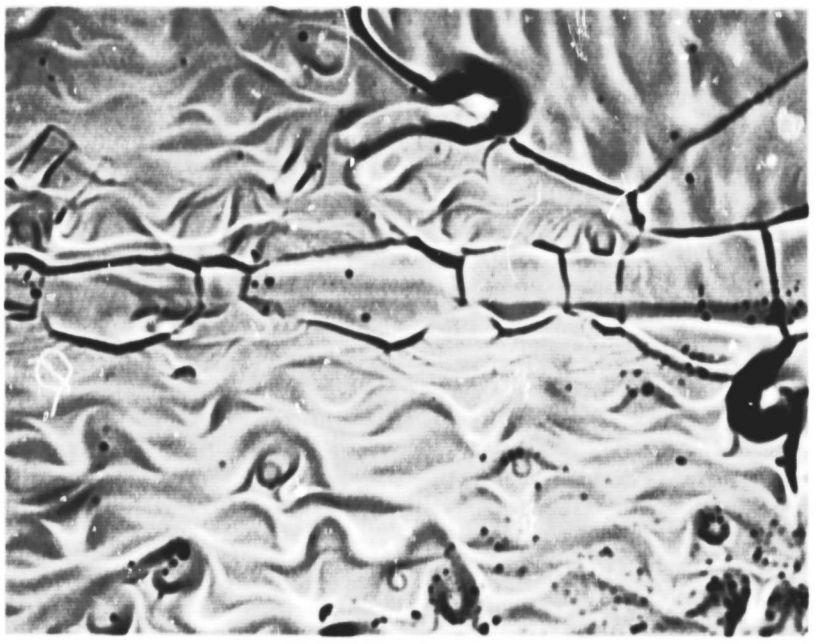

a. Optical Micrograph (625X)

b. Emission Micrograph (662X)

Figure 25. Micrographs of Vapor-Deposited Rhenium, Sample II, at 1700°C after Approximately 60 Hours of Operation at Approximately 1850°C

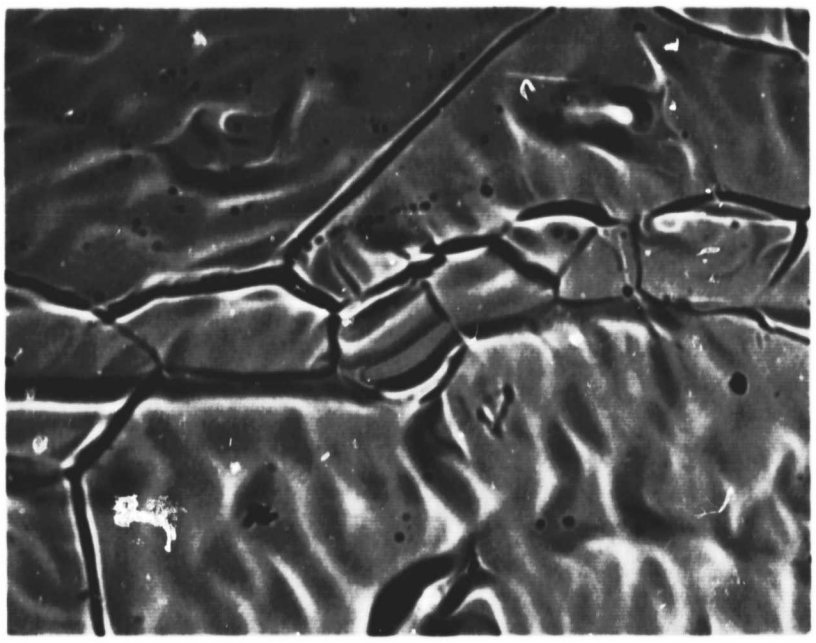

a. Optical Micrograph (688X)

b. Emission Micrograph (662X)

Figure 26. Micrographs of Vapor-Deposited Rhenium Sample II, at 1700°C after Approximately 60 Hours of Operation at Approximately 1850°C

Figure 27. Emission Micrograph of a Typical "Etch" Pit at 2000°K (997Å)

Figure 28. Emission Micrograph Composite After Electro-Etch of Area in Figure 23 (425X)

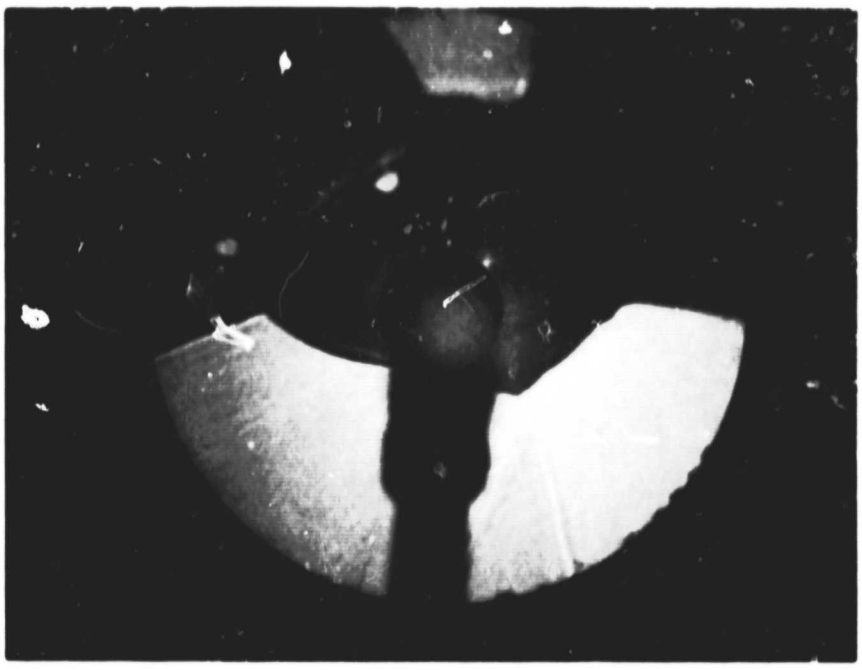

a. Initially Polished (662X)

b. After 75 Hours at 1800°C (662X)

Figure 29. Vapor-Deposited Rhenium Sample II Showing the Effect of Fine Polishing on Surface Irregularities and Grain Growth

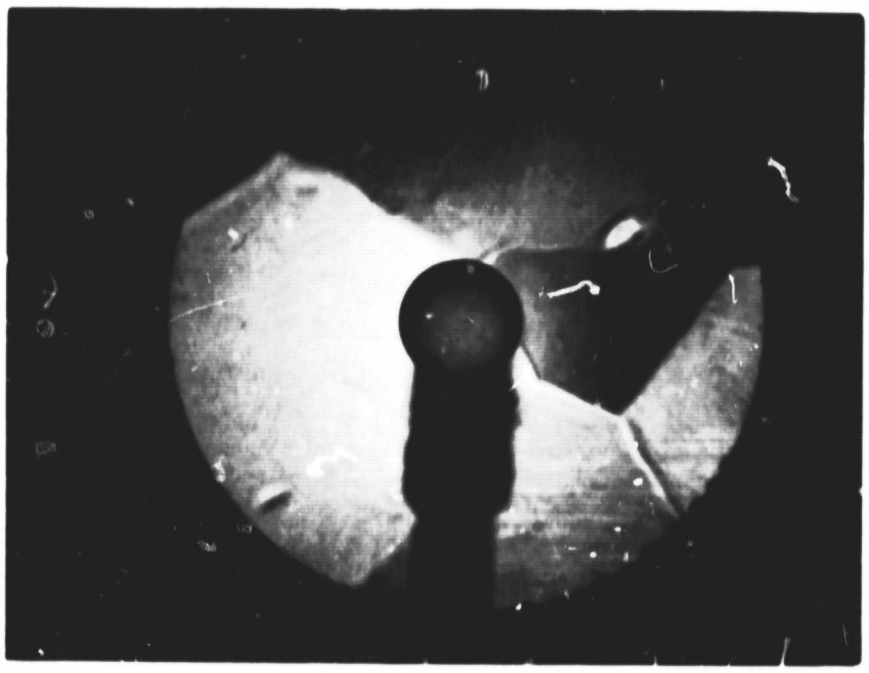

a. Initially Polished (662X)

b. After 75 Hours at 1800°C (662X)

Figure 30. Vapor-Deposited Rhenium Sample II Showing the Effect of Fine Polishing on Surface Irregularities and Grain Growth

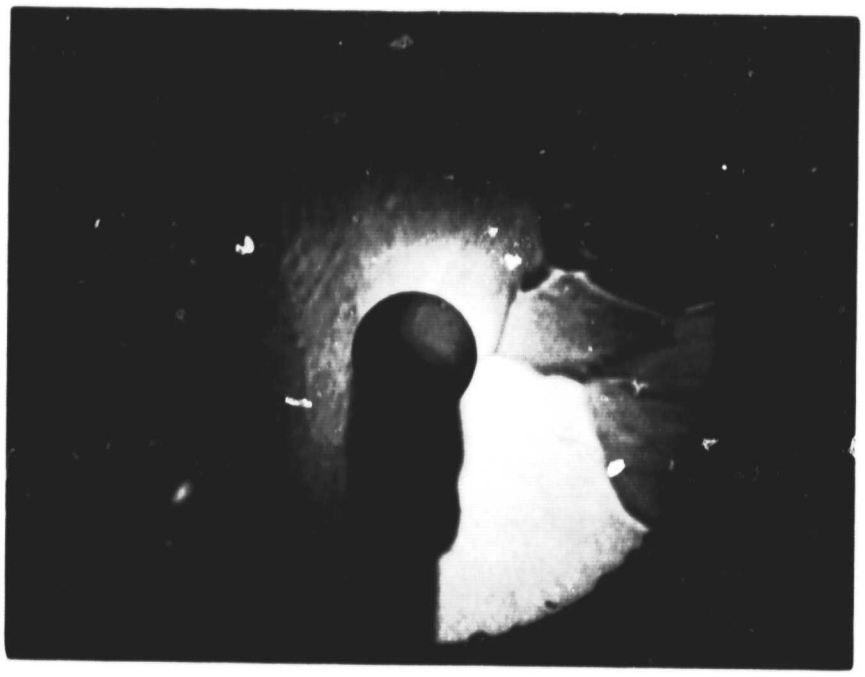

a. Initially Polished (662X)

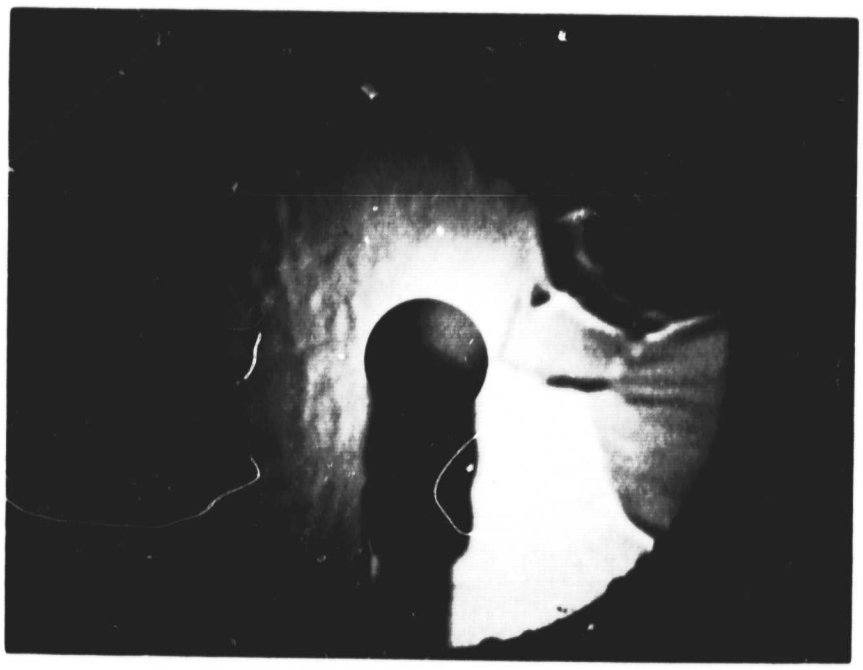

b. After 75 Hours at 1800°C (662X)

Figure 31. Vapor-Deposited Rhenium Sample II Showing the Effect of Fine Polishing on Surface Irregularities and Grain Growth

boundaries and some thermal etching of the surface are visible. The dark grain in the center of Fig. 29a is seen to have diminished in size at the expense of the larger surrounding grains in Fig. 29b. The small dark grain in Fig. 30a completely disappeared as the surrounding grains have grown. It is interesting to note the complete lack of surface irregularities in Figs. 29a and 30a as compared with Figs. 23 and 28. Even after 75 hours at 1800°C, Figs. 29b and 30b indicate only slight thermal etching of the surface. This observation tends to lend credence to the conclusions reached by metallographic analyses (Subsection 2.1.3) after various surface preparations, that since fine polishing removes the surface irregularities, which do not return after high temperature annealing, the irregularities are most likely the result of an initially rough surface preparation. These irregularities cannot be removed by electro-etching or by high temperature heat treatment. Figures 29b, 30b, and 31b do not appear as sharp after time at temperature as the initial micrographs. This is evidently due to thermal faceting of the grains and rounding at the grain boundaries.

2.3.3 EMISSION MICROSCOPE MEASUREMENTS

The incorporation of a Faraday cup into the emission microscope made possible the measurement of the effective work function of individual grains in sample cathodes. Measurement of the emission from a large number of grains by a scanning technique with a subsequent determination of the average effective work function has provided a basis for comparison with the average effective work function determinations obtained from the vacuum emission vehicle. Effective work function determinations have been made of highly polished, electro-etched, and rough diamond lapped vapor-deposited rhenium and of highly polished polycrystalline rhenium.

Quantitative measurements of the emission from individual grains were obtained by direct measurement of the electron current intercepted by the Faraday cup located behind the screen aperture. The sample electron current density and the Faraday cage current can be related by the first order equation

$$J_o = \frac{I \cdot M^2}{A_c} \qquad (3)$$

where I is the current from the sample as measured in the Faraday cup, J_o is the real emitter current density, M is the magnification of the microscope, and A_c is the area of the collecting hole in the center of the screen.

Vapor-deposited rhenium sample II with a diamond lapped surface finish was chosen for emission measurement and work function determinations of individual grains. A grid of 250 points was randomly selected from an area of 0.7 cm^2 and examined for emission density. Three instruments were used interchangeably for measuring the current: A Keithly 610R, a Boonton 95A, and a Cary 31. Measurements from the three instruments agreed within ±1 percent. The Cary 31 is guaranteed to be within 1 percent accurate.

The average effective work function was computed by the direct substitution of the temperature and the emission current density into the Richardson-Dushman equation with the A constant taken to be 120 $A/cm^2 - {}^oK^2$. An average current value was obtained from 250 individual current measurements at an average emitter temperature of 2158°K. The average work function computed in this manner was 5.28 ±0.04 eV which compares to a value of 5.13 ±0.04 eV as obtained from the vacuum emission vehicle. The apparent disparity between these values can be attributed to the fact that the surface of the vapor-deposited sample is so

irregular that the emission microscope sampling was insufficient to obtain a more nearly true average value for the work function.

The effective work functions of the indicated areas on a previously mapped composite (Fig. 23) of a sample area are shown in Fig. 32. There is a wide variation of ϕ_{eff} (4.97 to 5.52 eV) exhibited by the individual grains, but the lowest of 4.97 eV is approximately 80 to 100 mV higher than polycrystalline rhenium while the highest work function approaches that of single crystal rhenium of the (0001) orientation.

The increase of ϕ_{eff} of a selected low work function grain with temperature as a parameter is shown in Table IX.

TABLE IX

EFFECTIVE WORK FUNCTION OF A SELECTED GRAIN AS A FUNCTION OF TEMPERATURE TAKEN AT CONSTANT MAGNIFICATION

Temperature, ^{o}K	J_{sat}, A/cm^2	ϕ_{eff}, eV
2298	4.7×10^{-3}	5.07
2190	1.1×10^{-3}	5.07
2083	2.94×10^{-4}	5.06
1979	6.06×10^{-5}	5.06
1898	1.56×10^{-5}	5.05

Table IX shows that a temperature difference of $400^{o}K$ corresponds to a work function difference of 0.02 eV. This corresponds favorably with vacuum emission vehicle measurements as indicated in Fig. 15. This small change in effective work function shows the temperature dependence of the work function, thus providing a clear example that the measured current density is that resulting from thermionic emission.

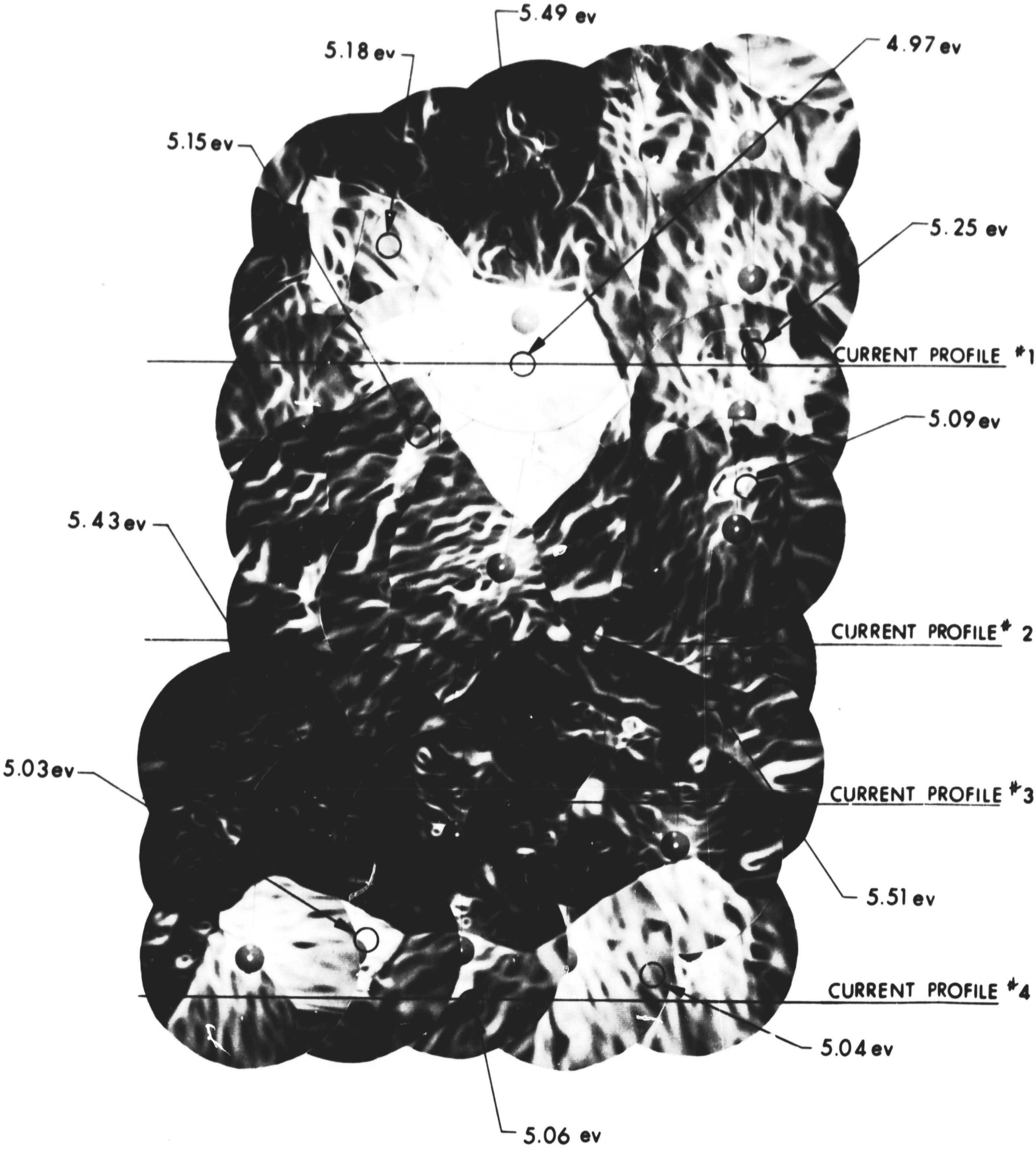

7118-Final

Foldout FRAME 1

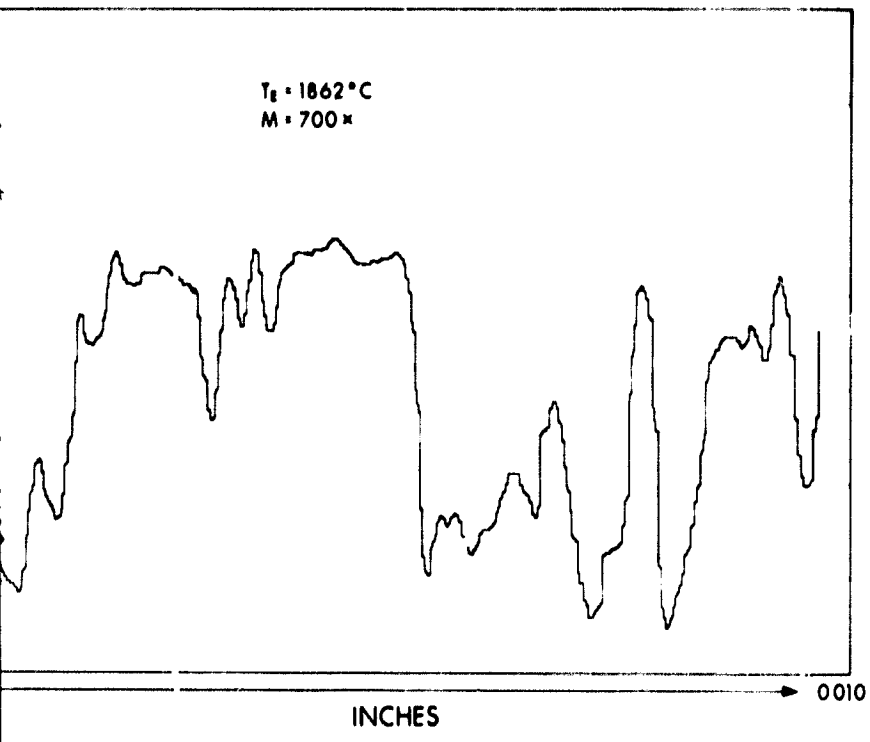

CURRENT PROFILE NO. 1

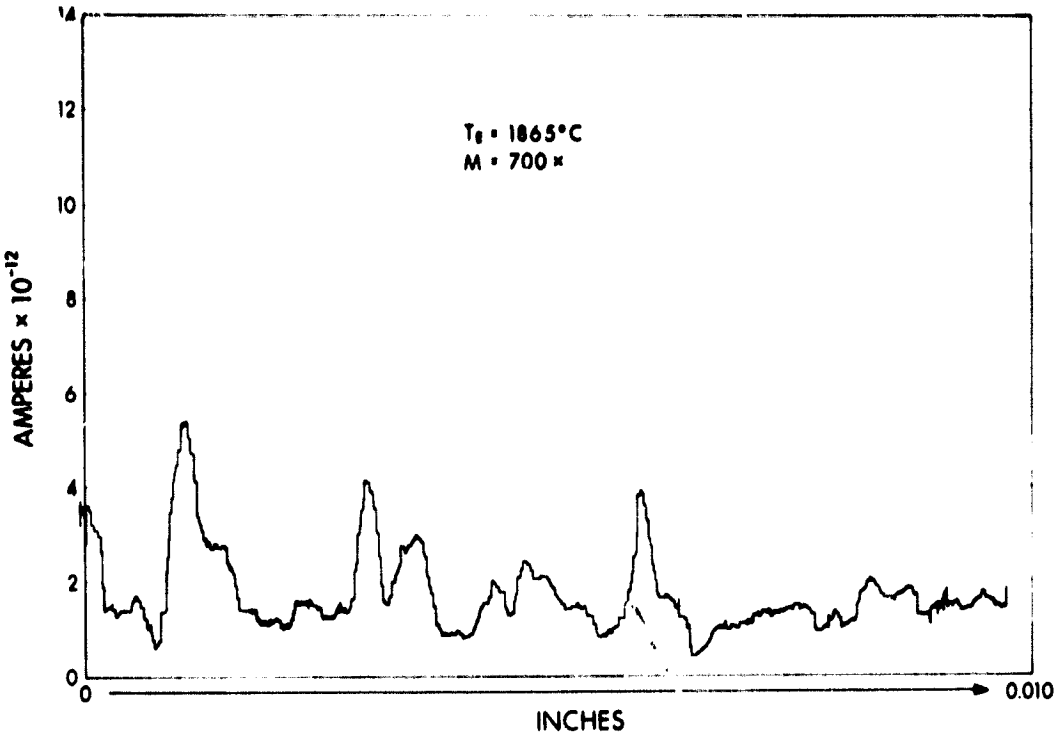

CURRENT PROFILE NO. 2

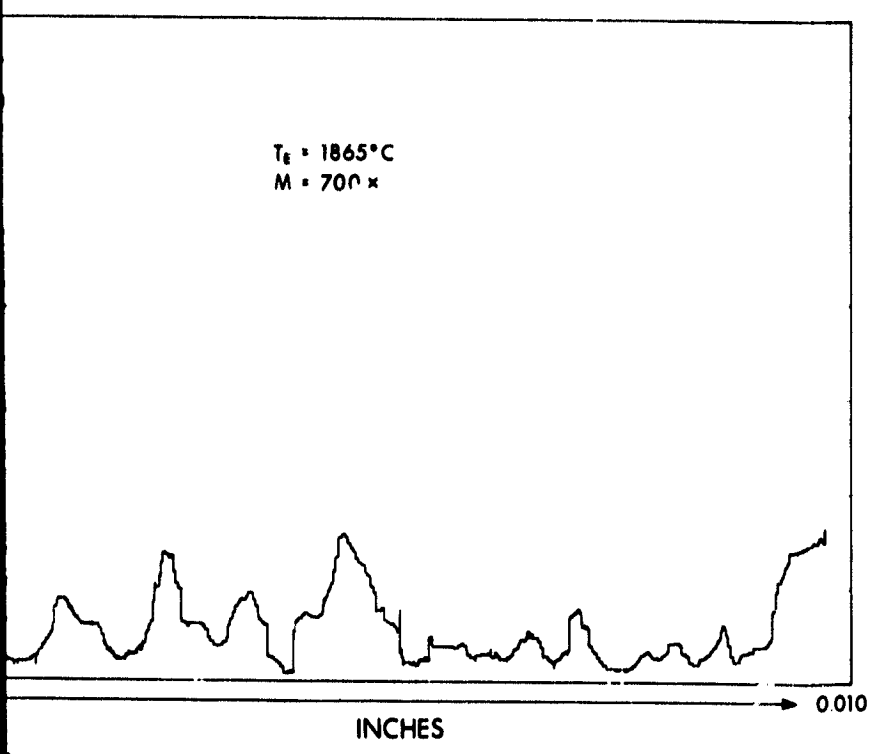

CURRENT PROFILE NO. 3

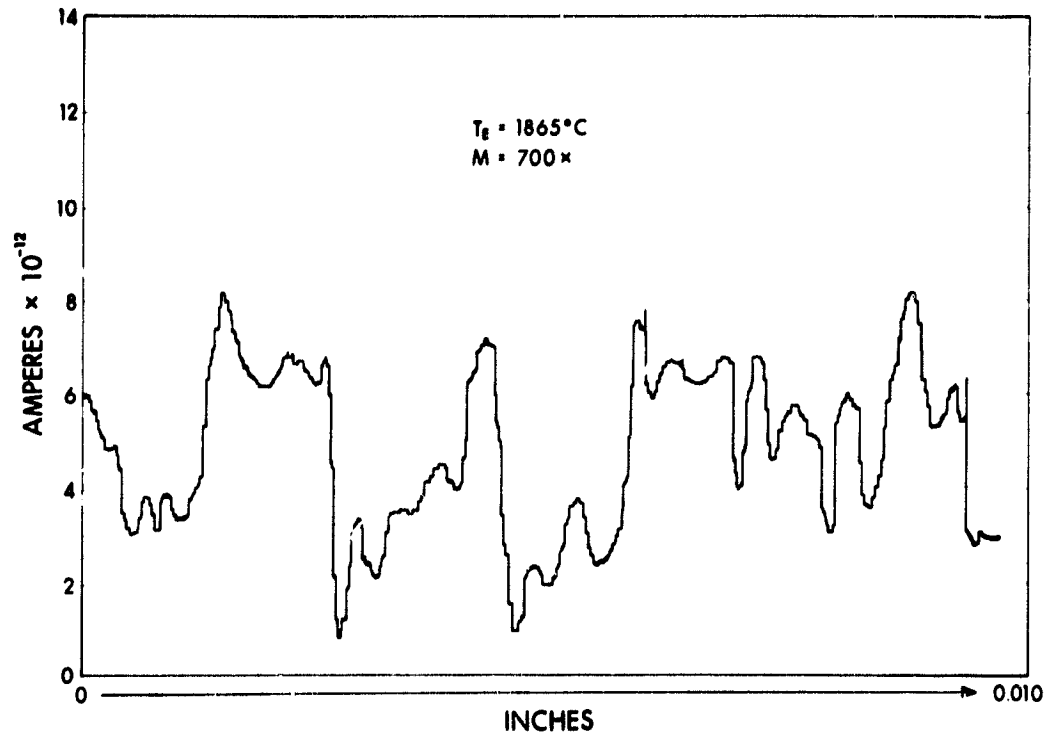

CURRENT PROFILE NO. 4

Figure 32. Mapped Composite of Sample Area in Figure 23 with Current Profiles

FRAME 2

To better delineate the variation of emission associated with the irregularities displayed by the surface, current profiles were taken. By recording the current on a calibrated X-Y plotter, a graphic presentation of the high and low emission areas can be shown. The axes and their emission profiles measured are also shown in Fig. 32. This graphic technique substantiates that the emission is high in the light regions and low in the dark regions. Also, it indicates that there are regions of high emission in predominantly dark areas that are on the order of 0.0001 inch or less in width.

A typical emission profile comparing two magnifications is shown in Fig. 33. This technique of emission profiles has been used by other investigators, such as D. Schnek in 1935 (Ref. 14).

Emission profiles were taken across the sample as shown in Fig. 28 and graphically analyzed to determine if there was any change in the average emission characteristics of the sample. Figure 34 compares the emission profiles before and after electro-etching. The analysis showed that the average emission had not changed, although there were changes in the characteristics of individual grains; in some grains the emission was decreased, where in others the emission increased, but the <u>overall</u> characteristic was the same.

Vapor deposited rhenium sample II was then fine polished with Linde alumina powders, A, B, and C. It was returned to the emission microscope for determination of the effective work function by the scanning technique. Thirty-four scans were taken, each scan being 0.2 inch long. After the completion of a given scan, the sample was moved 0.01 inch perpendicular to the scan direction, and the procedure was repeated. The scans were produced by driving the sample at a constant rate, with the X axis of an X-Y recorder being driven simultaneously and proportionally to the sample by means of a variable resistor. The corresponding current measured with the Faraday Cage was recorded on the Y axis.

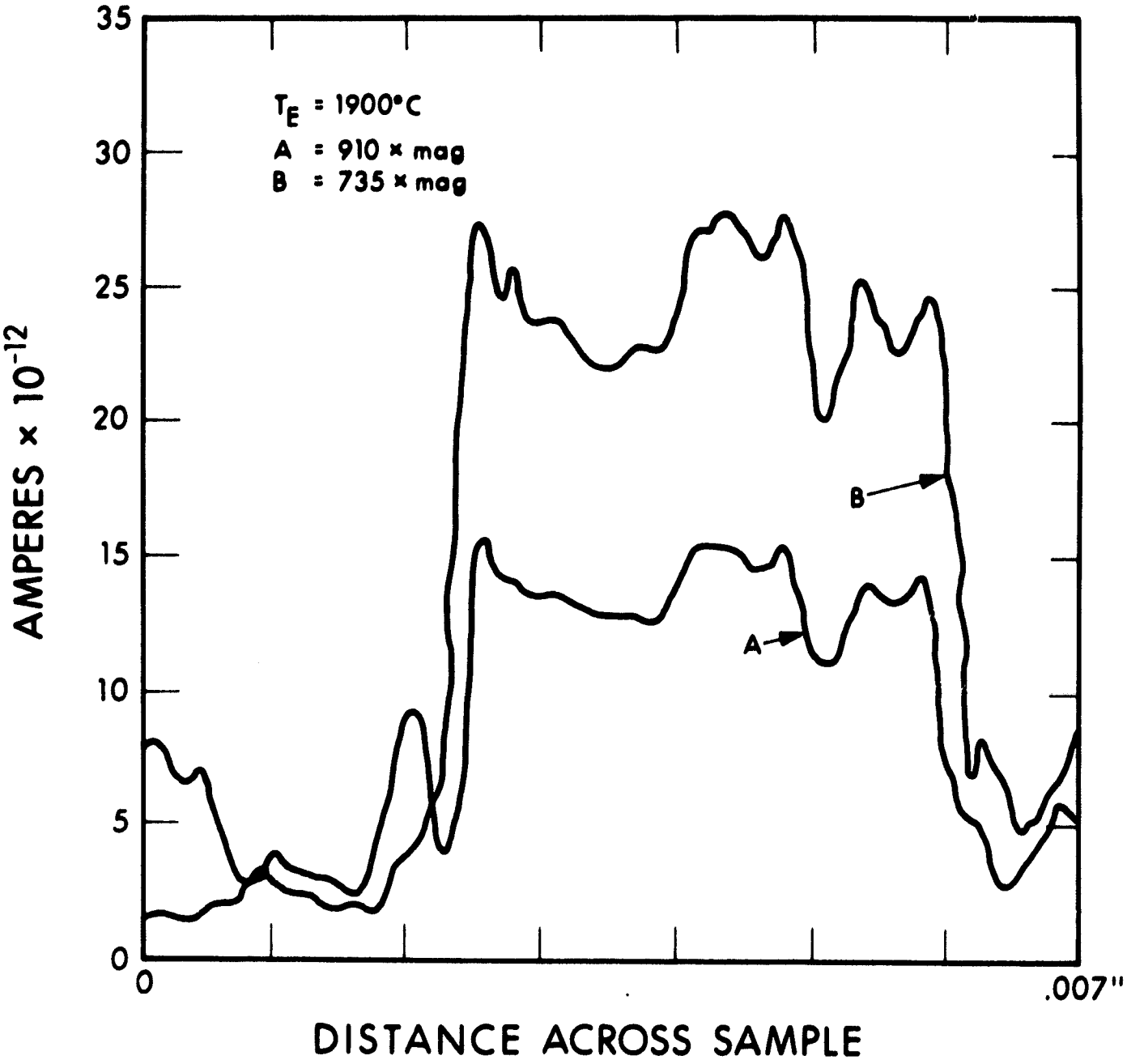

Figure 33. Emission Profiles: (A) 910X Mag, (B) 735X Mag

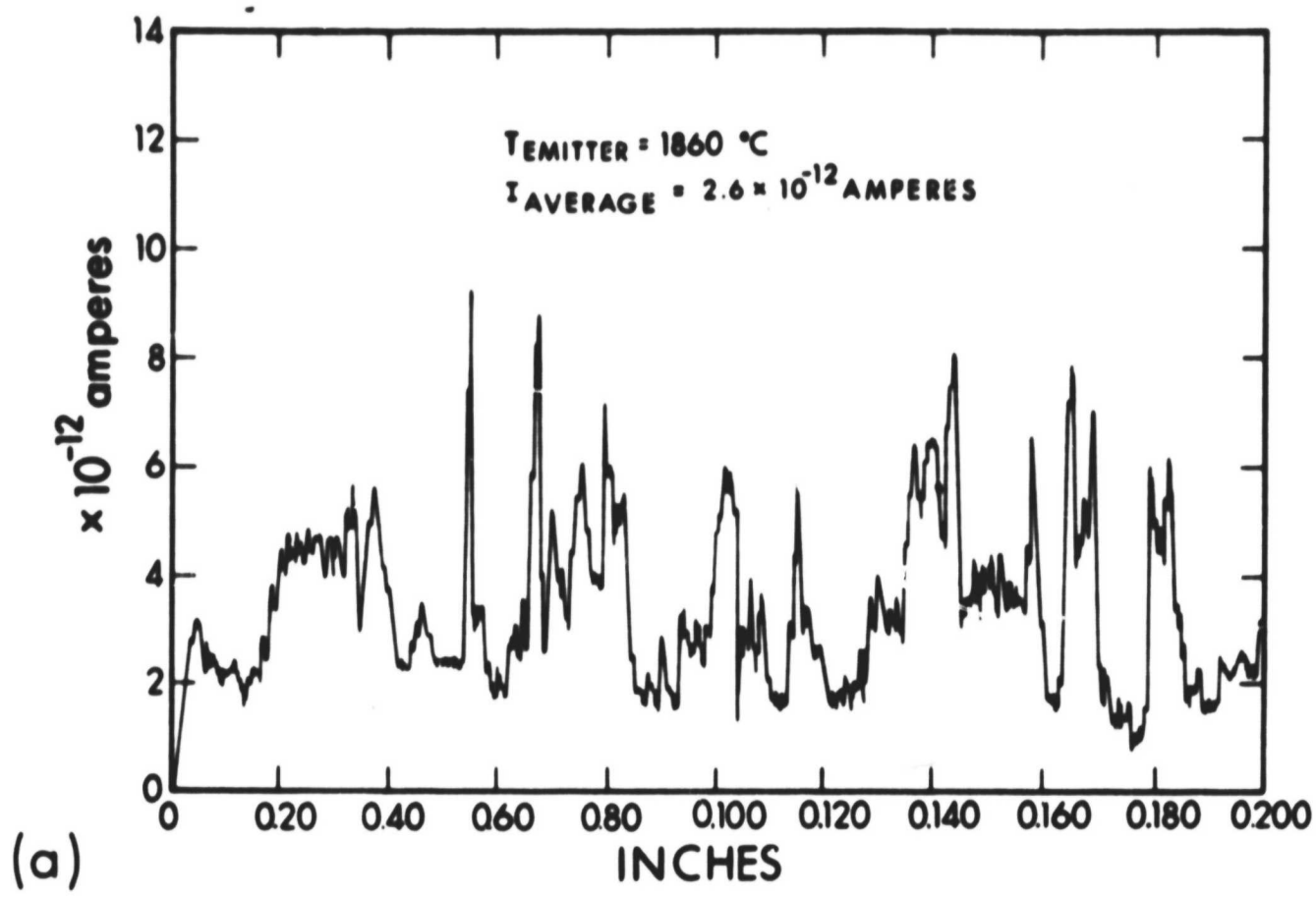

(a)

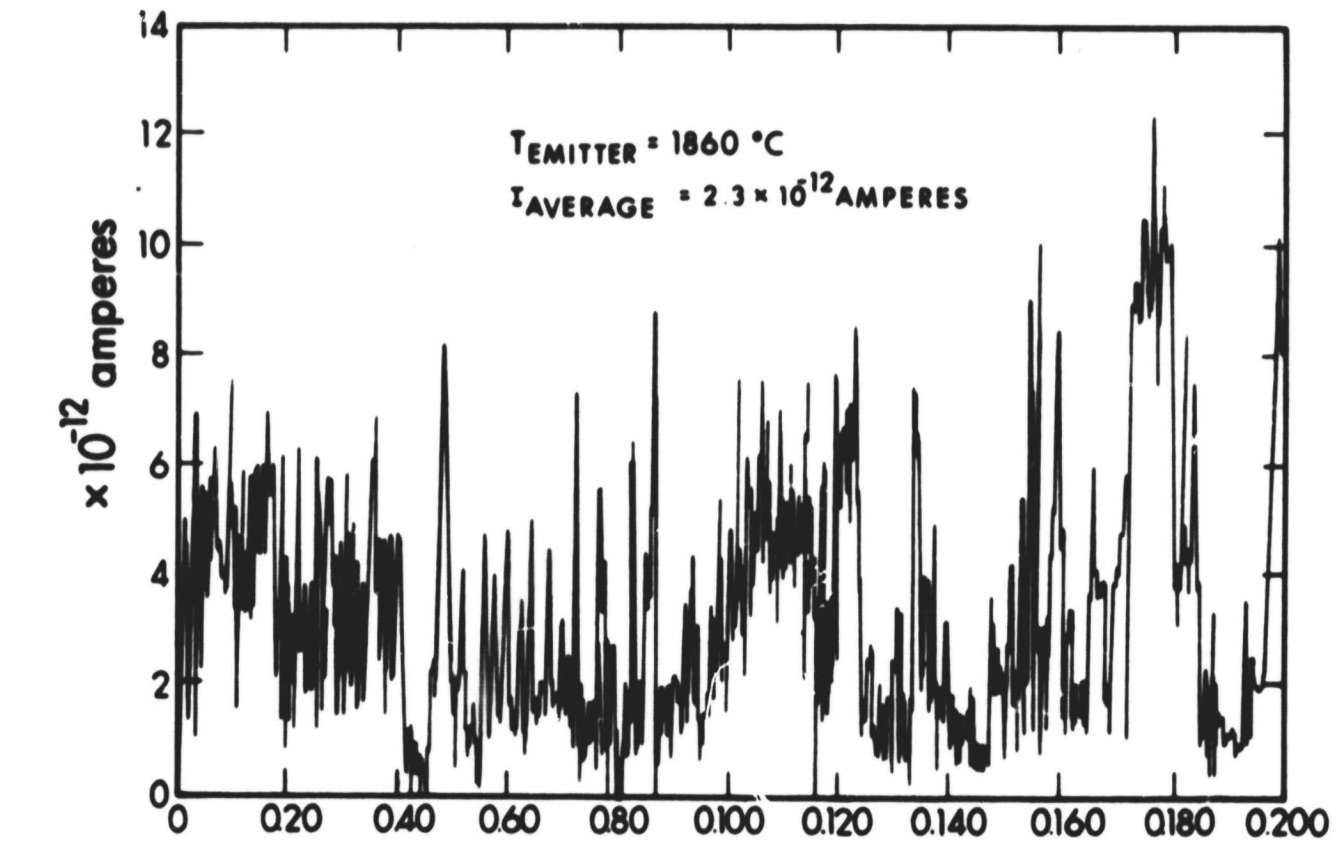

(b)

7118-Final

Figure 34. Emission Profile, Before (a) and After (b) Electro-Etching Vapor-Deposited Rhenium Sample II

The noise level of the system is 5×10^{-14} amp. The average effective work function for each scan was determined, and these are reported in Table X. The average effective work function for all scans taken at approximately 2153°K is 5.30 eV. The average value for those at 2093°K is 5.32 eV, and for those at 2085°K, it is 5.31 eV.

TABLE X

AVERAGE EFFECTIVE WORK FUNCTION VALUES OF FINE-POLISHED VAPOR-DEPOSITED RHENIUM SAMPLE II, DETERMINED FROM ELECTRON EMISSION MICROSCOPE SCANS

Temperature, °K	J_o, A/cm^2	$\bar{\phi}$, eV
2156	3.82×10^{-4}	5.25
2154	3.02×10^{-4}	5.29
2155	2.4×10^{-4}	5.34
2155	3.34×10^{-4}	5.27
2153	1.94×10^{-4}	5.37
2153	2.8×10^{-4}	5.30
2143	2.04×10^{-4}	5.30
2153	3.48×10^{-4}	5.25
2155	3.16×10^{-4}	5.29
2092	1.57×10^{-4}	5.23
2093	1.19×10^{-4}	5.31
2095	1.31×10^{-4}	5.29
2093	1.38×10^{-4}	5.27
2095	1.32×10^{-4}	5.28
2092	1.2×10^{-4}	5.30
2089	0.96×10^{-4}	5.28
2093	8.8×10^{-5}	5.36
2093	9.56×10^{-5}	5.36
2093	9.28×10^{-5}	5.35
2093	8.6×10^{-5}	5.36

TABLE X

AVERAGE EFFECTIVE WORK FUNCTION VALUES OF FINE-POLISHED VAPOR-DEPOSITED RHENIUM SAMPLE II, DETERMINED FROM ELECTRON EMISSION MICROSCOPE SCANS (contd)

Temperature, ^{o}K	J_o, A/cm^2	$\bar{\phi}$, eV
2093	8.7×10^{-5}	5.36
2090	8.94×10^{-5}	5.34
2093	1.45×10^{-4}	5.27
2094	7.43×10^{-5}	5.39
2093	1.10×10^{-4}	5.32
2094	1.21×10^{-4}	5.30
2085	0.92×10^{-4}	5.32
2086	0.88×10^{-4}	5.33
2085	0.96×10^{-4}	5.32
2085	1.49×10^{-4}	5.23
2083	1.05×10^{-4}	5.30
2085	0.91×10^{-4}	5.33
2085	0.895×10^{-4}	5.33
2085	1.01×10^{-4}	5.31

The effective work function of fine polished polycrystalline rhenium sample II has also been determined by electron emission microscope scans. Nineteen scans were taken; the scanning procedure was the same as that described above for the vapor-deposited rhenium. The average effective work function for each scan was determined, and these are reported in Table XI. The average effective work function for all the scans is 5.24 eV.

TABLE XI

AVERAGE EFFECTIVE WORK FUNCTION VALUES OF FINE-POLISHED POLYCRYSTALLINE RHENIUM SAMPLE II, DETERMINED FROM EMISSION MICROSCOPE SCANS

Temperature, ^{o}K	J, A/cm^2	$\bar{\phi}$, eV
2143	3.5×10^{-4}	5.24
2143	4.73×10^{-4}	5.18
2143	1.61×10^{-4}	5.38
2143	6.03×10^{-4}	5.14
2138	4.55×10^{-4}	5.19
2143	4.9×10^{-4}	5.18
2143	5.42×10^{-4}	5.15
2143	2.17×10^{-4}	5.32
2143	5.65×10^{-4}	5.14
2143	1.82×10^{-4}	5.36
2148	3.48×10^{-4}	5.24
2143	2.6×10^{-4}	5.29
2143	2.1×10^{-4}	5.33
2143	5.94×10^{-4}	5.14
2143	2.61×10^{-4}	5.29
2143	2.68×10^{-4}	5.28
2143	2.72×10^{-4}	5.28
2143	7.04×10^{-4}	5.11
2143	3.15×10^{-4}	5.26

Table XII is a list of the average effective work functions as determined by emission microscope scanning techniques and by vacuum emission vehicle measurements, for various electrode surface preparations, taken at approximately the same electrode temperature. All values are from rhenium sample II, one side of which is polycrystalline, with the vapor deposition on the opposite side of the sample.

TABLE XII

EFFECTIVE WORK FUNCTION VALUES, ϕ_{eff} ±0.04 eV, FOR POLYCRYSTALLINE RHENIUM SAMPLE II AND VAPOR-DEPOSITED RHENIUM SAMPLE II FROM EMISSION MICROSCOPE AND VACUUM EMISSION VEHICLE MEASUREMENTS FOR VARIOUS ELECTRODE SURFACE PREPARATIONS

	Vapor-Deposited, Diamond Lapped	Vapor-Deposited, Electro-Etched	Vapor-Deposited, Finely Polished	Polycrystalline, Finely Polished
Emission	2158°K	2158°K	2153°K	2143°K
Microscope	5.28 eV	5.28 eV	5.30 eV	5.24 eV
Vacuum				
Emission	2148°K	2198°K	2148°K	2159°K
Vehicle	5.09 eV	5.04 eV	5.18 eV	5.01 eV

The average effective work functions from emission microscope measurements for vapor-deposited rhenium are within experimental error for all surface preparations. The differences between the work function value for finely polished polycrystalline rhenium and vapor-deposited rhenium, regardless of surface finish, are all within experimental error, although the effective work function for polycrystalline rhenium is lower by at least 0.04 eV. The results from emission microscope measurements thus indicate that one surface preparation does not appear to produce a higher effective work function than another.

The effective work functions determined from vacuum emission vehicle measurements for both vapor-deposited and polycrystalline rhenium are practically all within experimental error, with the finely polished vapor-deposited surface being higher by 0.09 eV than the diamond lapped vapor-deposited surface, 0.14 eV higher than the electro etched vapor-deposited surface, and 0.17 eV greater than the finely polished polycrystalline surface.

The difference in effective work function between the two measu ement methods as a function of surface preparation is approximately 0.23 eV, the emission microscope indicating the higher value for work function in each case.

H. F. Webster (Ref. 3) has shown that large changes in effective work function are caused by a relatively small part of a surface consisting of facets of lower work function. For example, with a two-facet model with work functions of 6 and 4.2 volts for the two areas, when the fraction of the surface with a work function of 4.2 volts is 0.1, the effective work function of the surface is only 4.5 volts. When the fraction of the surface with a work function of 4.2 volts is 0.001, the effective work function is only about 5.3 volts. This reasoning would thus indicate that many sweeps would be necessary to cover the majority of the low work function grains in samples such as those measured in the emission microscope by the scanning technique. Greatly increasing the number of scans might possibly lower the effective work function values measured in the emission microscope to more closely agree with the effective work functions determined from vacuum emission vehicle measurements where all grains contribute to the average effective work function.

SECTION 3

PERFORMANCE STUDIES

3.1 VARIABLE PARAMETER TEST VEHICLE

Two variable parameter test vehicles of the same basic design but incorporating different sets of electrode materials were tested. The first, and most extensively studied set, was polycrystalline rhenium/polycrystalline molybdenum; the second set was vapor-deposited rhenium/vapor-deposited rhenium.

A total of 900 hours of operation was provided by these two test vehicles which were tested to cover the range of thermionic parameters as follows:

Interelectrode spacing	-	0.0001 inch to 0.026 inch
Cesium reservoir temperature	-	280°C to 500°C
Emitter temperature (true hohlraum)	-	1327°C to 2200°C
Collector temperature	-	640°C to 980°C

Experimental data obtained from the vehicle testing established that a higher bare work function material yields lower cesiated work functions and subsequent higher converter power output. Of equal importance was the data which also established that a cesium pressure-interelectrode spacing product of 16.0 ±0.8 mil-torr optimizes the converter output independent of emitter temperature, emitter work function, and collector work function.

The paragraphs which follow describe the basic and detailed design of the test vehicle, the low temperature emitter performance from polycrystalline rhenium electrodes, and limited performance from vapor-deposited rhenium electrodes.

3.1.1 VARIABLE PARAMETER TEST VEHICLE DESIGN

Before a detailed design and thermal analysis of a variable parameter test vehicle could begin, a basic decision concerning temperature measurement was required. A design which allowed the accurate determination of emitter (cathode) temperatures had to be selected. Due to the high-temperature instability of thermocouple measurements during long term operation (a result of material diffusion at the bimetal junction), a pyrometric method of measurement, utilizing a 10:1 blackbody sight hole, was chosen. Since the largest contribution to measurement inaccuracy in this method is extraneous radiation, a device geometry was selected which allowed an unobstructed view of the blackbody hole by a micro-optical pyrometer. This geometry is identical to the plane-parallel converter wherein the blackbody hole is located in the circumference of the emitter and at right angles to the filament heater.

Based on these considerations, the design geometry utilizes a concentric guard ring and a collector barrel with exposed emitter. Figure 35 shows the geometry of the vehicle. An added benefit of this design is the elimination of a "parasitic" cesium reservoir which occurs when a location within the device approaches the reservoir temperature. By keeping the vehicle compact, with the bellows, ceramic-metal seals, and guard ring concentric to the collector barrel, the device proper will operate at least 150^{o}C higher than the reservoir.

Heat transfer calculations and experiments based on the range of thermionic parameters previously listed have indicated a collector length of 1 inch for a 2.0 cm^{2} cross section. Provisions for cooling and heating the collector are available on the radiator strap.

Figure 36 is a layout of the variable parameter test vehicle subassemblies and components. The final assembly of the vehicle utilizes an approach wherein as many subassemblies as possible are preassembled before being

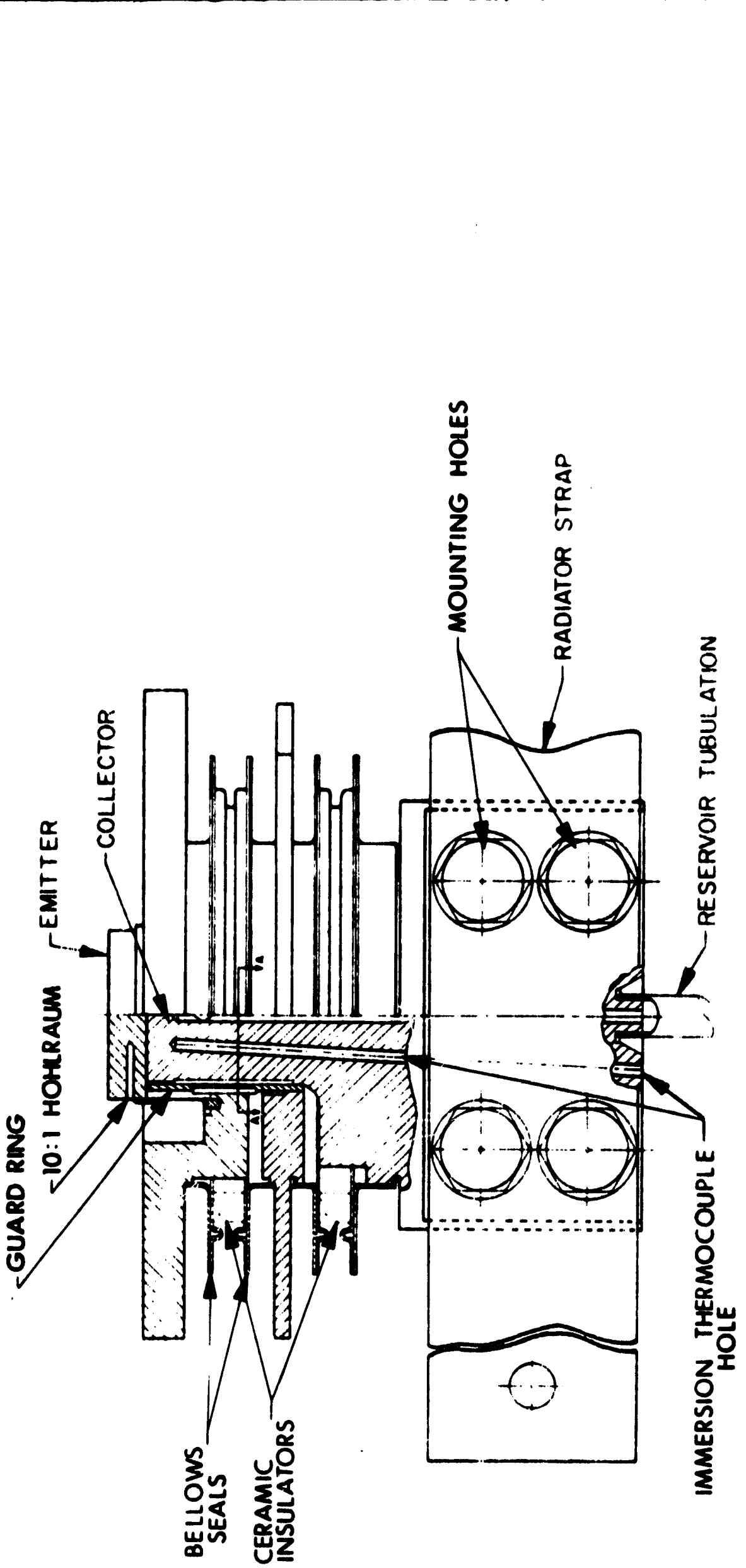

Figure 35. Variable Parameter Test Vehicle, Basic Design

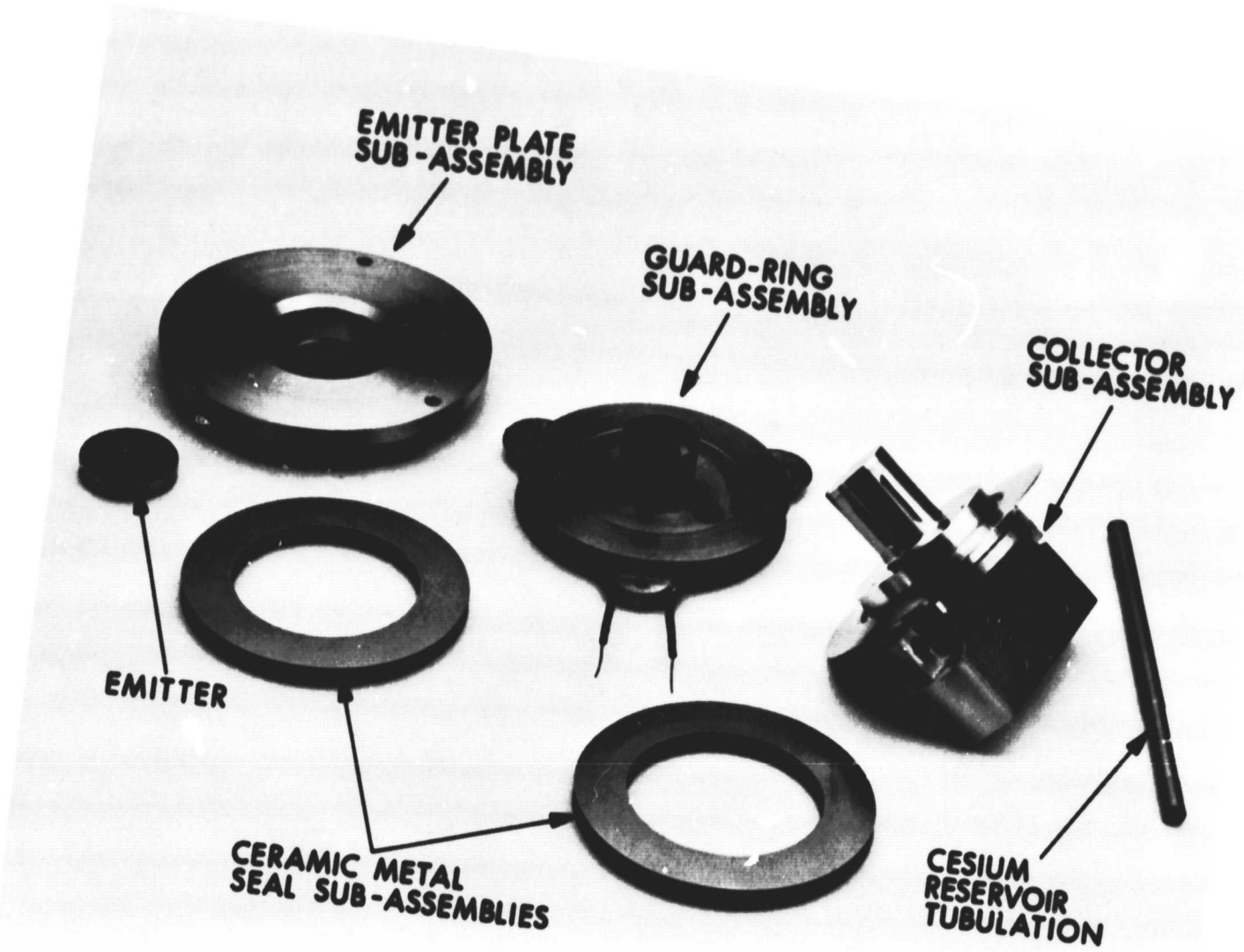

Figure 36. Variable Parameter Test Vehicle Subassemblies and Components

electron beam welded into the test vehicle final configuration. The key to the fabrication of the test vehicle was the development of a single-convolution, refractory-metal bellows formed by the electron beam welding of niobium flanges to prefabricated niobium-alumina seal subassemblies. The advantage of this method is the use of a high-purity, high-temperature bellows assembly which does not compromise the design objectives with ferrous alloys exposed to a device interior of high pressure cesium vapor. A bellows subassembly was fabricated and measured to have an excursion greater than 0.040 inch without failure. The same assembly was then cycled 3500 times at a 0.025 inch displacement, leak-checked, found leak-tight, and cycled to destruction, which occurred at 8000 cycles. The critical juncture in the test vehicle fabrication is the electron beam welding of these seal subassemblies to mating parts of the emitter and collector subassemblies. However, welded joints are easier to make on one-of-a-kind devices, than seal brazing a three-electrode system, particularly if seal brazing is the final assembly step.

The choice of either a vapor-deposited or polycrystalline rhenium emitter automatically selected rhenium as the emitter support material. Briefly the argument for a rhenium emitter/rhenium support is as follows: First, since the support structure and emitter are pierce-welded on an electron beam welder, both parts are brought to the melting point in a localized area. Rhenium forms brittle inter-metallic compounds and alloys with almost every common high-temperature material candidate, especially at its melting point. The solution is therefore to also make the envelope out of rhenium. Second, even if the material or materials were found to circumvent this problem, the high temperature and long-time requirements for converter operation would most surely lead to diffusion of such dissimilar materials. For example, it has been EOS's experience that a tantalum support structure/rhenium emitter leads to emitter surface contamination and work function changes within 200 hours at emitter temperatures near 2000^{o}K.

The test vehicle is comprised of four major subassemblies: the emitter plate subassembly, the guard ring subassembly, the collector subassembly, and the ceramic-metal seal subassemblies.

The emitter plate subassembly, which consists of the molybdenum emitter plate and rhenium envelope, was titanium brazed at 1700°C, although backup assemblies were brazed with vanadium at 1900°C. Both brazes were leak-tight; however, the vanadium braze is probably more reliable since there are fewer phase transitions to contend with than there are in titanium.

The guard ring subassembly fabrication procedure consisted of brazing the molybdenum guard ring barrel to the molybdenum guard ring support plate and joining two niobium bellows flanges to the top and bottom of the plate. All of these joints were titanium brazed at 1700°C.

The collector subassembly is comprised of a 0.040-inch rhenium disk vanadium-brazed to the surface of the molybdenum collector. A niobium collector flange and cesium reservoir tubulation were subsequently titanium-brazed. After this braze, the collector surface was machined to the finish dimensions. The collector surface was lapped, cleaned, and vacuum-fired at 800°C for 20 hours to remove any trace impurities.

Upon completion of these subassemblies, the final assembly proceeded wherein all items were re-leak-checked on a 2×10^{-10} cc-atm/sec sensitive mass spectrometer leak detector and stacked for electron beam welding at the periphery of the flanges and seals. During stacking, three specially machined molybdenum screws were used to mechanically fasten the guard ring and collector at a common reference plane so that thermal expansion of both members will be identical during operation of the vehicle. Electrical isolation was provided by ceramic sleeve inserts. This method of guard ring location has proven successful throughout the operation of two test vehicles. The collector and

guard ring maintained concentricity while the collector surface remained at least 0.0003 inch above the guard ring surface, a condition preset during final assembly to allow the interelectrode spacing to be measured only between emitter and collector.

After the bellow seals were welded, the structure was mounted in a jig which expanded the bellows by 0.005 to 0.008 inch, and the rhenium emitter was inserted into the rhenium support structure and electron beam welded into place. The weld is a pierce-type joint requiring no burn-off lips or other projections for effecting the weldment. The emitter is purposely allowed to be in contact with the collector surface (with bellows expanded) to achieve controlled parallelism at the emitter-collector operating temperatures. If the bellows were not preexpanded, it would be necessary to effect the bellows action in the ceramic-metal seal alone to achieve the condition of a controlled short, since there is always an inherent thermal expansion in the envelope of 0.003 to 0.005 inch.

Figure 37 illustrates the test vehicle drive mechanism and stainless steel test gantry used to secure the test vehicle for operation. The basic gantry structure consists of three parallel stainless steel rings separated by stainless steel rods. The bottom ring mates with the inside edge of the vacuum test station base plate. The middle ring, actually a disk, supports the return drive mechanism and the test vehicle support fixture. This disk is covered by 10 sheets of 0.002-inch-thick dimpled molybdenum heat shields to limit the temperature of the dial indicators as well as the disk itself, since the disk serves to support the test vehicle. Two molybdenum brackets are bolted to the collector root and terminate on insulated base straps, as shown in the figure. The bolts are made of Inconel-X and contain hand-polished shanks which mate to the insides of collector mounting holes. The bolts are torqued in place at a value of 95 ft-lb to insure even and firm attachment of the test vehicle.

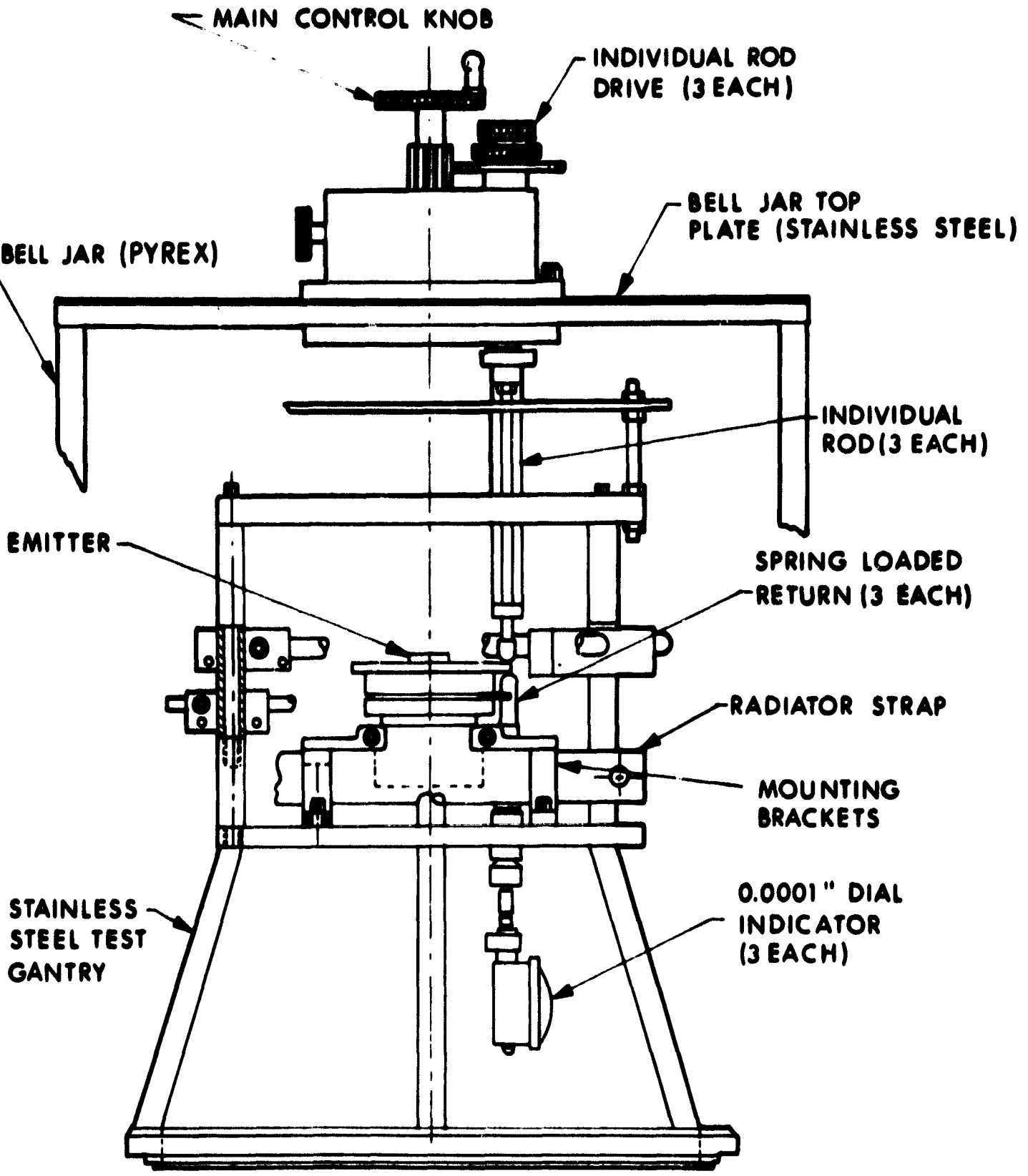

Figure 37. Variable Parameter Test Vehicle, Precision Drive Mechanism, and Gantry

29964

The interelectrode spacing of the variable parameter test vehicle is varied by applying force to three spring-loaded rods which are inserted from the bell jar top plate. These rods apply pressure to the emitter plate. The individual rods are controlled by a differential thread drive to allow independent movement of each rod. One complete rotation of the control nut on the individual rods results in a vertical displacement of 0.002 inch. The three rods can be ganged for uniform excursion controlled by a single drive. One complete rotation of the main control knob results in a uniform displacement of 0.0008 inch by the ganged rods. The return movement is obtained by spring-loaded ceramic rods mounted beneath the emitter plate. These rods maintain a continuous upward force on the bottom of the emitter plate. The measuring device is supported from a second ceramic rod while measuring the movement of the ceramic return rod. This method is temperature compensating and allows the measuring device to indicate only the true mechanical movement of the emitter with respect to the collector, and not the thermal expansion in the support and return rods. The measuring device is a 0.0001-inch dial indicator which may be read to within 0.00005 inch.

In practice, the 0.0001-inch indicators must be replaced after 400 to 600 hours of operation, since their internal moving parts will not permit smooth tracking for longer periods. It should be pointed out that the gages will still register accurate displacements, but the needle movement of the individual indicators track discontinuously, creating nuisance rather than error.

Inconel X was selected for the spring material used throughout the drive mechanism, and has performed satisfactorily at nominal temperatures of 150 to 200°C for over 1800 hours of continuous loading. The other structural materials of the drive mechanism are Type 304 stainless steel and sulfur-free nickel. The alumina rods were selected to provide electrical isolation between the drive mechanism and test vehicle; in addition, they conduct only minimal heat away from the emitter plate.

3.1.2 LOW TEMPERATURE EMITTER PERFORMANCE FROM POLYCRYSTALLINE RHENIUM ELECTRODES*

The characterization of performance from this electrode system at higher emitter temperatures (or 2000°K) has been completed and reported elsewhere (Ref. 15). During this period of operation and test it was determined that the electrode system of rhenium/molybdenum is unstable; that is, high temperature operation of the emitter provides a sufficient amount of evaporated rhenium onto the collector surface to change the work function from a cesium-on-molybdenum system to a cesium-on-rhenium system. Subsequent long term, low emitter temperature operation of the device resulted in the apparent diffusion of the evaporated rhenium into the molybdenum collector substrate, resulting in a collector system consisting of cesium-on-molybdenum. The quantitative difference between these electrode systems is approximately 0.080 volt output, as measured in the test vehicle and reproduced independently in a fixed-spacing converter of rhenium-molybdenum electrodes.

To maintain a stable system of rhenium-rhenium electrodes in the presence of diffusion, the rhenium emitter was periodically operated at temperatures as high as 2200°C for 3 hours (with the cesium reservoir heater turned off) to insure at least a two or three monolayer coverage of rhenium on the collector surface.

The data from a previously examined polycrystalline rhenium/rhenium system compares within 1 or 2 percent of the rhenium/evaporated rhenium-on-molybdenum system. Hence the low temperature data reported for the rhenium/rhenium-on-molybdenum system is considered, within the experimental error, to be a rhenium-rhenium system. Perhaps the most useful data from a variable parameter test vehicle is the voltage output versus interelectrode spacing for a constant load current, constant

*This is actually a polycrystalline rhenium emitter/polycrystalline molybdenum collector system with evaporated rhenium on the collector surface.

emitter temperature, constant collector temperature, and constant cesium vapor pressure. If these element temperatures are truly maintained constant and the spacing between electrodes is precisely determined, some important phenomenological information as well as engineering optimization data is present in one display. For example, it was determined that the pressure-distance product, "pd", at the point of optimum voltage (and power) output was 16.0 ±0.8 mil-torr for a limited selection of output levels at 1735°C emitter temperature.

The first data of interest in the low emitter temperature range (1330°C-1735°C) were voltage output versus interelectrode spacing. Figures 38 through 44 show the data acquired in the low emitter temperature region. All data plotted are dc data taken under steady-state conditions of operation. It is interesting to note the continuous depression of the voltage minimum in these data as a function of decreasing emitter temperature, and the subsequent loss of contact potential difference between emitter and collector. In fact, it may be seen that at the condition of very low emitter temperatures and close spacing a voltage must be applied to support the electron current flow between emitter and collector.

Collector work function measurements were taken from the test vehicle in both the molybdenum and the rhenium-on-molybdenum configurations, the difference between the two at conditions of maximum output being 70 to 80 millivolts. Therefore, from two independent sets of measurements (viz., voltage output versus interelectrode spacing and saturated electron emission) the lower value of cesiated collector work function leads to higher thermionic power output. The increase in converter power output, Δp, due to a decrease in collector work function, ΔE, at constant current is given by

$$\Delta p = I\Delta E, \text{ since } \Delta I = 0$$

73623839

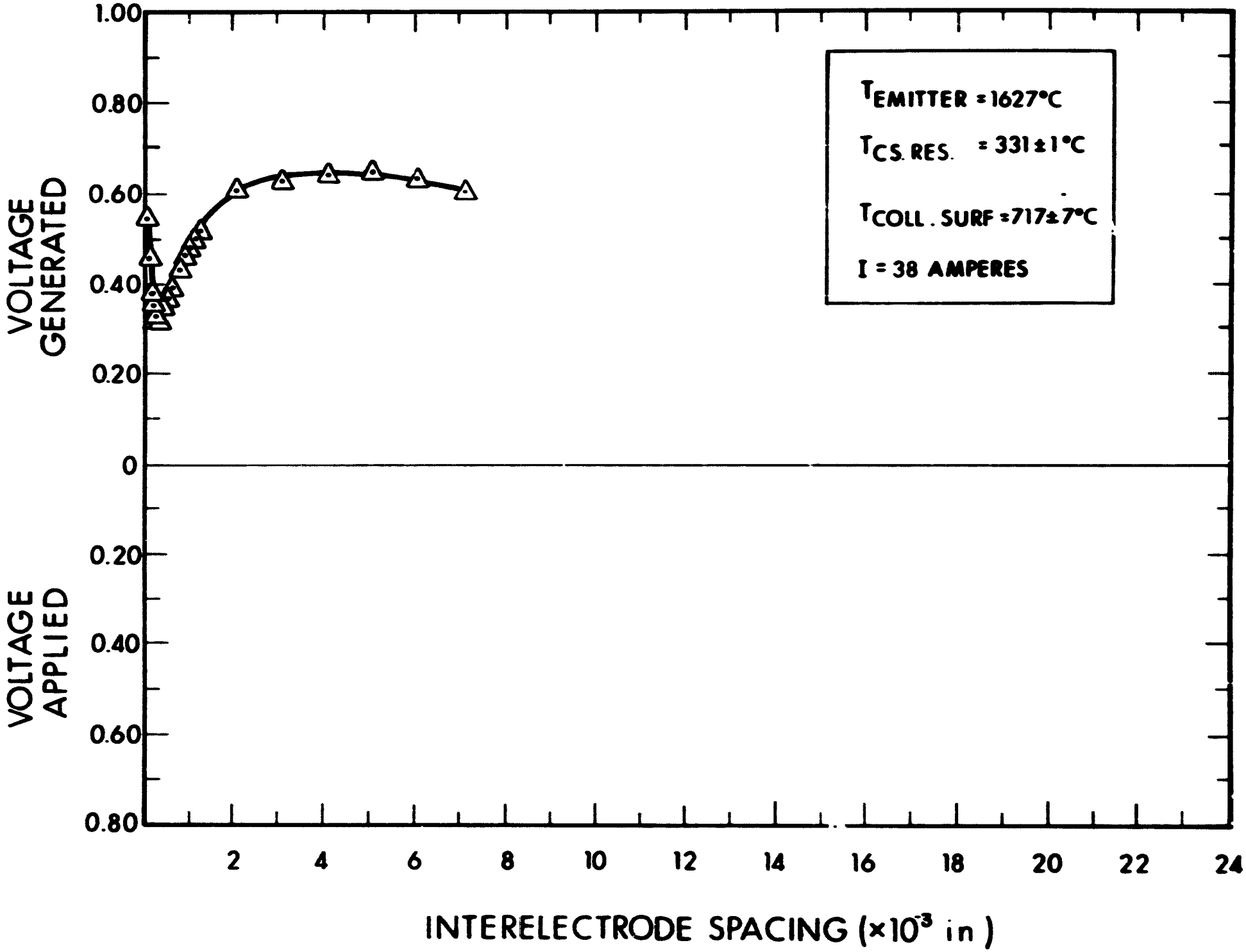

Figure 38. Voltage versus Interelectrode Spacing for $T_E = 1627^{\circ}C$, Nonoptimized Performance (all points are dc data)

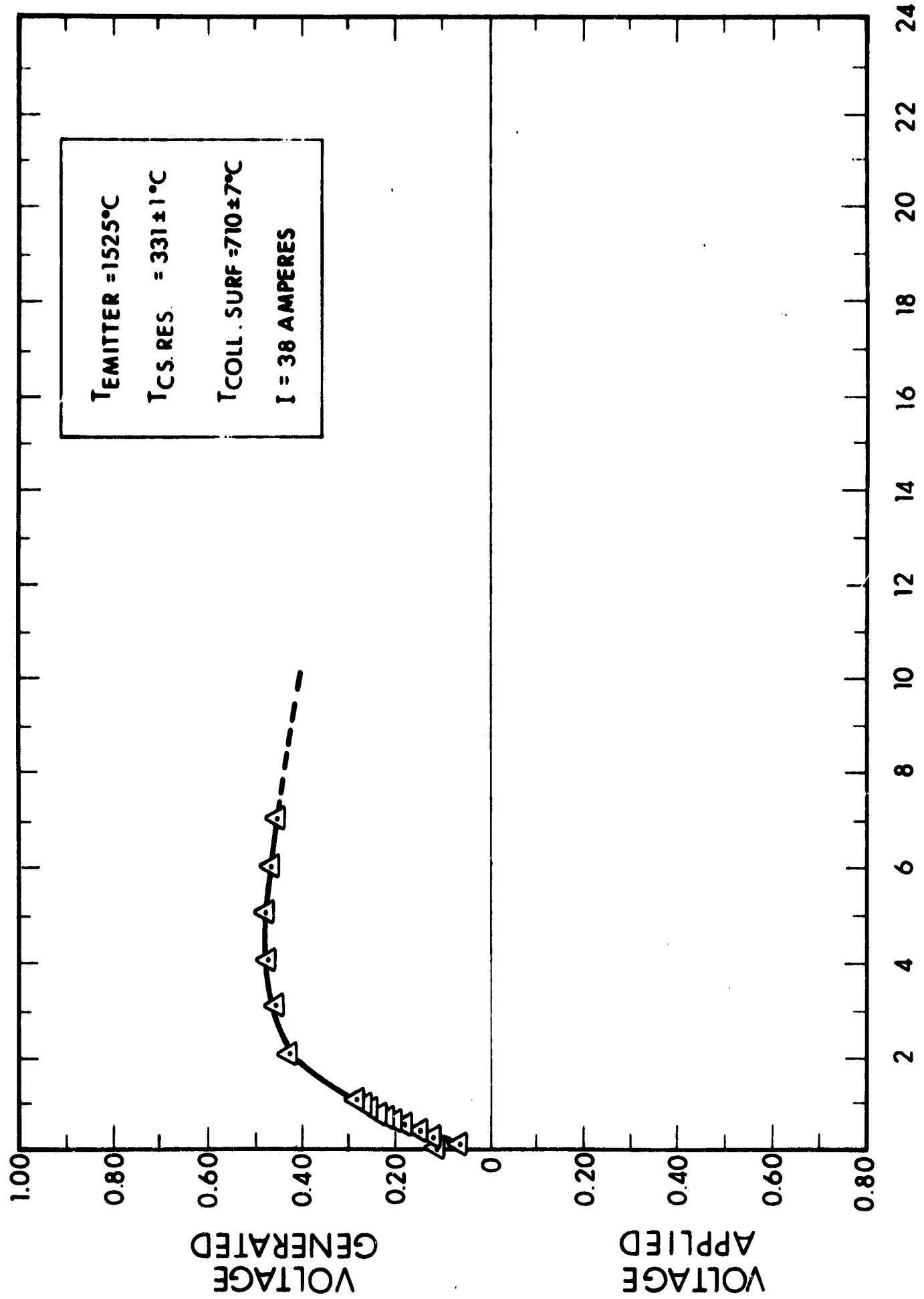

Figure 39. Voltage versus Interelectrode Spacing for T_E = 1525°C, Nonoptimized Performance (all points are dc data)

73623838

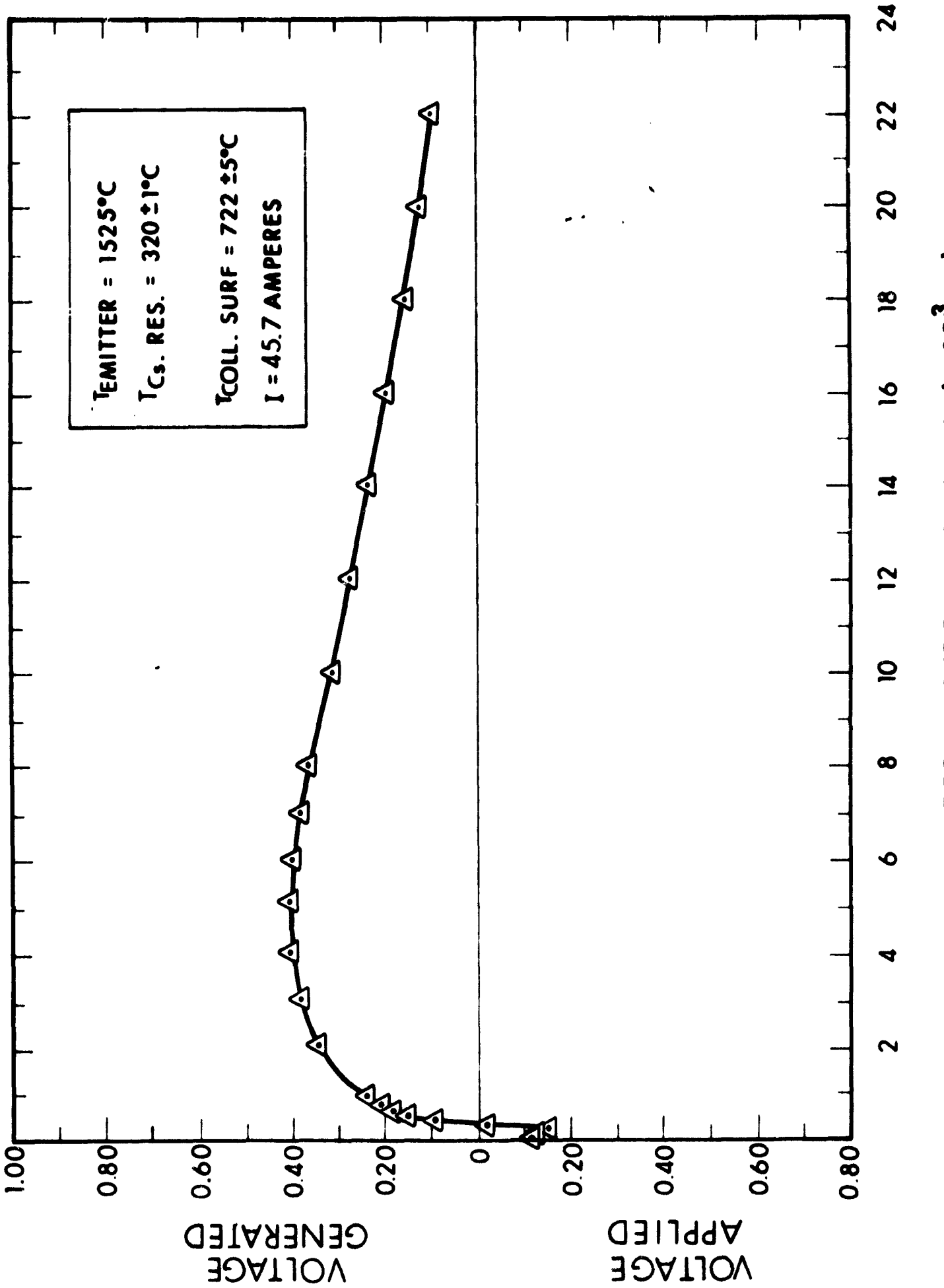

Figure 40. Voltage versus Interelectrode Spacing for T_E = 1525°C, Optimized for 0.40 Volt Output (all points are dc data)

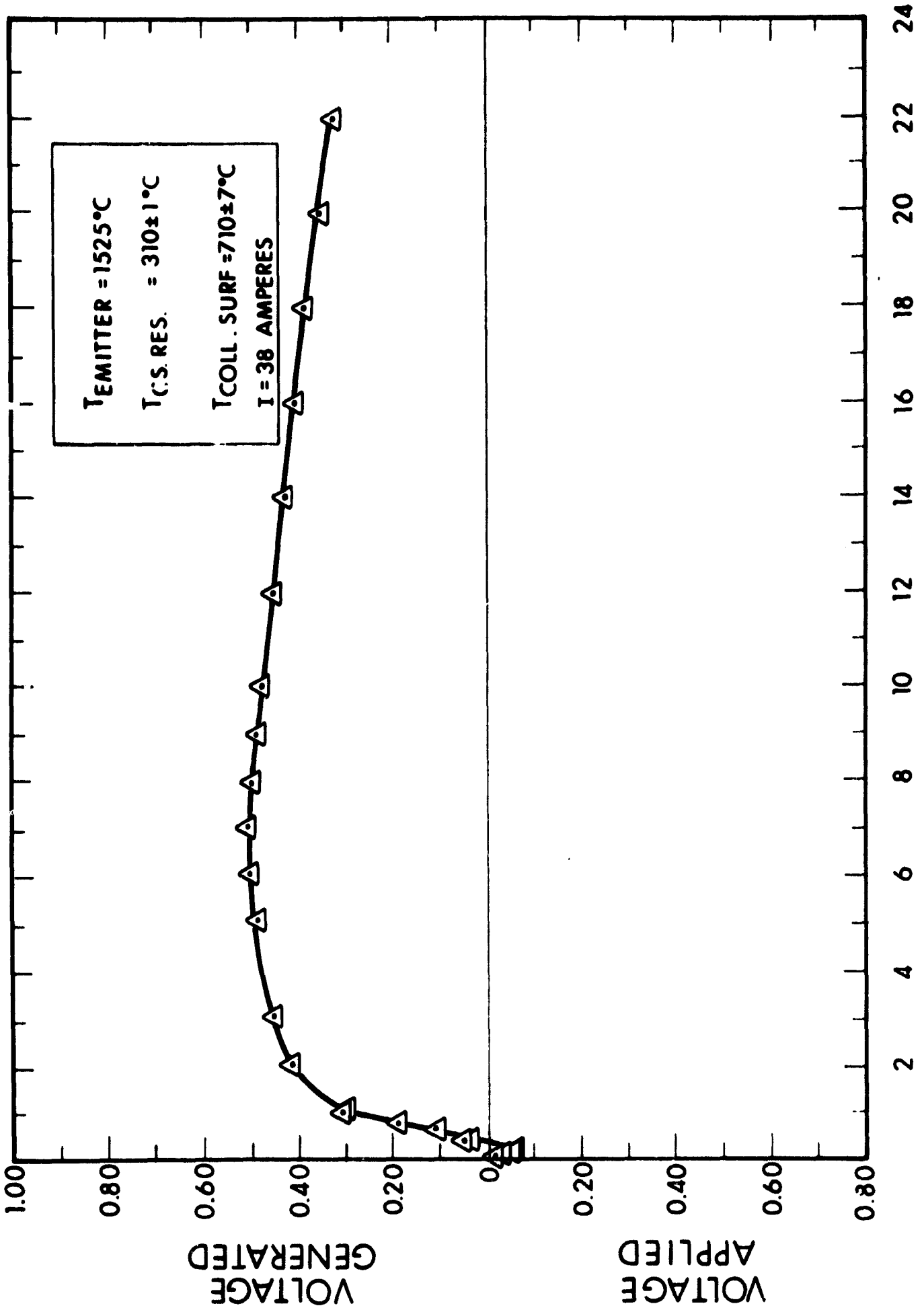

Figure 41. Voltage versus Interelectrode Spacing for T_E = 1525°C, Optimized for 0.50 Volt Output (all points are dc data)

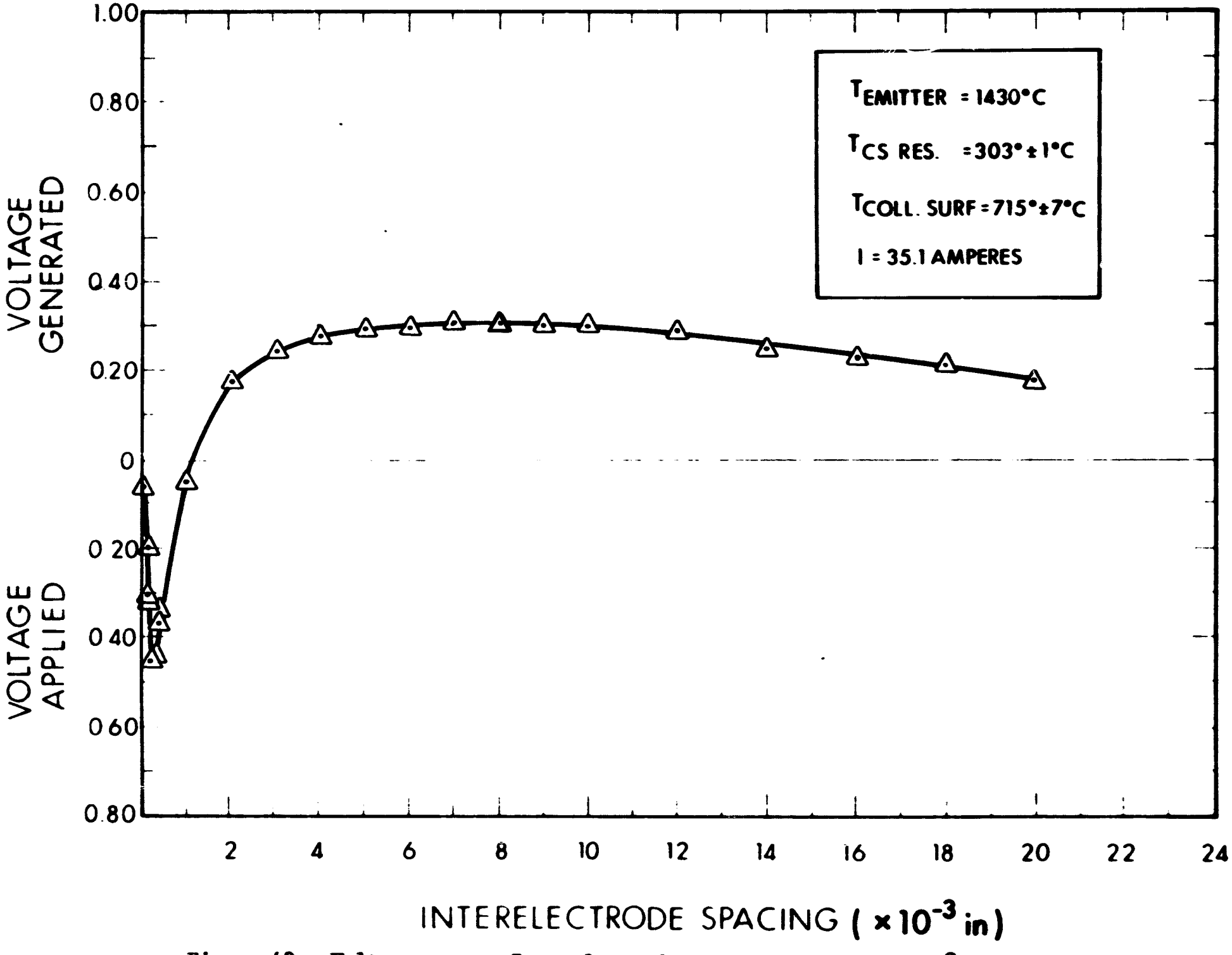

Figure 42. Voltage versus Interelectrode Spacing for T_E = 1430°C, Optimized for 0.30 Volt Output (all points are dc data)

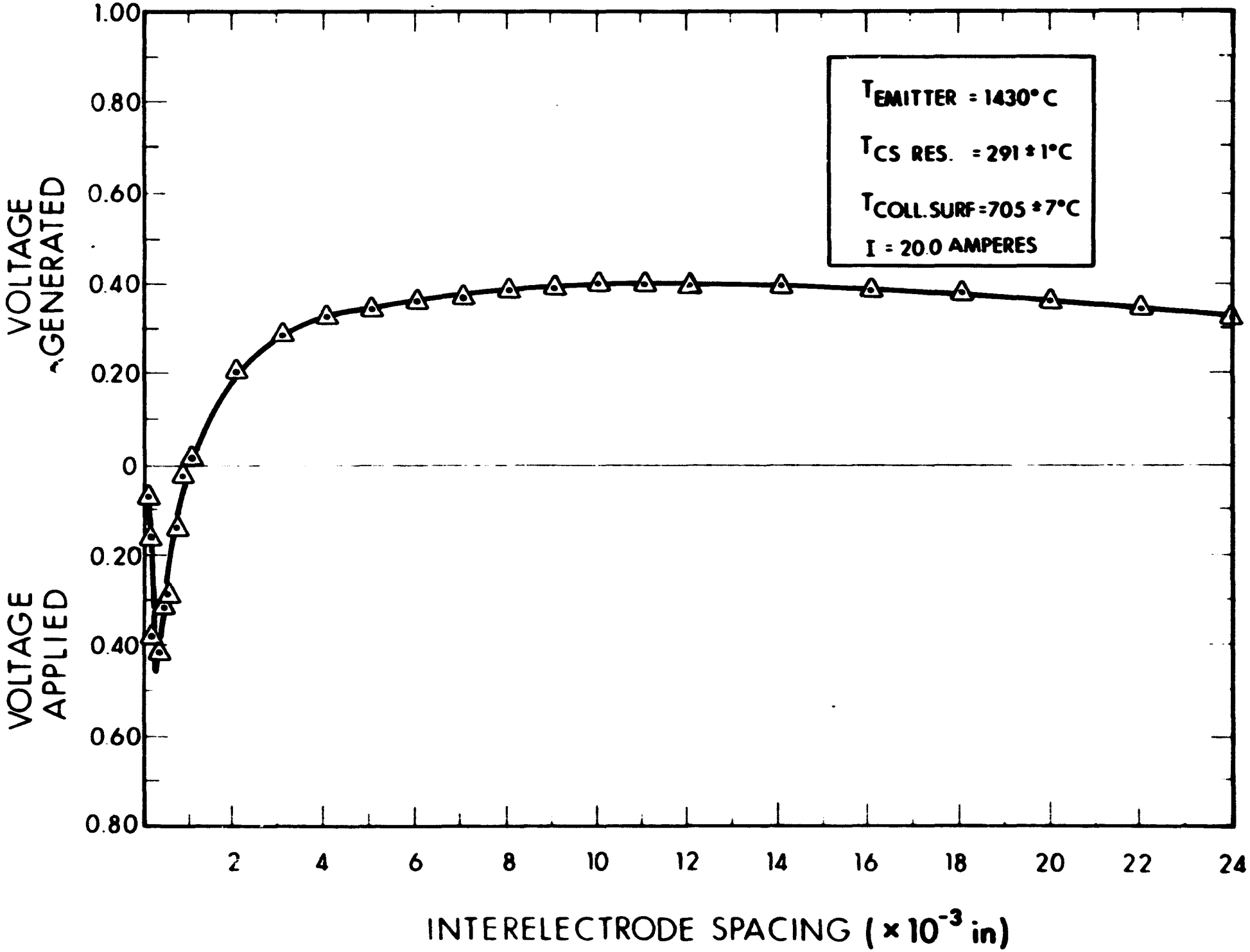

Figure 43. Voltage versus Interelectrode Spacing for T_E = 1430°C, Optimized for 0.40 Volt Output (all points are dc data)

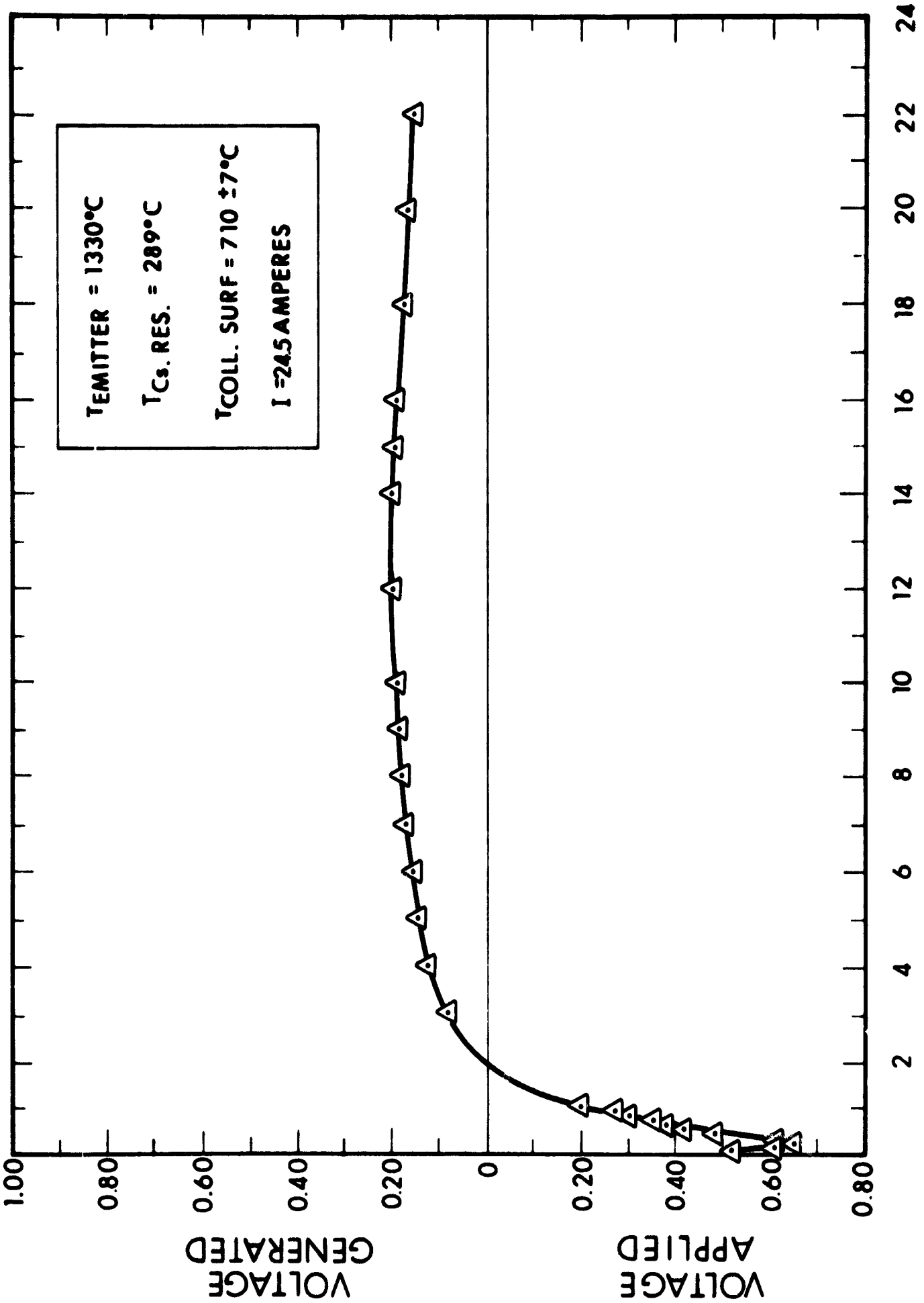

Figure 44. Voltage versus Interelectrode Spacing for T_E = 1330°C, Optimized for 0.20 Volt Output (all points are dc data)

or

$$\frac{\Delta p}{p} = \frac{\Delta E}{E}, \quad \text{since } p = IE$$

Table XIII summarizes the pd products from these curves with three additional sets of data included from previous investigations (Ref. 16). The average pd product from these data is computed to be 16.0 mil-torr ±0.8 mil-torr. It may be noted from the curves and the tabulated data that the pd product is independent of emitter temperature. The optimum pd product is also independent of the collector material as shown in Fig. 45, a comparison curve of the Re-Re and Re-Mo systems.

TABLE XIII

SUMMARY OF PRESSURE-DISTANCE DATA TAKEN FROM INTERELECTRODE SPACING VERSUS VOLTAGE OUTPUT CURVES (FIGS. 38 THROUGH 44)

$T_{emitter}$ (°C)	$T_{cs\ res}$ (°C)	P_{cs} (torr)	d (mil)	pd (mil-torr)
1327	289	1.33	12.5	16.7
1427	291	1.43	11.0	15.7
1427	303	1.96	8.0	15.6
1527	310	2.35	7.1	16.8
1527	320	3.01	5.3	15.9
1527	331	4.02	3.9	15.7
1627	331	4.02	3.9	15.7
1735	331	4.02	3.9	15.7
1735	344	5.30	3.0	15.9
1735	350	6.06	2.7	16.3

Figure 45 demonstrates the central thesis of this program, namely, increased thermionic converter performance attributable to a minimum collector work function. An average difference of 70 to 80 millivolts between the two sets of data is readily seen at the optimum spacing of 3.5 to 3.9 mils. At closer spacings of 0.5 to 2.0 mils the voltage

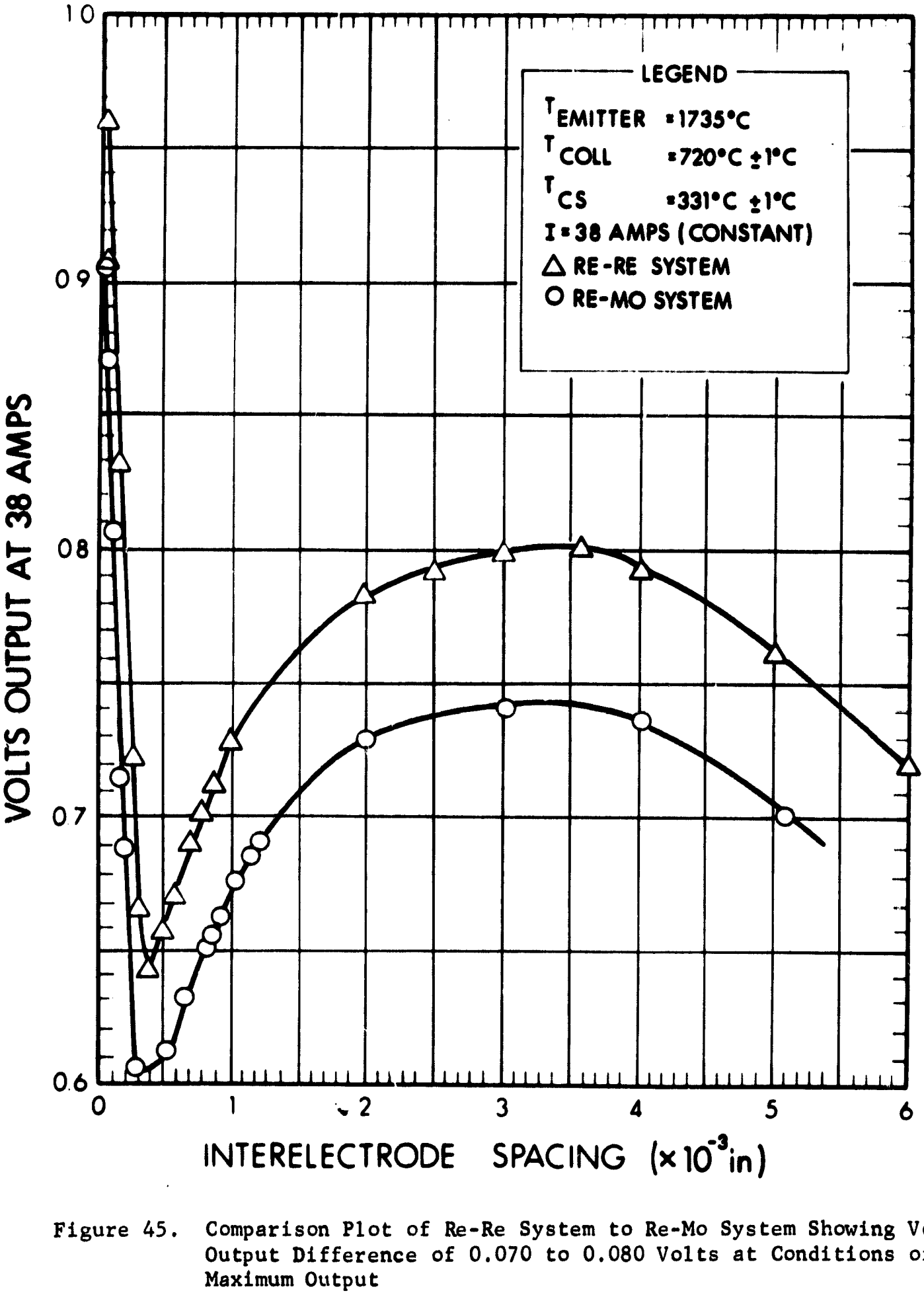

Figure 45. Comparison Plot of Re-Re System to Re-Mo System Showing Voltage Output Difference of 0.070 to 0.080 Volts at Conditions of Maximum Output

difference is somewhat less, possibly because the collector temperature is difficult to control in this region which in turn can account for 0.1 to 0.2 mil changes in the spacing. At the very close spacings of less than 0.0005 inch the collector temperature is easily controlled and the voltage difference is again near 70 to 80 millivolts.

The explanation for this behavior of collector temperature in the various regions of interelectrode spacing is as follows: Since the electron current flow and electrode surface temperatures are maintained constant while taking data from the vehicle, the only varying heat transfer quantity to the collector is gas atom conduction. At very close spacings (0.1 to 0.5 mil) the heat transfer by cesium atom gas conduction is independent of spacing and follows the classical laws developed by Knudsen (Ref. 16); at spacings from 0.5 to 2.0 mils, heat transfer measurements suggest that cesium atom gas conduction is spacing dependent; and finally, at larger spacings of 2.0 - 5.0 mils the heat transfer by gas atom conduction is essentially constant.

For ΔE = 80 millivolts (the maximum difference between a cesiated rhenium collector surface and a cesiated molybdenum collector surface), the increase in power output at 0.8V dc is 0.080/0.80 = 10 percent, the increase at 0.75V dc is 0.080/0.70 = 12 percent, both of which agree with the aforementioned measurements. For low temperature thermionics, where the converter voltage output may be in the 0.4V to 0.5V range, it is readily seen that the advantage of a rhenium collector surface over a molybdenum collector surface is 15 percent more output at 0.5 volt and 20 percent more output at 0.4 volt.

As an interesting assessment of different research approaches to thermionic energy conversion, the optimized performance from a low work function collector was compared to the optimized performance from an oxygen additive system. The data for the oxygen additive system was

obtained from the final report on JPL Contract 951262 and is shown in Fig. 46 along with cesium-only data taken from the EOS variable parameter test vehicle. The emitter temperature, in both cases, is the emitter surface temperature; the voltage output, in both cases, is the terminal voltage; and finally, the spacing, in both cases, is 5 mils. In each case, the collector and cesium reservoir temperatures are optimized for maximum output. The additive system employs polycrystalline tungsten-molybdenum electrodes while the cesium-only system employs polycrystalline rhenium-rhenium electrodes, and herein lies the important difference between the two. The rhenium collector provides the lower collector work function and consequently higher performance output. In fact, 80 millivolts more voltage output was observed from the rhenium collector at each current level from 20 to 70 amperes than was reported on the additive system.

Other comparisons at different emitter and reservoir temperatures established the same difference between the two approaches. It appears that greater performance is available from the simpler polycrystalline rhenium collector system than from any other known thermionic converter collector except perhaps an oriented or single crystal collector. The equations for increased output which were discussed previously are still applicable here; for example, the expected increase in output at 0.4 volt is 0.080/0.40 or 20 percent. From Fig. 46, the additive data yield 41 amps at 0.4V or 8.2 watts/cm^2. The EOS cesium-only converter yields 41 amps at 0.48V or 9.8 watts/cm^2, a 20 percent increase over 8.2 watts/cm^2. If, instead of holding the current level constant, the voltage level is held constant, then the increase of the nonadditive rhenium system over the additive system is 35 percent, i.e., at 0.4 volts output the Re-Re, Cs-only system yields 11 W/cm^2, while the W-Mo additive system yields only 8.2 W/cm^2.

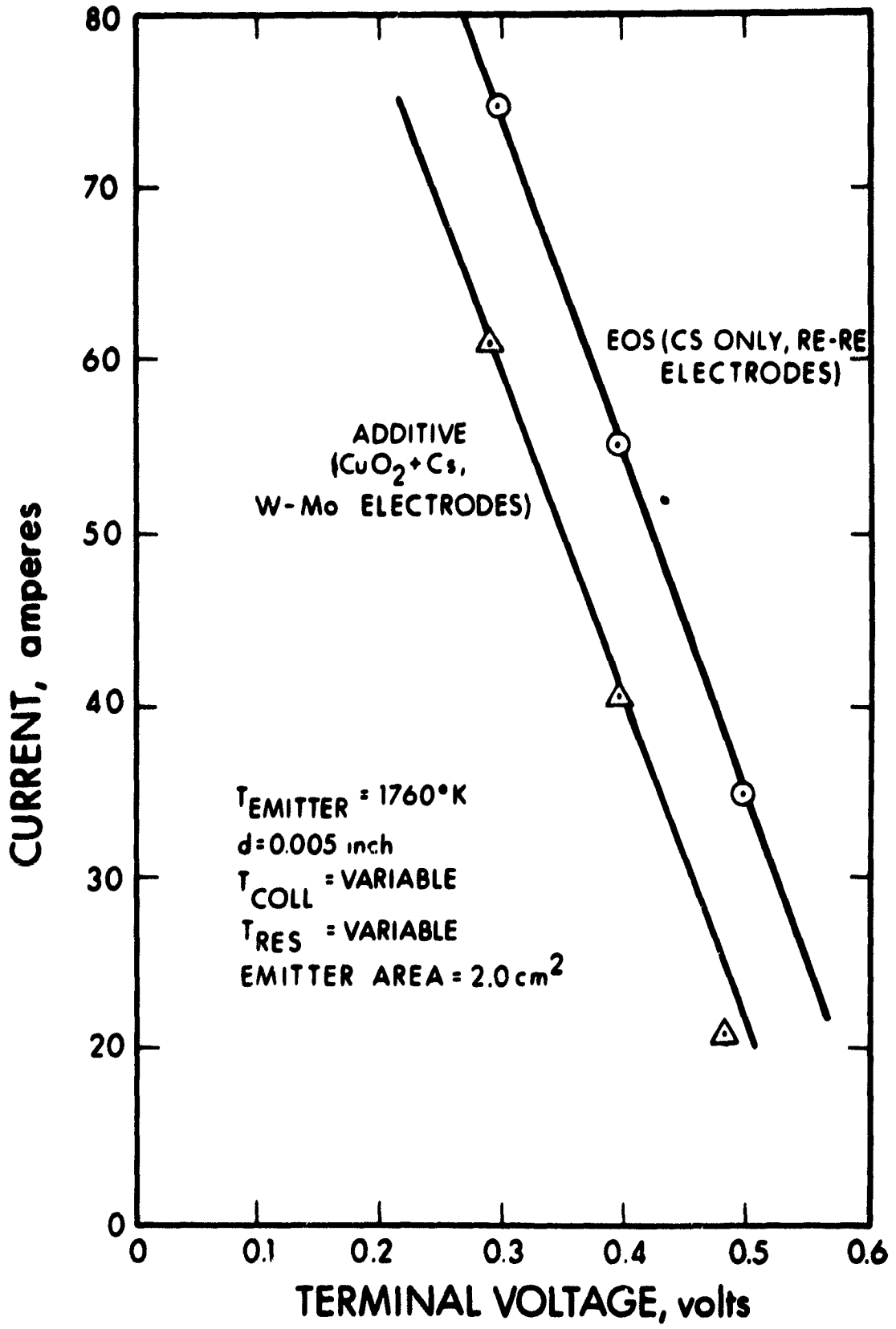

Figure 46. Optimized Performance Plot Comparing Additive Data to EOS Cesium Only Data

624168

3.1.3 PERFORMANCE FROM RHENIUM VAPOR DEPOSITED ELECTRODES

Performance data was obtained from a variable parameter test vehicle (VPTV) with vapor-deposited rhenium electrodes. Vapor-deposited sample 5 was employed as the emitter and vapor-deposited sample 3 was employed as the collector. The first task consisted of optimizing the dc current output of the vehicle as a function of spacing, cesium reservoir temperature, and collector temperature. The emitter temperature (1735°C true hohlraum) was held constant for all optimizations. Complete optimizations of current output were performed at two different output voltages, 0.7V and 0.8V. The voltage was maintained at a constant value by an electronic load. The complete optimization at a fixed output voltage and constant emitter temperature consisted of three parts. First, the collector temperature was held constant, the spacing was fixed, and the cesium reservoir temperature was varied to achieve maximum output current. Second, the spacing was fixed again, but at a different value, while the collector temperature was held constant as before. The cesium reservoir temperature was again varied to obtain maximum current output. The second step was repeated for three or four electrode separations (usually 1 mil to 4 mils) while the cesium reservoir temperature achieved optimized current output while varying between 310°C to 350°C. Third, the collector temperature was varied, performing steps one and two for each temperature. The collector temperature was varied from approximately 710°C to 775°C. Thus, for a given emitter temperature and constant output voltage, the above procedure produced a complete set of optimization data from which the maximum output current could be obtained as a function of the variables, spacing, collector temperature, and cesium reservoir temperature.

The optimum parameters for maximum power output at 0.7V are: collector temperature (as measured by an immersion collector thermocouple) of 720°C, cesium reservoir temperature of 342°C, and interelectrode spacing between 0.002 and 0.003 inch. The 0.7V data are shown in Figs. 47, 48, and 49. The 0.8V data are shown in Figs. 50 and 51.

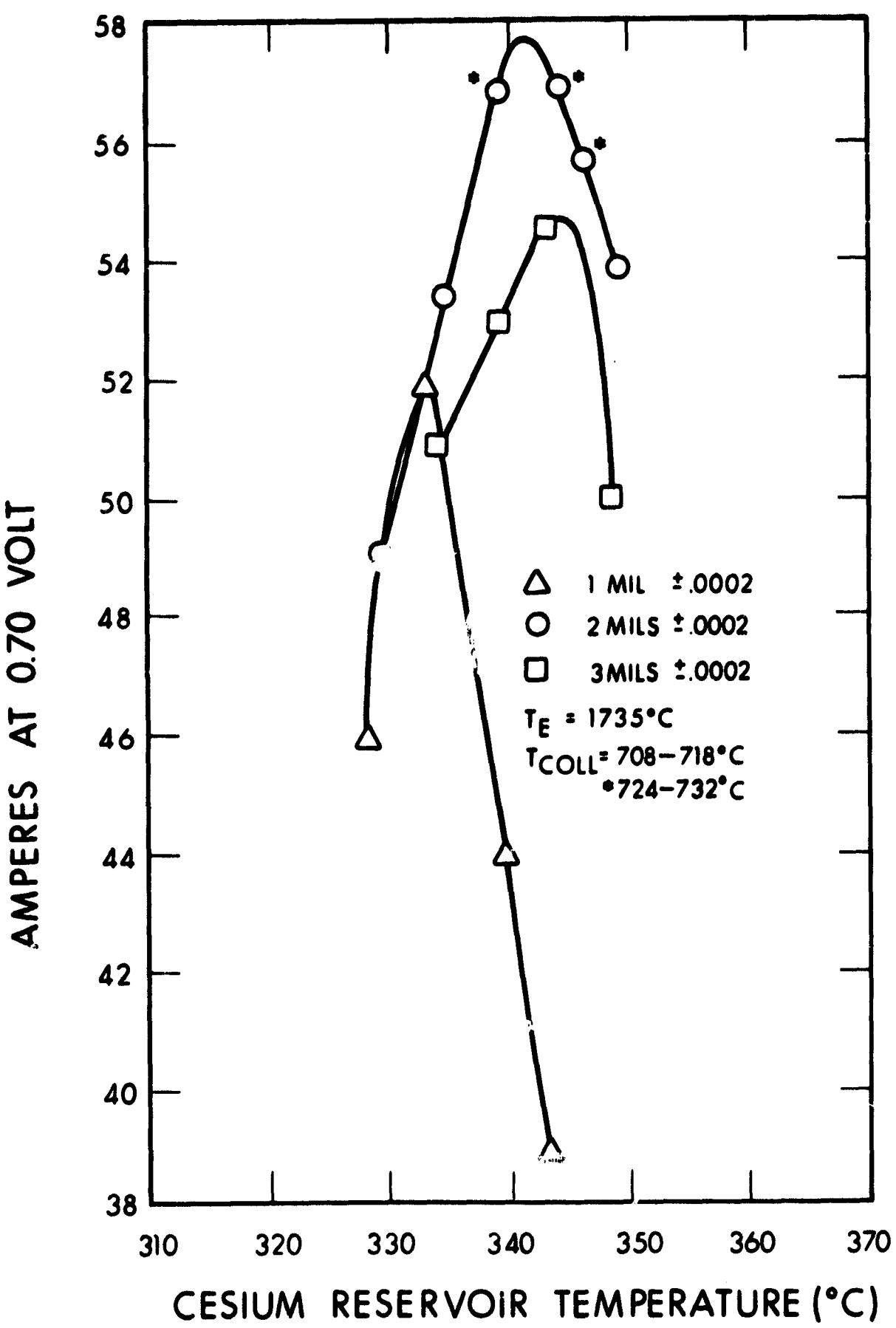

Figure 47. Converter Optimization at 0.70 Volt.
(all dc data points)

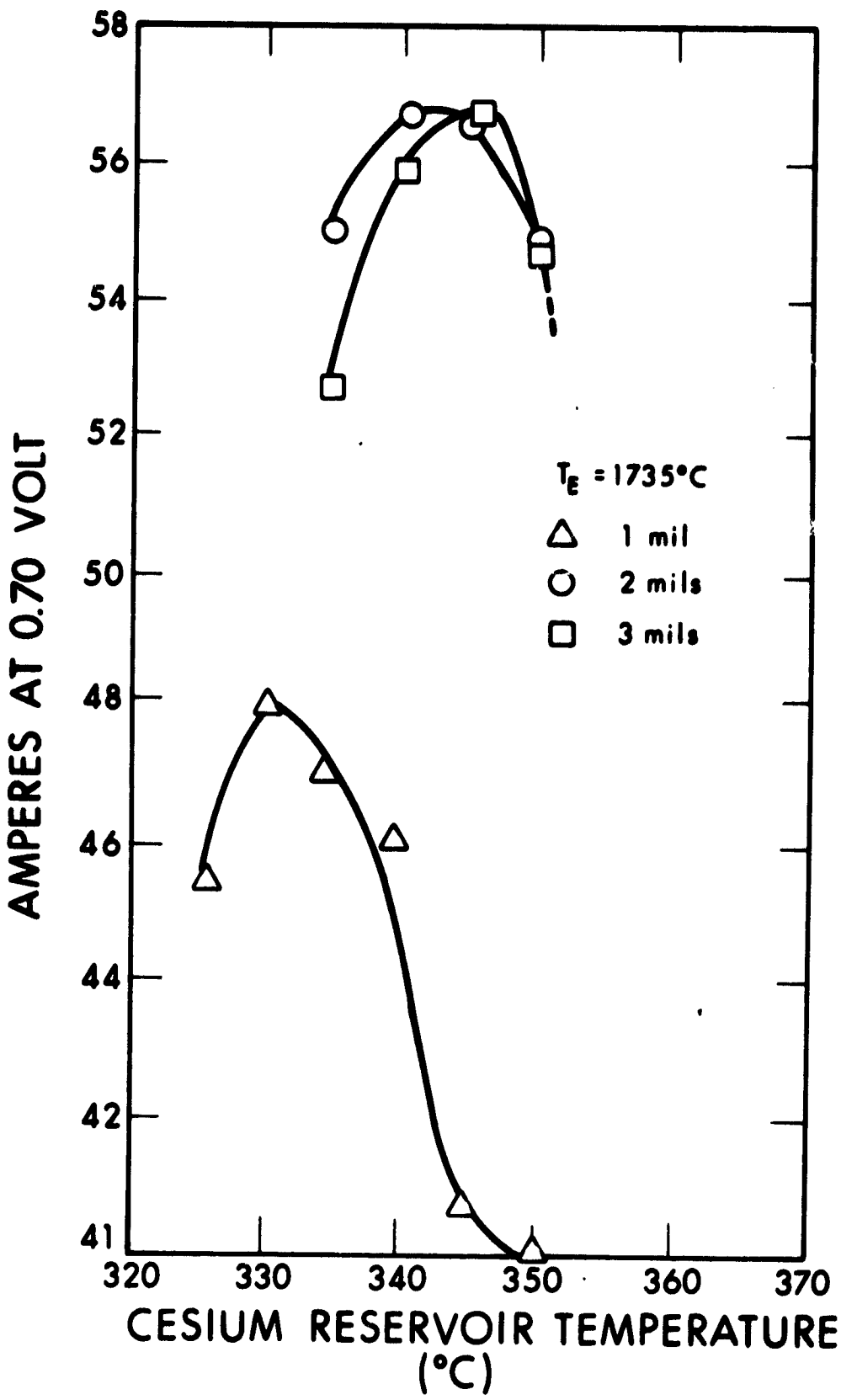

Figure 48. Converter Optimization at 0.70 Volt. Temperature of Collector 745°C to 760°C (all dc data points)

29396

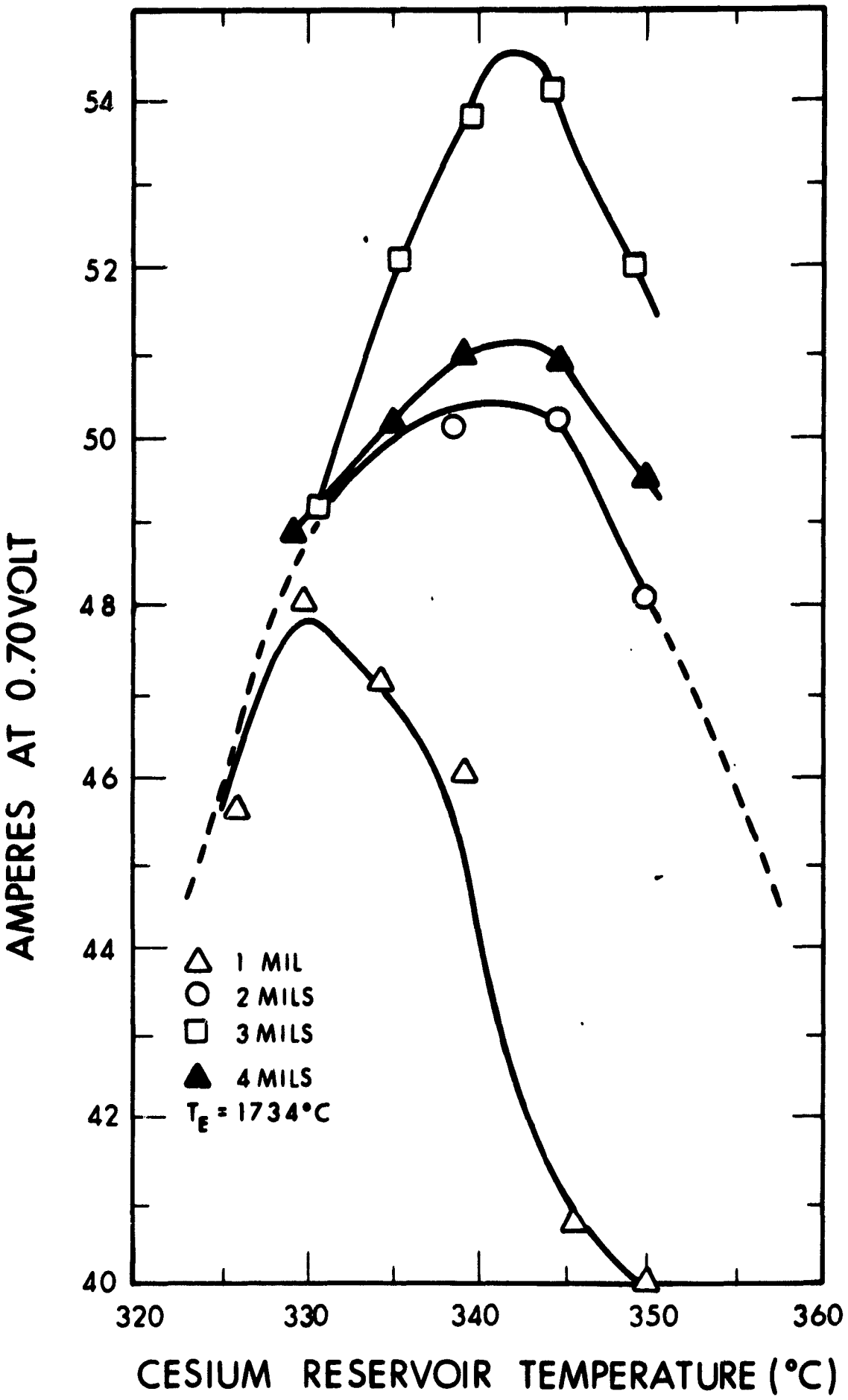

Figure 49. Converter Optimization at 0.70 Volt. Temperature of Collector 775°C (all dc data points)

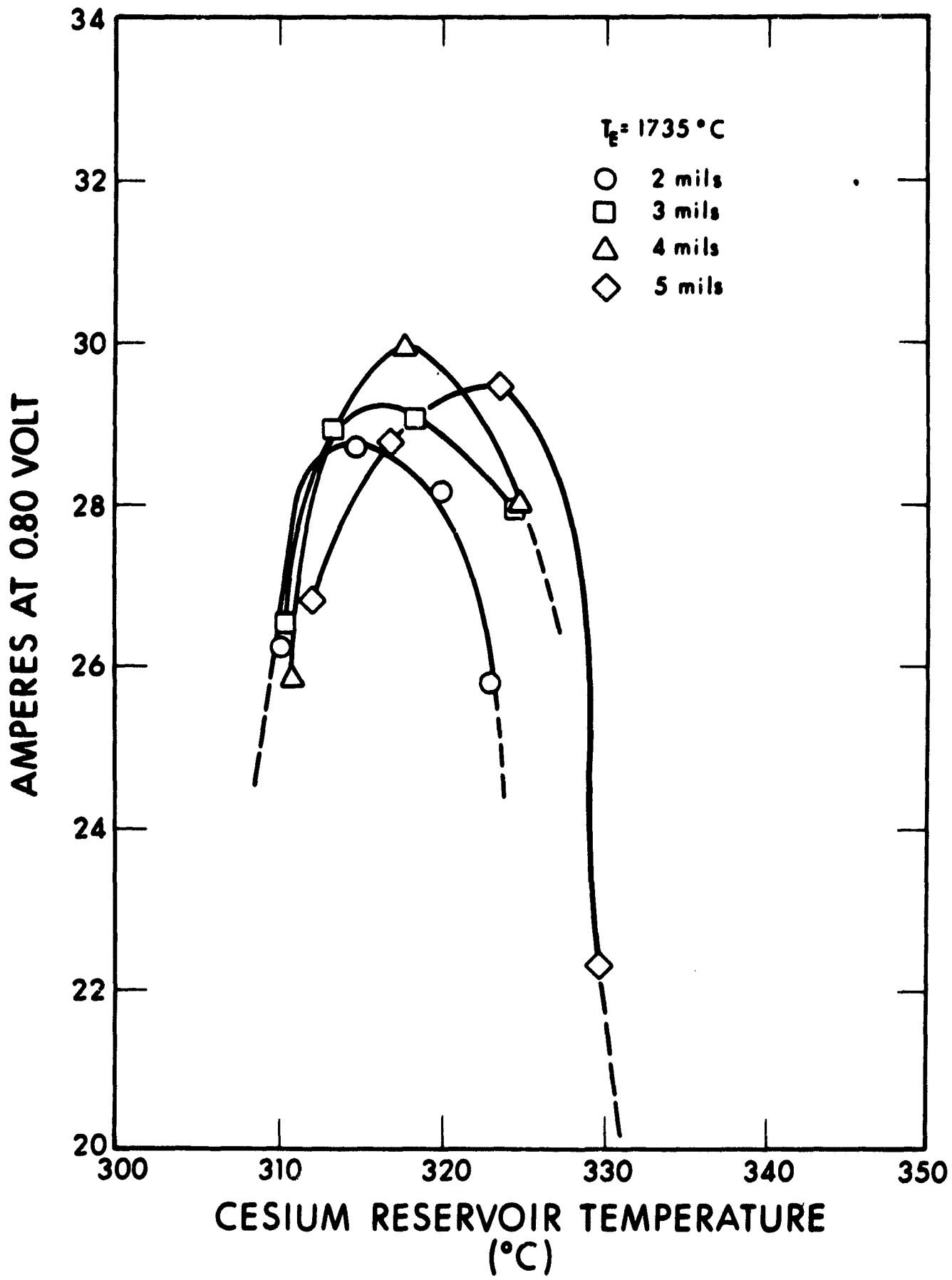

Figure 50. Converter Optimization at 0.80 Volt. Temperature of Collector 640°C to 650°C (all dc data points)

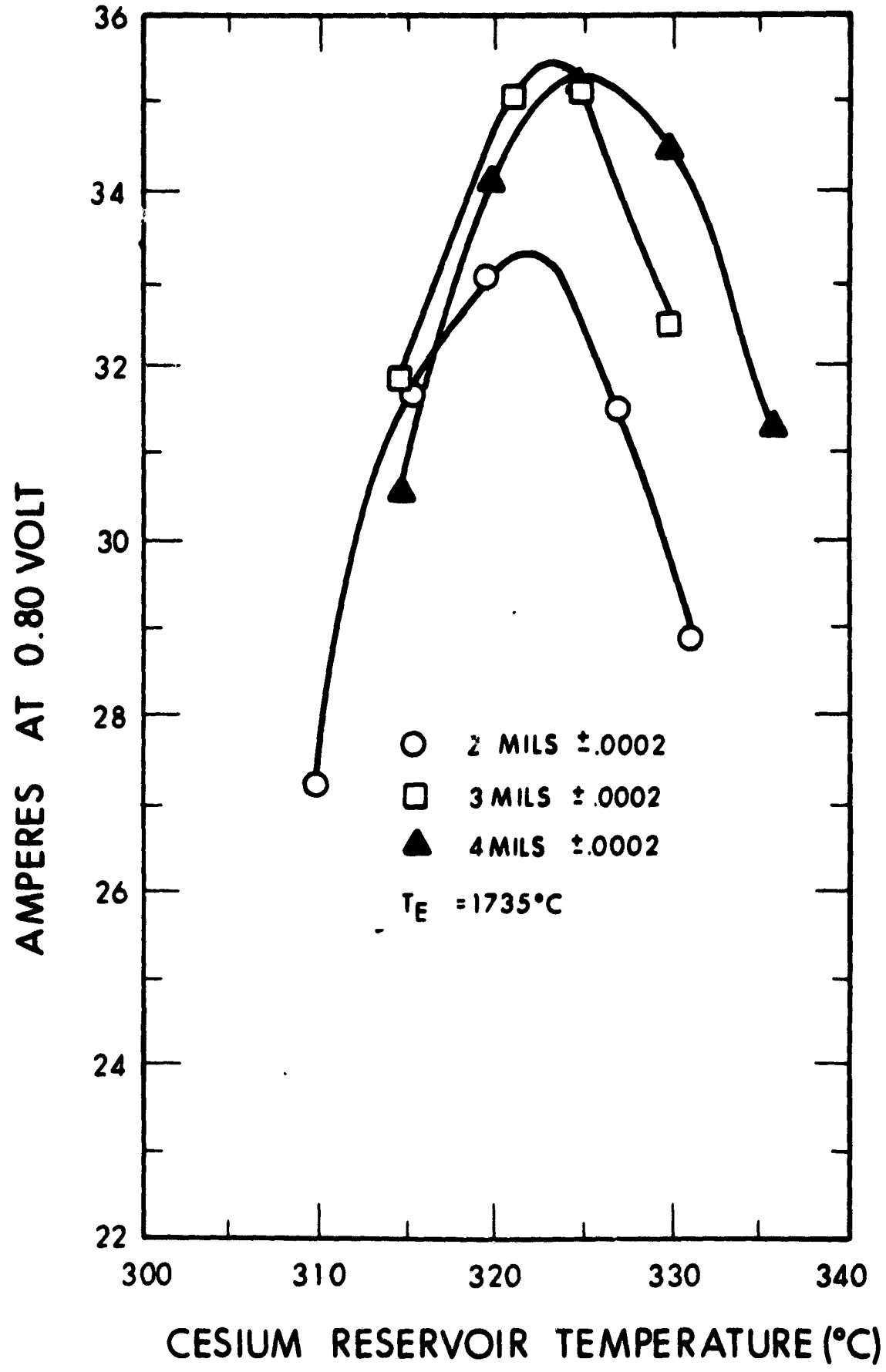

Figure 51. Converter Optimization at 0.80 Volt. Temperature of Collector 704°C to 710°C (all dc data points)

After 120 hours of operation, the VPTV performance was characterized by decreased output and non-reproducible interelectrode spacings. A comparison check on data taken at 100 hours and 120 hours of operation at 0.8V showed a decrease of 2 to 3 amperes (i.e., 6%-9%) at the same cesium reservoir, collector, and emitter temperatures. Figure 52 shows a comparison of two I-V characteristics at these conditions. The saturation emitter currents in the two I-V curves are the same ($\approx$ 25 A/cm^2) which compare favorably to that of polycrystalline rhenium.

Table XIV shows a comparison of optimized data of the vapor-deposited rhenium electrode VPTV, with that of the polycrystalline rhenium electrode VPTV.

TABLE XIV

COMPARISON OF OPTIMIZED PARAMETERS FROM VARIABLE PARAMETER TEST VEHICLE DATA FOR VAPOR-DEPOSITED RHENIUM ELECTRODES AND POLYCRYSTALLINE RHENIUM ELECTRODES; (T_E = 1735°C AND EMITTER AREA = 2.0 cm^2)

	Vapor-Deposited Rhenium		Polycrystalline Rhenium	
Voltage output (V)	0.70	0.80	0.70	0.80
Spacing (mils)	~ 2.0	3 to 4	2.6	~ 3.7
Collector temperature (°C)	720	710	746	716
Cesium reservoir temperature (°C)	342	327	341	331
Output current (amps)	58	36	60	38

An evaluation of Table XIV indicates that the performance of vapor-deposited rhenium electrodes is not significantly different from that of polycrystalline rhenium. This comparison is not absolutely conclusive because of the anomalous behavior of the vapor-deposited VPTV after about 120 hours of operation, as has already been noted.

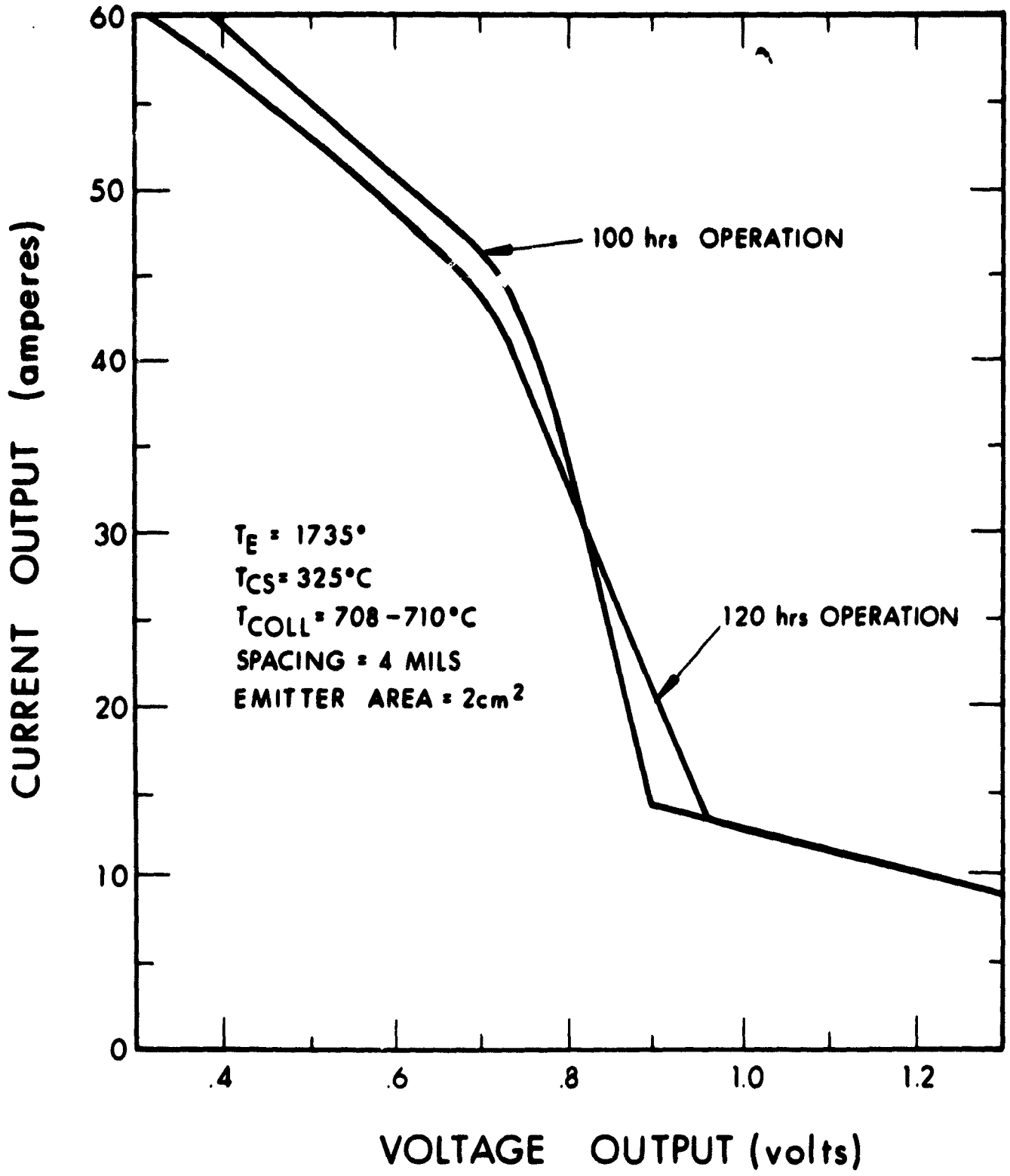

Figure 52. Vapor-Deposited Rhenium Variable Parameter Test Vehicle Characteristics Showing Shift in Performance Between 100 and 120 hours of Testing

An interelectrode spacing (d) versus voltage (V) curve was taken for the vapor-deposited rhenium system as shown in Fig. 53. The collector temperature ($\approx$ 720 $\pm$10°C), emitter temperature (1735 $\pm$5°C), cesium reservoir temperature (330 $\pm$1°C), and current (38A $\pm$1A) were the same for all three curves. A comparison of the vapor-deposited rhenium electrode system with the polycrystalline rhenium electrode system and the polycrystalline rhenium-molybdenum system show an apparent increase in the bare collector work function of approximately 0.1 eV of the vapor-deposited system over the polycrystalline system, and 0.04 eV greater than the rhenium-molybdenum system. A shift in the optimum spacing of approximately 0.0006 to 0.0007 inch indicates that the vapor-deposited emitter has a higher bare work function than does polycrystalline rhenium.

As described previously in Subsection 3.1.1, the interelectrode spacing and parallelism in the variable parameter vehicle are established by independently applying a force to three spring-loaded rods of the spacing drive mechanism. Contact between the emitter and collector is indicated by a drop in the output voltage of the device. When contact is made, the emitter temperature decreases and the collector temperature increases.

After about 150 hours of operation it was found that a clearly defined emitter-collector short circuit necessary for determination of interelectrode separation became difficult to produce. After 200 hours of operation, typical thermionic currents could not be established. A positive voltage of 3 to 4 volts was applied between the emitter and collector, and breakdown of the cesium vapor was not observed. At this time the variable parameter test vehicle was removed from the test station and a postoperational examination was undertaken.

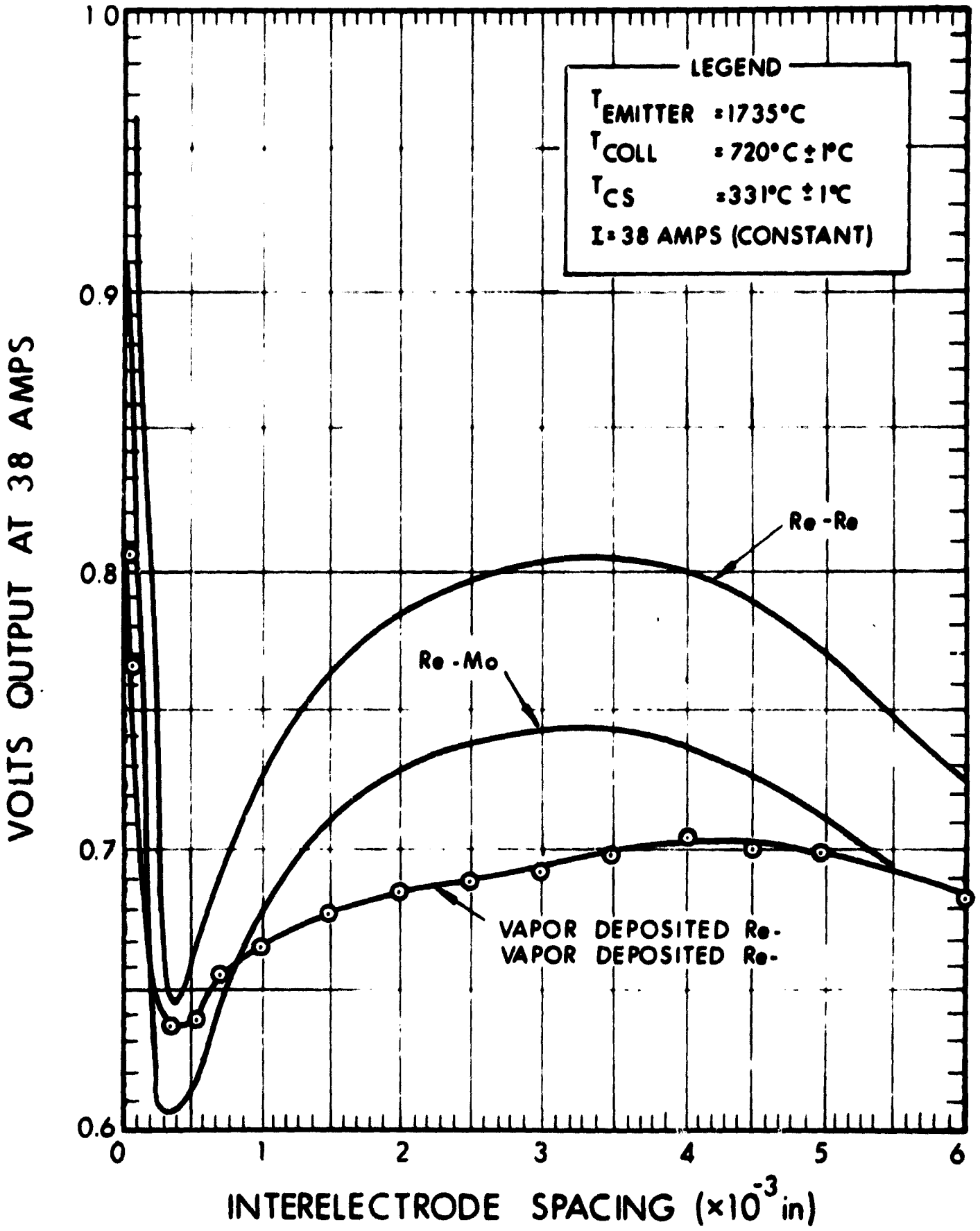

Figure 53. Comparison Plot of Re-Re, Re-Mo Systems to Vapor-Deposited Rhenium System with Altered Collector Work Function

The VPTV was opened by removing the copper reservoir tubulation to perform a vacuum leak check of the vehicle. Two large leaks were found in the titanium braze joint between the rhenium heat choke tubulation and the molybdenum emitter plate. A subsequent metallurgical cross section of this braze joint confirmed suspicions that the titanium had not adequately wetted and filled the interface between the rhenium envelope and the molybdenum emitter plate. Rhenium, having a larger coefficient of thermal expansion than molybdenum, expanded away from the molybdenum upon heating and the deficiency of titanium braze material at the interface gave rise to minute cracks in the braze material away from the interface. A reevaluation of the braze joint design has since provided a successfully tested rhenium heat choke, titanium braze, molybdenum emitter plate subsystem.

The VPTV was further disassembled by removing the emitter-heat choke plate subassembly at the seal flange to examine the vapor-deposited rhenium collector surface. Figure 54 shows the collector surface. It is apparent from an observed oxide coating on the collector that the anticipated minimum collector work function was not achieved. Closer examination revealed peaks and valleys in the oxide coating that were estimated to be approximately 0.002 inch deep. The inability to obtain an interelectrode spacing to within 0.002 inch during testing can be explained by the presence of this oxide-surfaced collector. Thick oxide flakes were also found which extended from the side of the collector barrel and connected to the guard ring. This situation could have been responsible for internal short circuiting of current at elevated temperatures.

When the emitter plate was removed, the sapphire spacing rods between the guard ring and the emitter heat choke sleeving were found to be cracked in two or three places. The purpose of these rods was to maintain a fixed spacing between the emitter envelope and guard ring before the final electron beam weld was made. It is not felt that the cracked

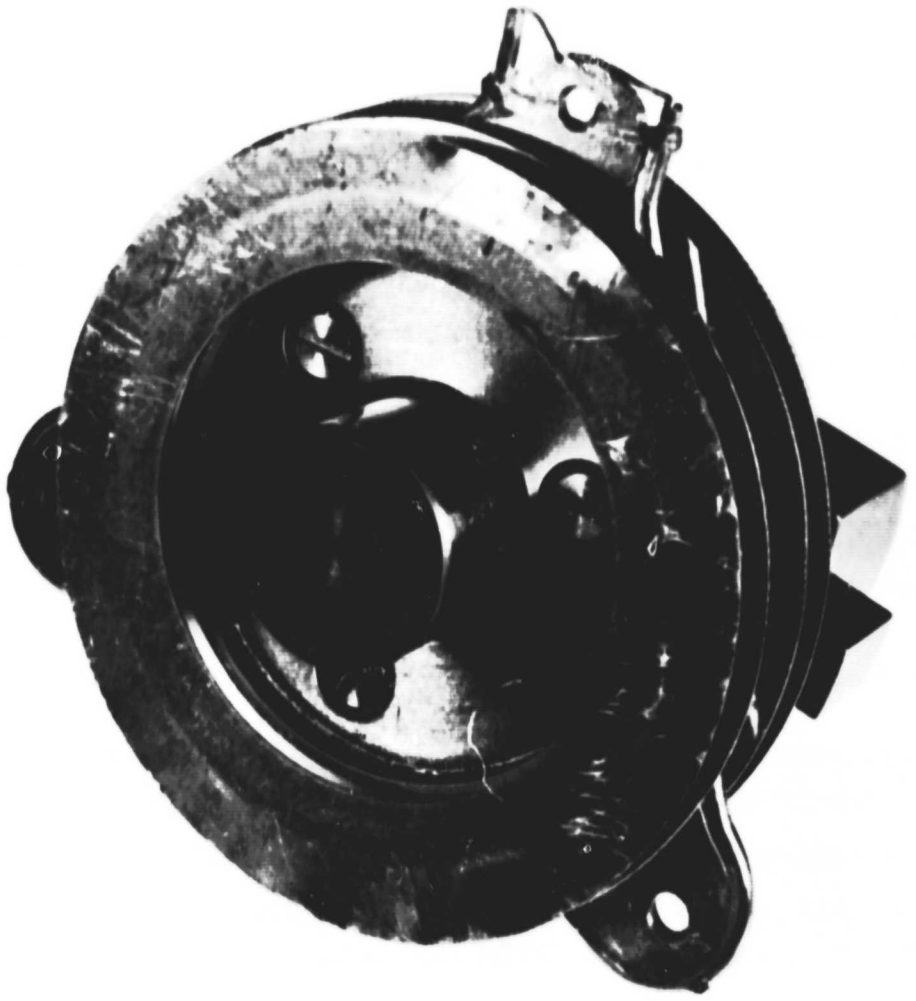

Figure 54. Collector Surface of VPTV after 200 Hours of Operation. (Note oxide coating on collector surface as a result of braze joint failure after 100-120 hours operation.)

sapphire spacing rods affected the operation of this device in any way. A reevaluation of the role of these rods has since led to their exclusion from the device since the spacing between the guard ring and emitter plate can be maintained without them during the final electron beam welding. The sapphire rods between guard ring and collector were found intact and were holding the guard ring concentric to the collector.

3.2 VAPOR-DEPOSITED RHENIUM CONVERTERS

Two thermionic converters of planar geometry employing vapor-deposited rhenium electrodes were fabricated and tested. The two converters, designated SN-109 and SN-110, are identical to the EOS SN-101 series which is described elsewhere (Ref. 17).

The sections that follow detail the converter design and fabrication and discuss the testing procedures and output performance.

3.2.1 CONVERTER DESIGN AND FABRICATION

The critical elements of converter design are an emitter structure that allows for accurate temperature measurement, a carefully defined emitter area, a reliable heat rejection system, and a method of accurately establishing the interelectrode spacing. Moreover, it is implicit to the EOS converter design that as much of the variable parameter test vehicle geometry be retained as possible. In this manner an immediate and unambiguous correlation is possible between hardware performance and research results.

The emitter structure of converters SN-109 and SN-110 permitted a direct line-of-sight pyrometric measurement of the emitter hohlraum (8:1 to 10:1) temperature which is free from extraneous radiation or reflection attributable to the filament heater. In turn, the filament heater is a counterwound, pancake filament designed for uniform heating of the

emitter backside. Thermal shielding of the filament heater prevents spurious radiation from interfering with the hohlraum temperature measurement. Figure 55 illustrates the position of the emitter, emitter hohlraum, filament heater and filament shielding. Also shown in this figure is the emitter support structure or envelope which is spaced, concentric to the collector, a distance of at least 0.012 inch. A pertinent detail in this drawing is the heat choke configuration. As noted, the heat choke section begins almost immediately below the emitter to ensure that the support structure operates at a much lower temperature than the emitter. This lower temperature and wider spacing with respect to the collector therefore allows only a minimal power output attributable to the support structure. In this manner the emitter area is defined for a planar converter, namely:

$$A_{emitter} = 1/4\ \pi D^2$$

where D is the inside diameter of the support structure.

The final elements of converter design in this discussion are reliable heat rejection, which was presented previously (Ref. 15), and interelectrode spacing which is reviewed here. The procedure for fabricating SN-109 and SN-110 was identical up to the point of electron beam welding the emitter. This was the last step and simultaneously determined the interelectrode spacing. Figure 56 is a layout of the principal subassemblies prior to electron beam welding. The emitter face contains four small flats or legs which are machined to a predetermined height. These legs are in contact with the collector at room temperature and break contact upon heating of the emitter. An interelectrode spacing is therefore achieved at the emitter design temperature for 99 percent of the emitter area. Figure 57 indicates the position of the various electron beam weldments on converter SN-109 which was spaced at 6.2 mils for an emitter temperature of 1527°C (true hohlraum). Converter

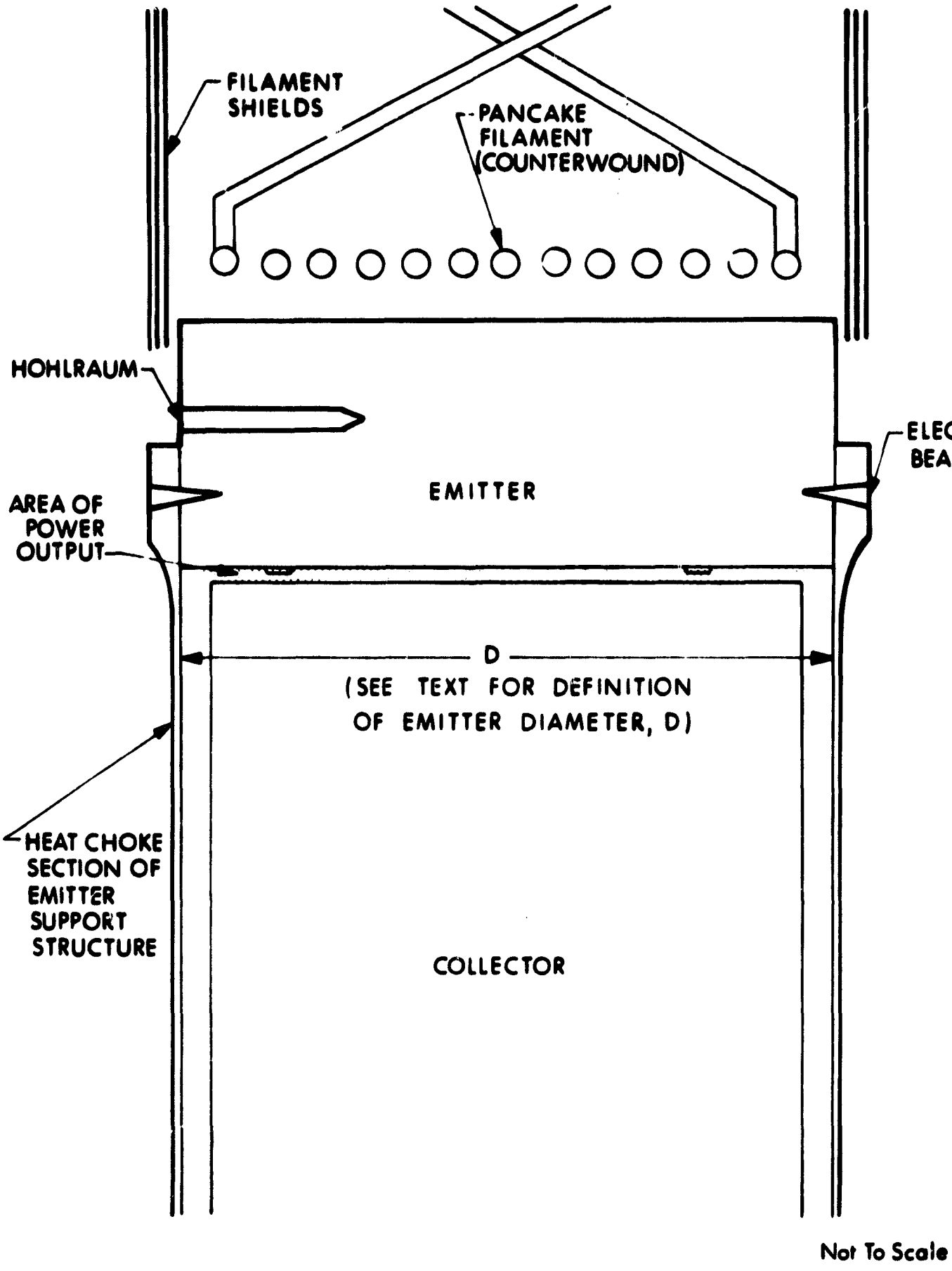

Figure 55. Basic Converter Design Illustrating the Positions of Various Parts (Note absence of power output from the emitter support structure)

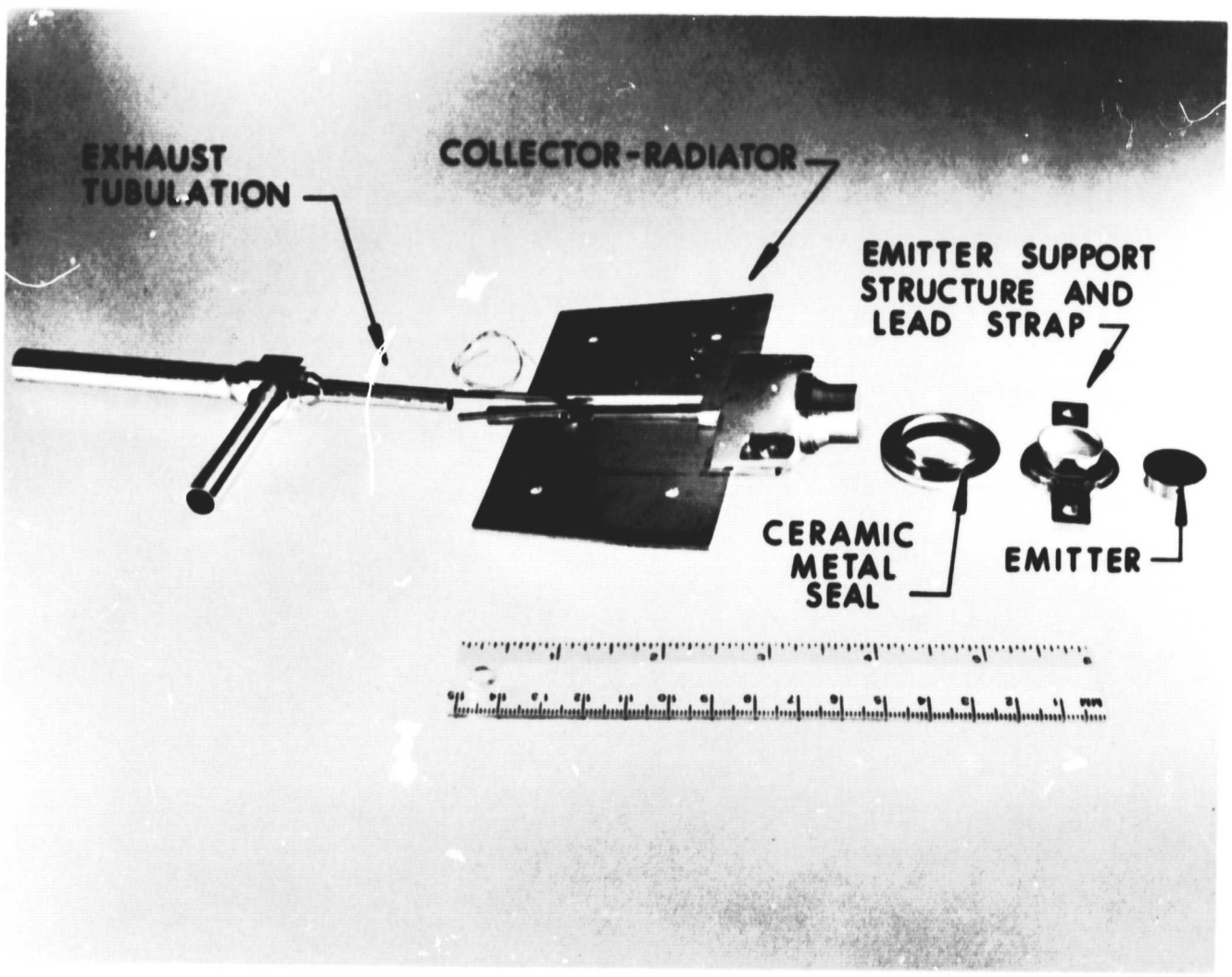

Figure 56. Layout of Principal Subassemblies of EOS SN-101 Series Thermionic Converters

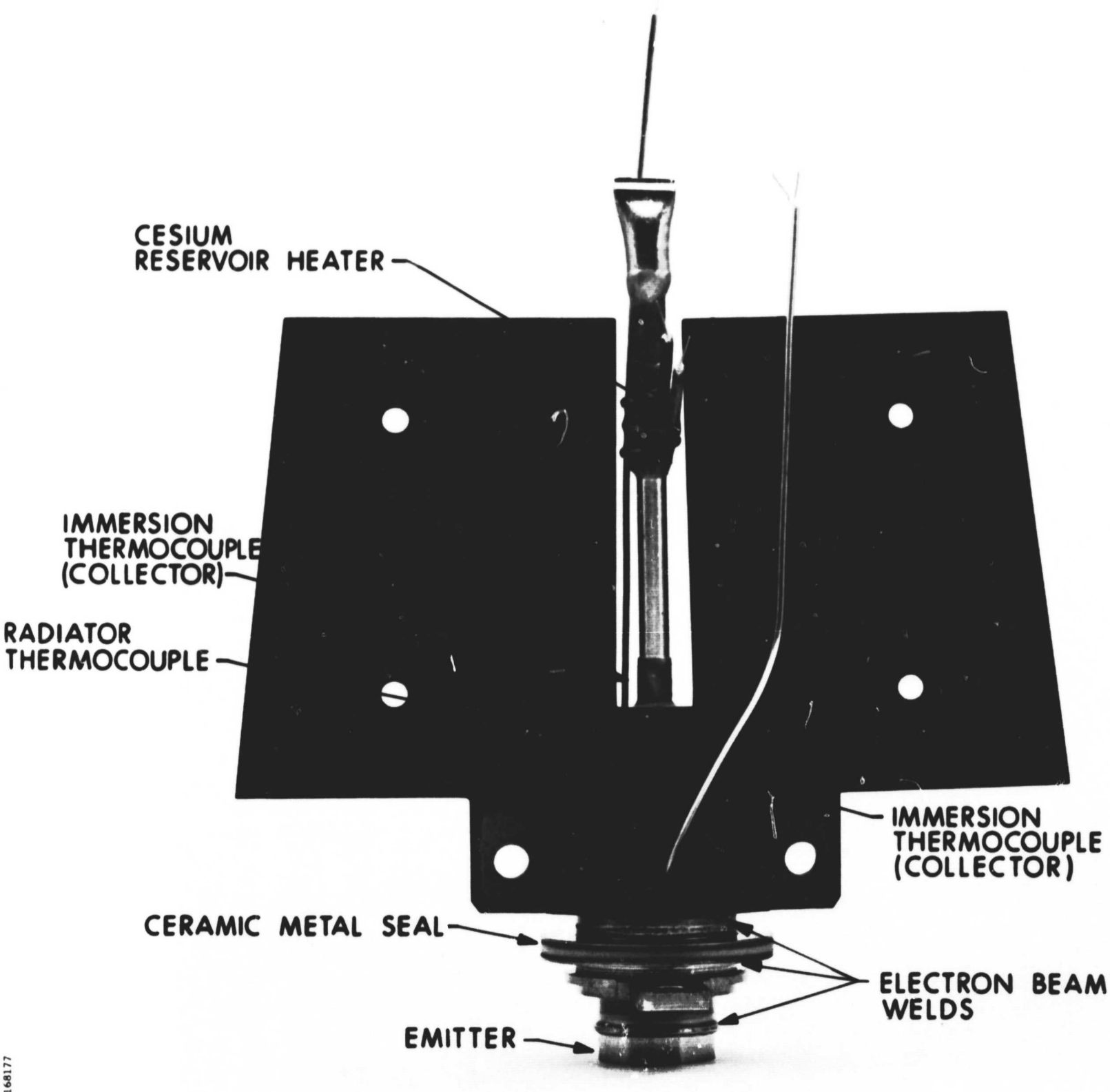

SP-168177

Figure 57. Converter SN-109 Indicating the Position of Electron Beam Welds and Thermocouples

SN-110 was spaced at 11.2 mils for an emitter temperature of 1427°C (true hohlraum). Table XV illustrates the basic design and operational similarities between the converter and variable parameter test vehicle.

3.2.2 CONVERTER TEST PROCEDURES

Converter current-voltage measurement and temperature measurement are the key experimental data obtained from converter testing.

Current-voltage data may be acquired by two different methods. The first method is the steady-state, dc measurement of optimized converter current and voltage. To facilitate testing, the usual ohmic resistor in the external circuit is replaced by an electronic load capable of maintaining either constant current or voltage output from the converter.

All voltage output is measured across the converter terminals. All current output is measured as a millivolt drop across a 0.1 percent accurate shunt. The emitter temperature is held constant while the cesium reservoir and collector temperatures are adjusted for maximum current output at a specified voltage output. To insure that the output is stable, all element temperatures are held constant for 10 to 15 minutes; the final current and voltage values are then recorded.

The second method of obtaining current-voltage data is the impression of a 60 cycle voltage source about a steady-state, dc converter operating point. This has the effect of continuously and rapidly changing the converter load line about the dc operating point. An oscilloscope of sufficient precision and stability may be employed to monitor the sweep characteristic. The main advantage of this technique is that an entire I-V characteristic may be photographed with all element temperatures unchanged. The conditions for obtaining reliable AC sweep data are as follows:

TABLE XV

COMPARISON OF CONVERTER AND VARIABLE PARAMETER
TEST VEHICLE DESIGN FEATURES

Design or Operational Particular	Converter	Variable Parameter Test Vehicle
Measurement of emitter temperature	Blackbody (8:1 to 10:1) hohlraum; directly observed in line of sight; no extraneous radiation from heater filament	Blackbody (10:1) hohlraum; directly observed in line of sight; no extraneous radiation from heater filament
Method of heating emitter	Indirect heating by counterwound, pancake electron bombardment heater	Indirect heating by counterwound, pancake electron bombardment heater
Power producing region	Sidewall emission minimized by 1) heat choke directly below emitter 2) wide spacing between envelope and collector	Collector area and emitter area equivalent by use of guard ring.
Cesium reservoir	Isolated from converter structure to establish a unique reservoir temperature	Isolated from test vehicle structure to establish a unique reservoir temperature
Materials compatibility	Solid rhenium emitter electron beam welded into rhenium tubing	Solid rhenium emitter electron beam welded into rhenium tubing
Interelectrode spacing	Fixed spacing by positive method; ±0.0003 inch accurate	Variable spacing with drive mechanism; ±0.0001 inch accurate

First, the sweep transformer should have a low inductance, low impedance secondary capable of sustaining at least 400 amperes, steady state. High leakage inductance transformers often lead to a voltage displacement or hysteresis in the I-V characteristic caused by high values of $L_{leakage}\,[dI/dt]$. Second, grounding problems should be avoided by providing a common system ground since oscilloscope grounds are made by the neutral line in the three-wire electrical system servicing the laboratory while the converter emitter is usually tied to water-pipe ground. Therefore, a voltage difference of several tenths of volts can exist between two reference points in the system. Third, the oscilloscope must have a high degree of stability, such that millivolt responses are displayed without drifting. If the oscilloscope is accurately calibrated, its display will register the true I-V characteristic for a fixed set of operating conditions. Finally, a useful technique is to double expose the film on an oscillograph – the first exposure records the dc operating level, the second records the ac sweep about the dc level and must contain the original operating point if the element temperatures have not changed.

In summary, there are advantages to both methods. The dc yields unequivocal, acceptance-type data for hardware testing. On the other hand, the ac sweep method is useful for diagnostic testing where the effects of cesium pressure and collector temperature are quickly required. Moreover, such important items as saturated electron emission, breakdown voltage, arc impedance, etc., are available from an I-V sweep picture. The important point about sweep or dynamic testing is that, <u>if done properly</u>, it gives absolute agreement with the dc method. Any point on an I-V sweep picture can be statically reproduced within test accuracy.

In addition to current-voltage measurements, temperature measurements are equally important to thermionic converter testing. There are two types of temperature measuring instruments involved with converter

testing: optical pyrometers and themocouples. The converter emitter temperature is measured by sighting a micro-optical pyrometer on an 8:1 or 10:1 depth-to-diameter hohlraum drilled parallel to the emitter surface. Micro-optical pyrometers with thin filament bulbs 1/3 to 1/6 the diameter of the hohlraum are used for converter testing at EOS, thus facilitating accurate temperature measurement. These same pyrometers are calibrated each month against a standard lamp certified by the National Bureau of Standards.

Thermocouple measurements on a converter are made at the cesium reservoir, the collector, the radiator, and the seals. All thermocouples have wire material continuity from the temperature measuring junction through the vacuum system and into the ice junction to prevent erroneous emf generation. All thermocouples are made from the same heat number as supplied by vendor source. The variation in millivolt response from these couples is approximately ±0.5 percent as determined by furnace calibration. Moreover, the couple response is ±0.5 percent of the true temperature indicated by a secondary standard of platinum/platinum-10 percent rhodium.

3.2.3 CONVERTER OUTPUT PERFORMANCE FROM SN-109 and SN-110

Since the uncertainty in performance from the vapor-deposited rhenium test vehicle did not settle the basic question of whether or not there is increased thermionic output from vapor-deposited rhenium electrodes as opposed to polycrystalline rhenium electrodes, converters SN-109 and SN-110 were first operated to compare performance with the polycrystalline rhenium system. Figures 58 and 59 are reproduced from Subsection 3.1.2 with the respective performance from SN-109 and SN-110 plotted for <u>identical</u> conditions of operation. That is, in Fig. 58 converter SN-109 was operated at an emitter temperature of 1524^{o}C, a cesium reservoir temperature of 321^{o}C, a collector surface temperature of 720^{o}C, and converter current level of 45.2 amperes. Likewise the

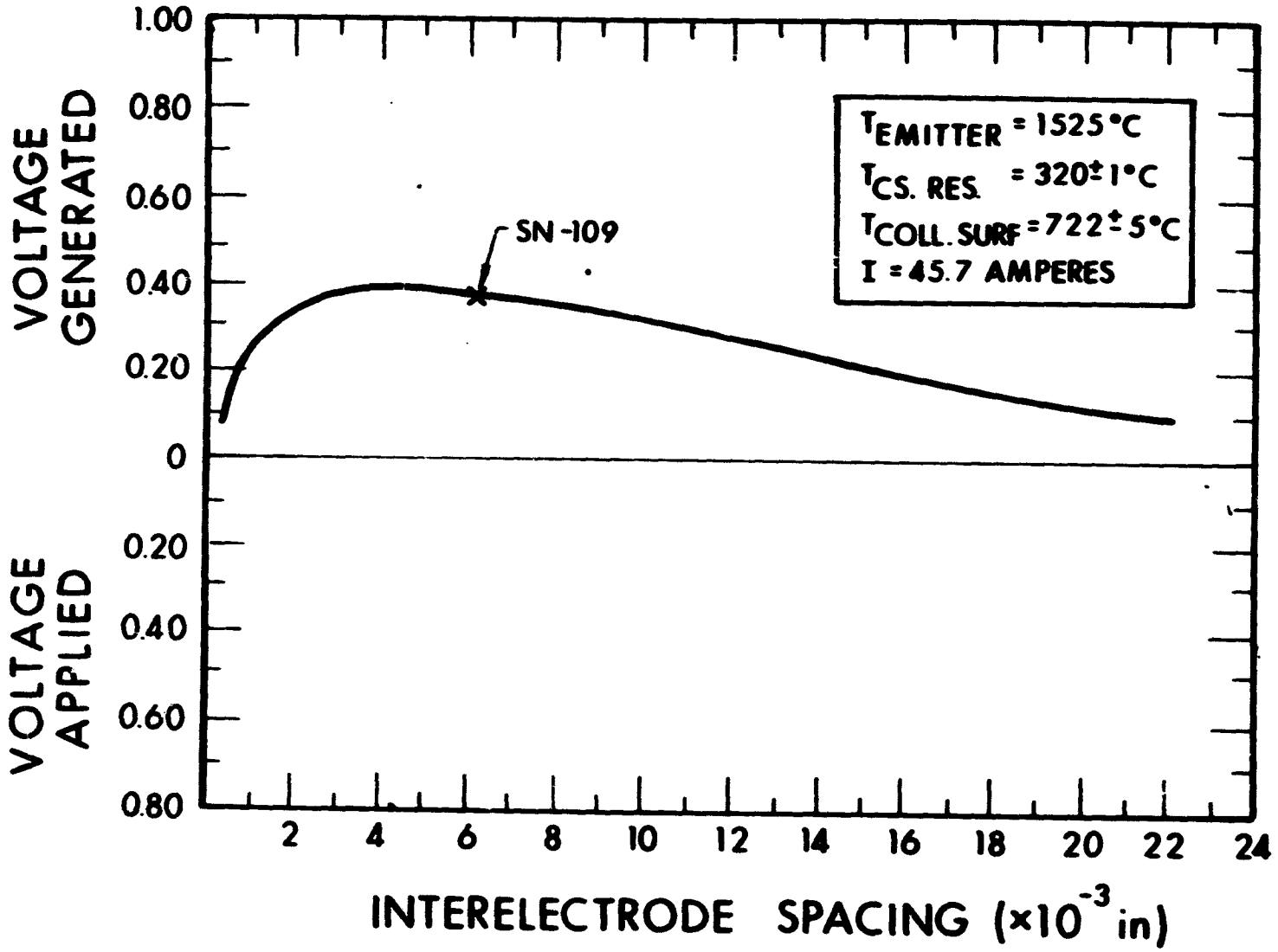

Figure 58. Comparison of Vapor Deposited Rhenium Converter SN-109 Performance with Polycrystalline Rhenium VPTV Data

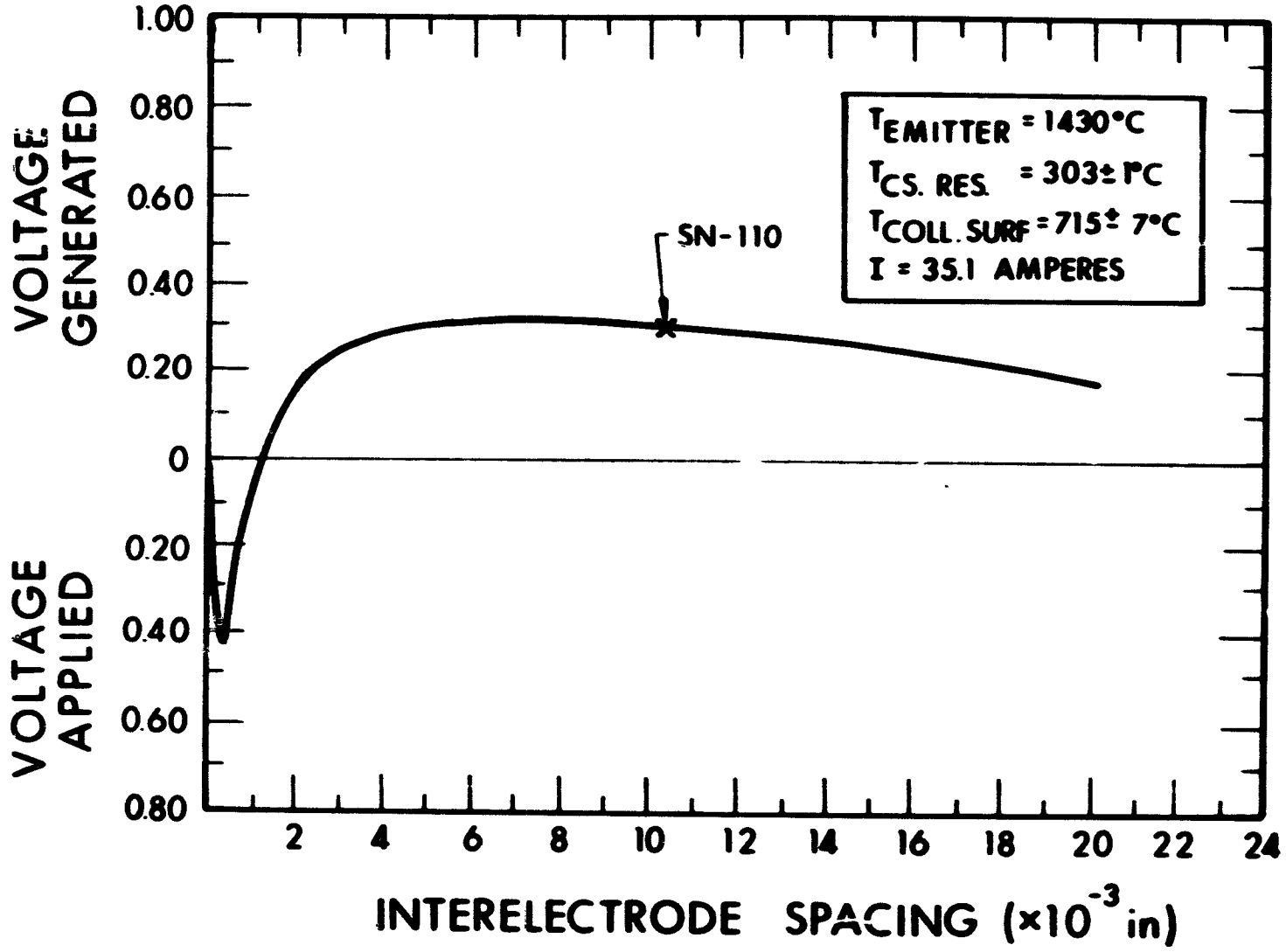

Figure 59. Comparison of Vapor Deposited Rhenium Converter SN-110 Performance with Polycrystalline Rhenium VPTV Data

operation of SN-110, as plotted in Fig. 59, was 1425°C emitter temperature (slightly lower than intended), a cesium reservoir of 302°C, a collector surface of 706°C and a converter current level of 35.1 amperes. The agreement is very close and this data suggests that the electrode systems of vapor-deposited and polycrystalline rhenium yield nearly equivalent thermionic performance.

Converters SN-109 and SN-110 were also tested at a higher emitter temperature for further comparison to polycrystalline rhenium test vehicle data performance. Figures 60 and 61 again illustrate the close agreement. It should be noted that the converter interelectrode spacing in these figures is increased by 0.0005 - 0.0007 inch over that of Figs. 58 and 59 — a result of greater thermal expansion in the emitter-support structure since it operates at a higher average temperature.

Saturated electron emission measurements were obtained from SN-109 and SN-110. While it was realized that these were not guard-ringed data, the emitter support structure design provides an effective guard against sidewall emission. Figure 62 is a plot of saturated emission from SN-109 and SN-110 as compared to the saturated emission measured for polycrystalline rhenium in a guard-ringed test vehicle. The converter values indicate reasonable agreement since the area for saturated emission is probably not known within 30 percent.

The proximity of data from the voltage output versus interelectrode spacing comparisons as well as the emission measurements suggests that the thermionic performance of vapor-deposited and polycrystalline rhenium is very nearly equivalent.

In addition to diagnostic tests, SN-109 and SN-110 were performance tested for optimum output. A voltage level of 0.4 volt (dc) and an emitter temperature of 1527°C (true hohlraum), were selected as performance test levels for SN-109. Figure 63 is a family of curves

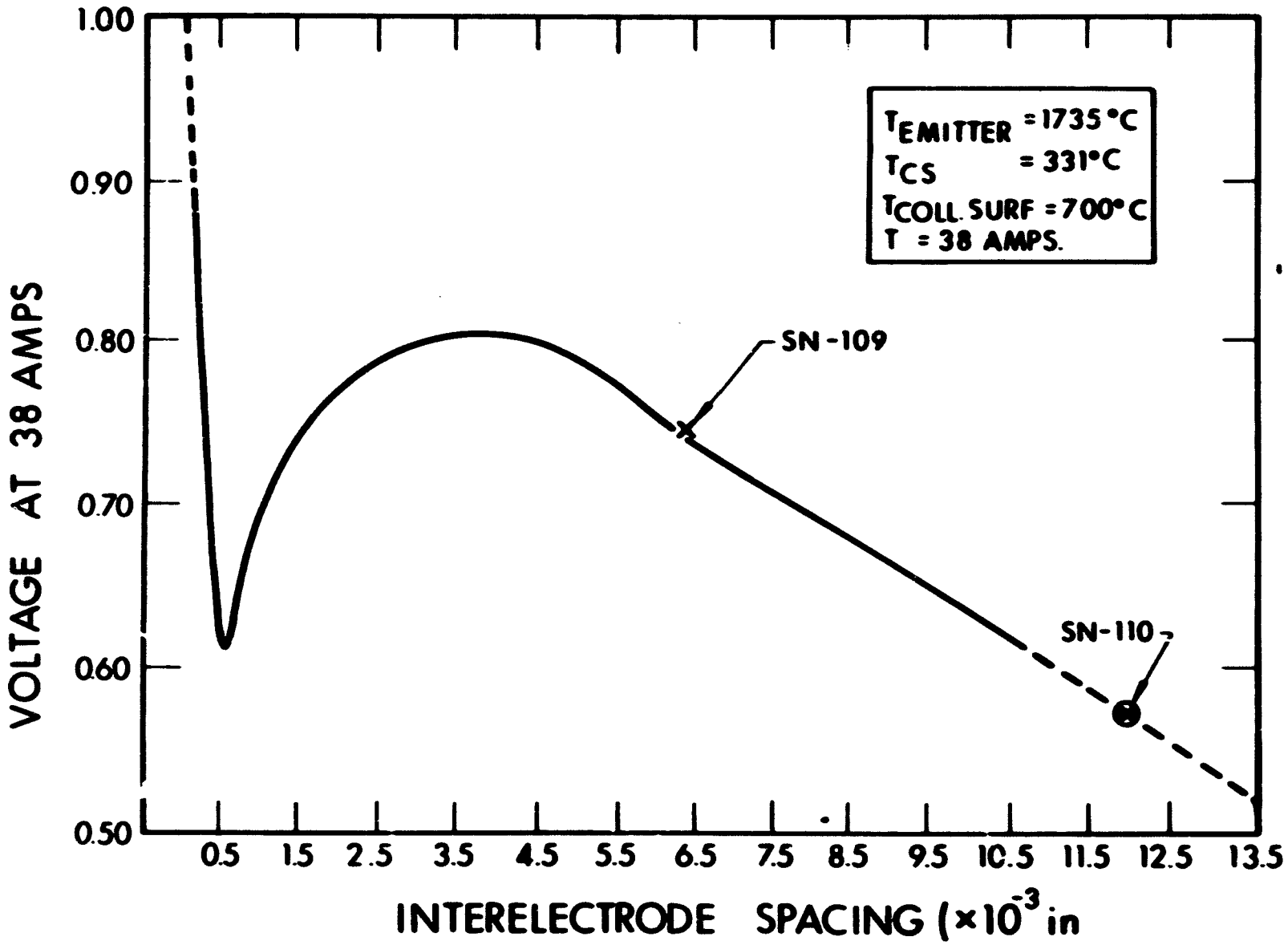

Figure 60. Comparison of Polycrystalline Rhenium VPTV Data with Vapor Deposited Rhenium Converters SN-109 and SN-110

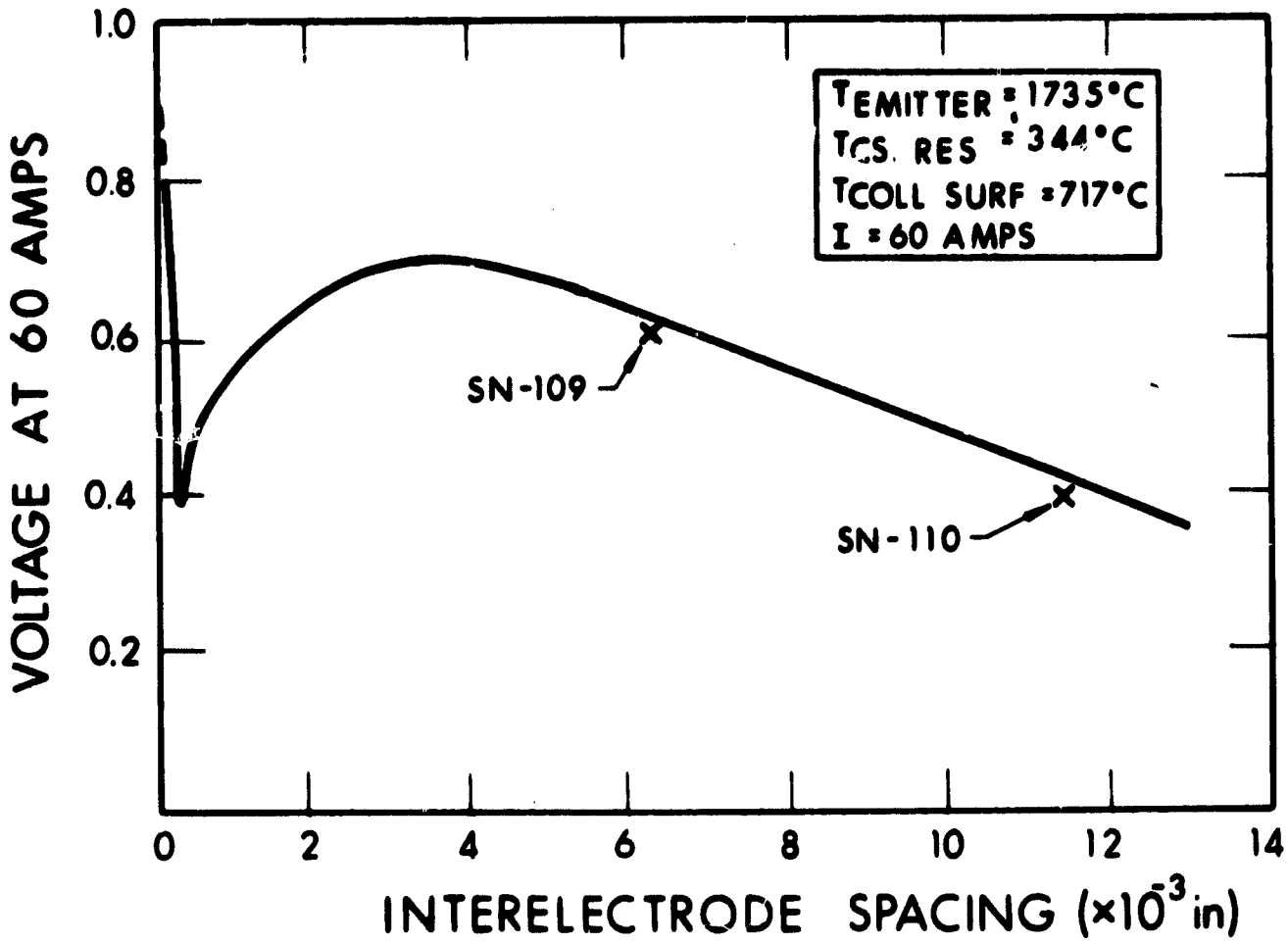

Figure 61. Comparison of Polycrystalline Rhenium VPTV Performance with Vapor Deposited Rhenium Converters SN-109 and SN-110

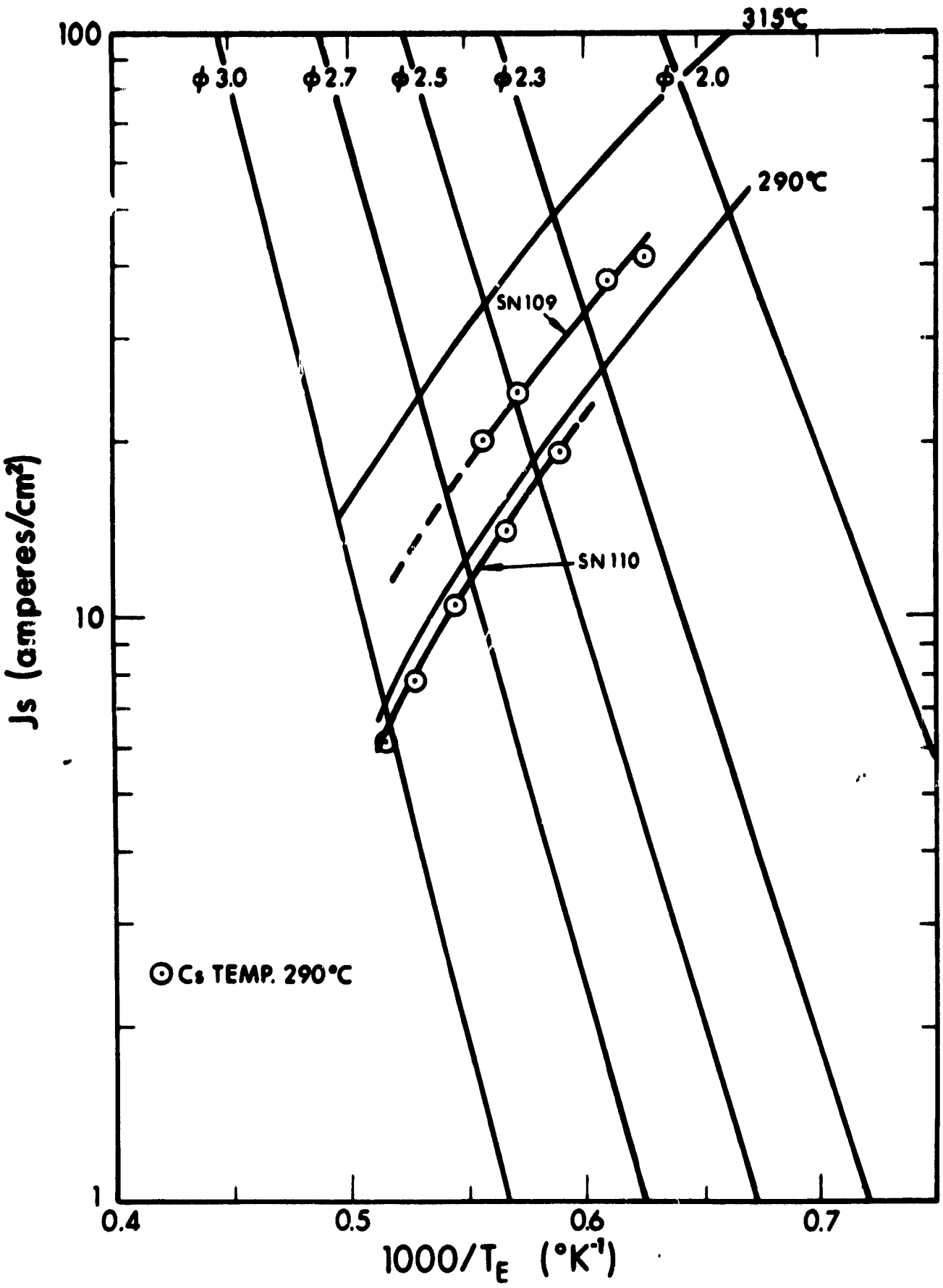

Figure 62. Comparison of Saturated Electron Emission from Polycrystalline Rhenium VPTV (measured at cesium reservoir temperatures of 290°C and 315°C) to Vapor Deposited Rhenium Converters SN-109 and SN-110 (measured at a cesium reservoir temperature of 290°C)

9955

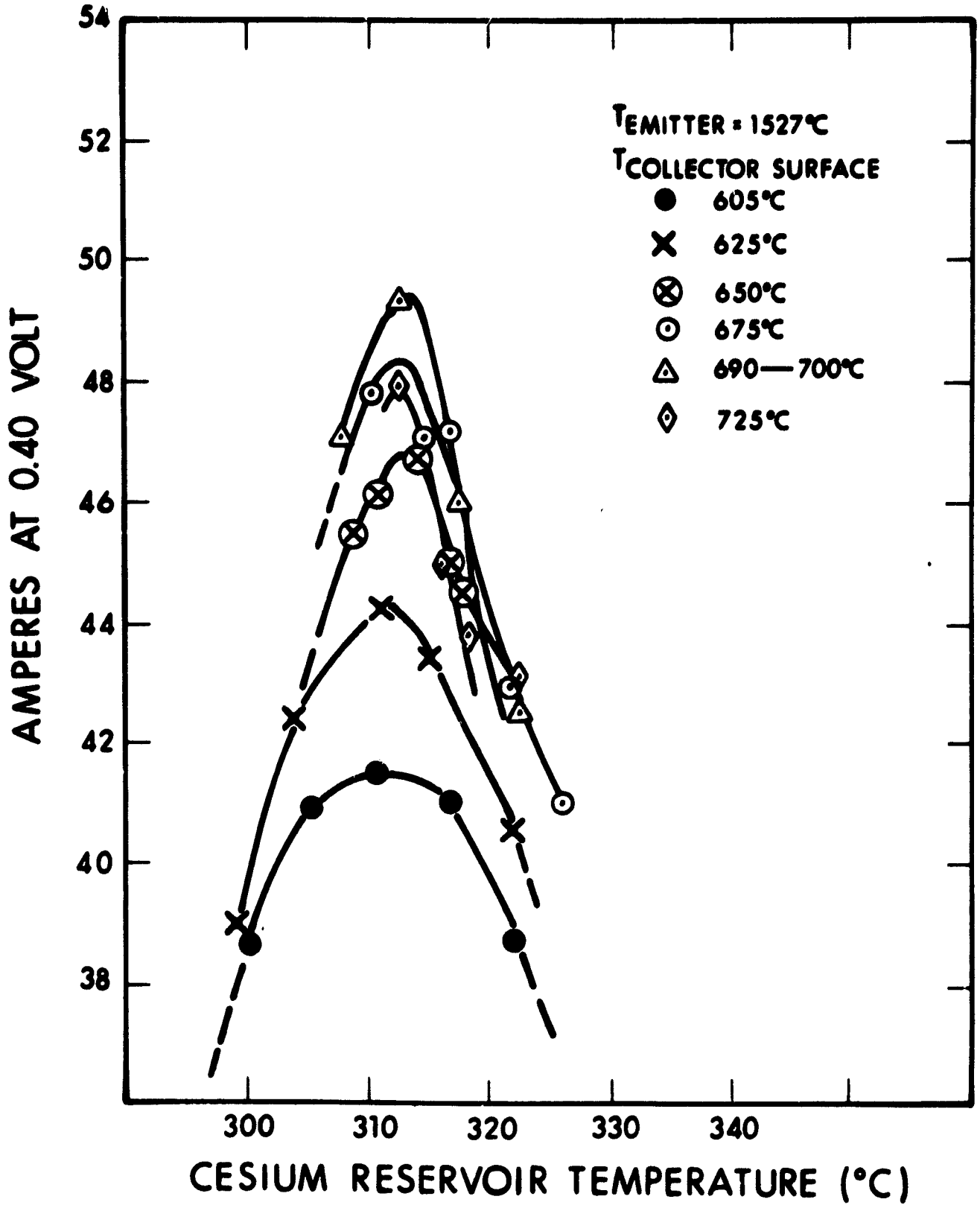

Figure 63. Converter SN-109 Performance, Optimized for a $T_{emitter}$ of 1527°C and Voltage Output of 0.40 Volt

illustrating current output (at 0.4V) as a function of cesium reservoir temperature with collector temperature as the parameter. A maximum output of 10 watts/cm^2 at 0.40V dc was recorded at a cesium reservoir temperature of 313°C and a collector surface temperature of 700°C. Converter SN-110 was tested in a similar manner at an emitter temperature of 1427°C and voltage output level of 0.30V dc with a maximum recorded output of 4.9 watts/cm^2 for conditions of cesium reservoir temperature and collector surface temperature as indicated in Fig. 64. The optimized performance from these converters is 5 percent to 10 percent less than comparable polycrystalline rhenium converters with the distinction that SN-109 and SN-110 were built to preselected interelectrode spacings which were not optimized according to the 16 mil-torr relationship. Instead, the converters were built to reproduce the voltage output versus interelectrode spacing curves at some other point than optimum. EOS's cumulative experience in matching converter to VPTV performance has been quite successful as evidenced by ten converters built and all matched to test vehicle within experimental error.

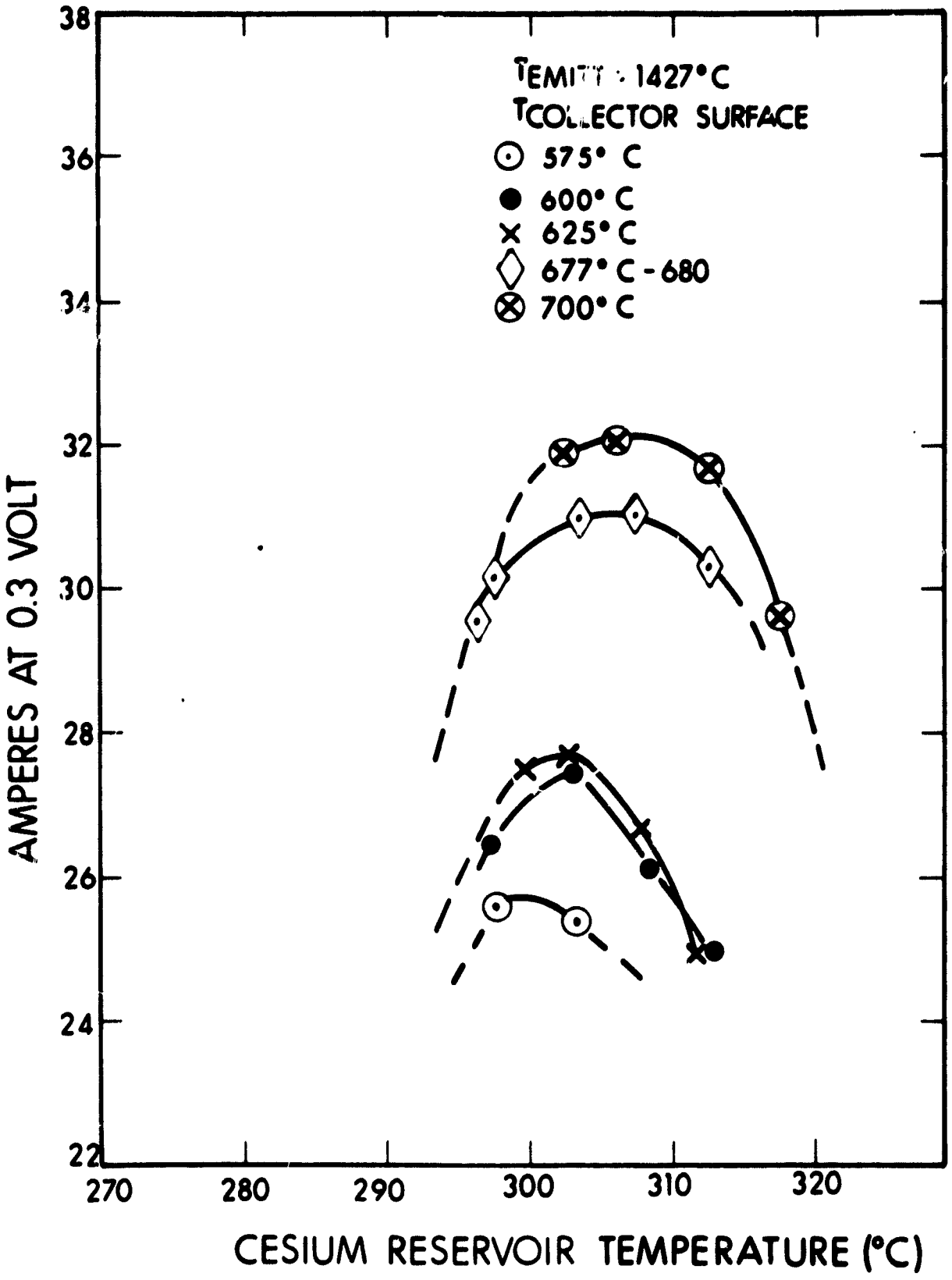

Figure 64. Converter SN-110 Performance, Optimized for a $T_{emitter}$ of 1427°C and Voltage Output of 0.3 Volt

SECTION 4

ANALYSIS AND INTERPRETATION (TASK III)

4.1 INTRODUCTION

The primary objective of Task III was to formulate a theoretical description of thermionic converter performance and apply it to an analysis and correlation of the parametric vehicle data of Task II and the data acquired in Task I. Specific topics that received particular attention in this task were: (1) the similarity laws of a cesium vapor discharge, and (2) the characteristics of the collector sheath. Task III proceeded in roughly three stages, each stage covering one of the regions of parametric vehicle operation as defined by the typical output voltage interelectrode spacing curve, V(d), shown in Fig. 65.

Region I of Fig. 65 is designated the <u>electron space charge region</u> and extends from zero interelectrode spacing to the minimum of V(d) identified as the plasma onset point. In region I, the output voltage at small interelectrode spacings is governed primarily by space charge created by electrons emitted by both emitter and collector in the absence of significant numbers of cesium ions. The theoretical model adapted for the first analysis of this region is the double vacuum diode. This model is undoubtedly valid at very small spacings, but it will have to be augmented as the spacing approaches the onset point from below by including the influences of excited cesium atoms and cesium positive ions.

At interelectrode spacings near the plasma onset point and beyond, the voltage output curve begins to display characteristics of a cesium

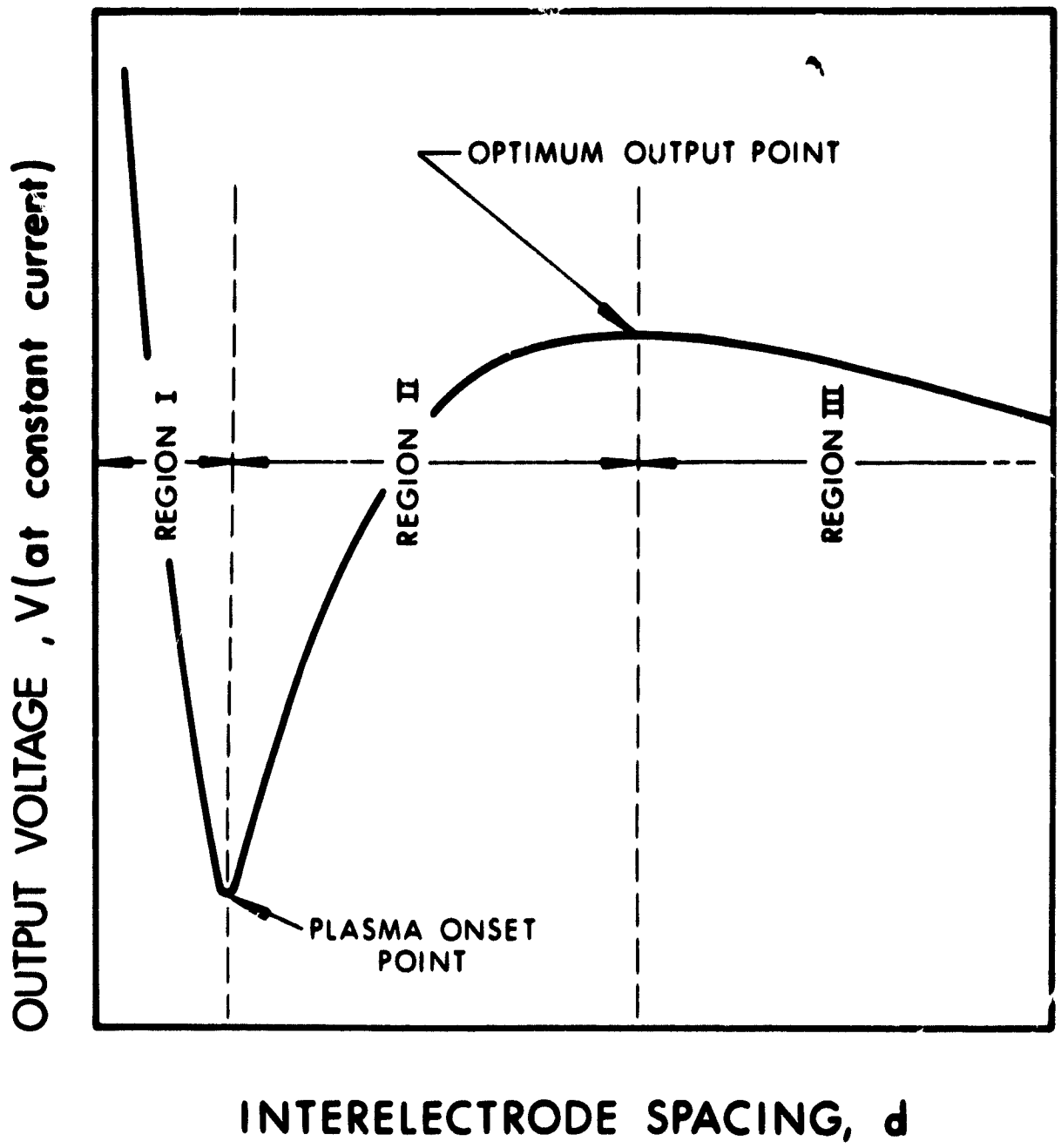

Figure 65. Typical Voltage Output versus Interelectrode Spacing Curve Showing the Three Characteristic Regions Described in the Text

plasma diode. For this reason, region II between the plasma onset point and the maximum of V(d) (identified as the optimum output point in Fig. 65) is designated the transition region. It is in this region that the plasma becomes fully developed. Region III is defined by the remaining portion of the output curve beyond the optimum power point and is designated the posi ive column region.

The Task III effort was directed mainly to the analysis of region I. The literature on both single and double vacuum planar diode space charge was reviewed, and specific application of double diode space charge theory to close-spaced cesium diodes was completed. The approach was similar to that of Dugan (Ref. 18).

4.2 THEORY OF THE VACUUM DOUBLE DICDE

The analytical problem consists of (1) deriving an expression for the electron space charge density in the interelectrode space due to electron emission from the electrodes, both of which are partially coated with cesium, and (2) combining this expression with Poisson's equation to derive the electrostatic potential energy as a function of position in the interelectrode space. The problem is treated in one dimension. The emitted electrons are assumed to be Maxwellian and the flow, collisionless. For a double vacuum diode operating in a region of applied positive voltage, the electrostatic potential will have the form shown schematically in Fig. 66. Although the space charge potential shown in Fig. 66 is typical of a diode operating with an applied voltage, the analysis of Task III included the more conventional diode operation in the power producing quadrant. In that case, the Fermi level of the collector was below the Fermi level of the emitter in Fig. 66.

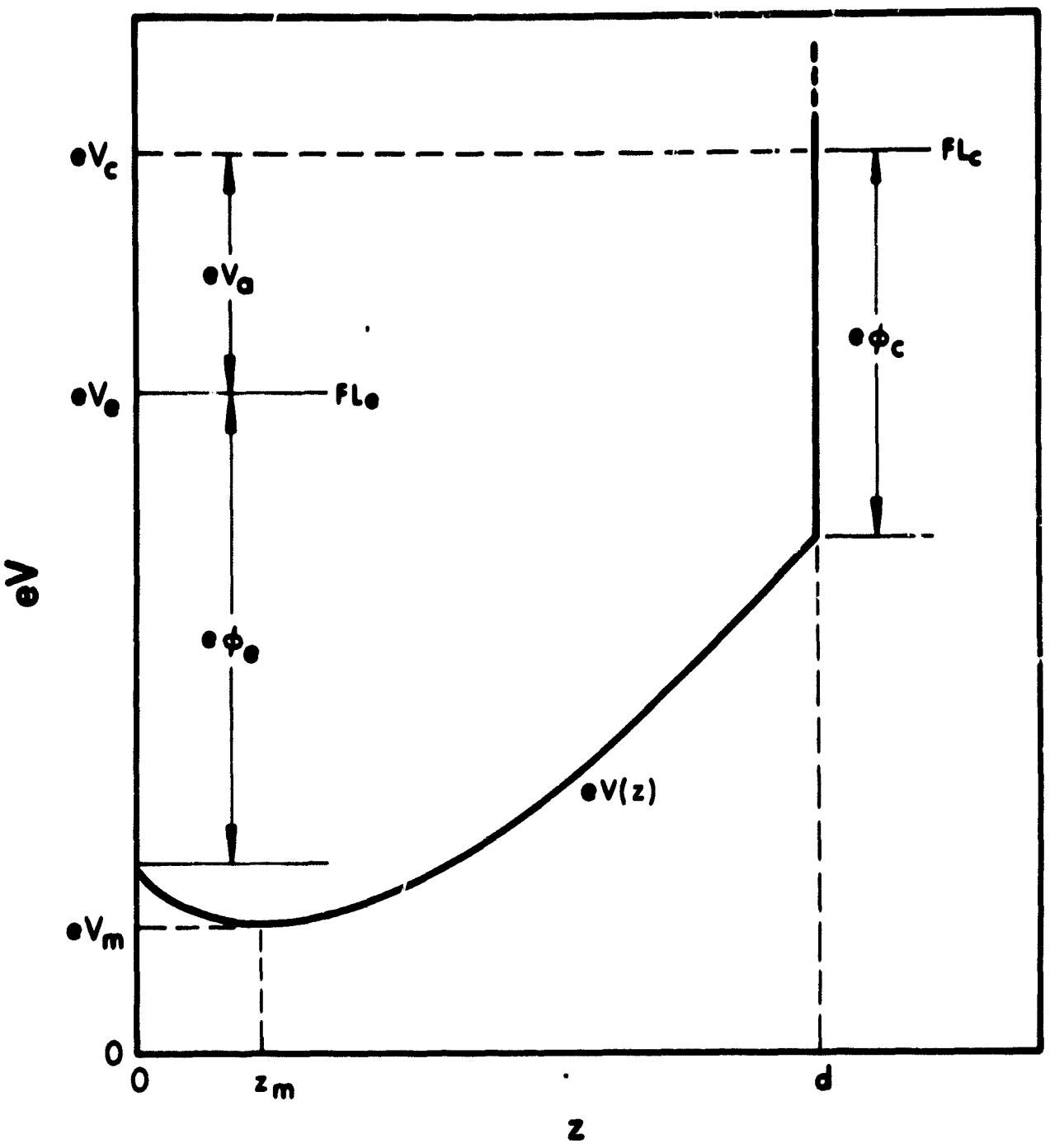

Figure 66. Schematic Representation of the Electrostatic Fotential Energy Due to Electron Space Charge Between Emitter and Collector

73624504

The symbols used in Fig. 66 and in the following discussion are listed in Table XVI.

4.2.1 ELECTRON SPACE CHARGE IN A DOUBLE DIODE

At the emitter ($z = 0$: refer to Fig. 66), the complete Maxwellian velocity distribution of the electrons is:

$$F(u,v,w) = n_{eo}(m/2\pi kT_e)^{3/2} \exp\left[-m(u^2 + v^2 + w^2)/2kT_e\right], \qquad (4)$$

where u,v, and w are the x,y, and z components, respectively, of the electron velocity; F(u,v,w) is the number of electrons in the incremental velocity range du dv dw; and n_{eo} is the <u>equilibrium</u> electron density. The density, n_{eo}, is related to the work function of the emitter and the absolute temperature by

$$n_{eo} = (2/h^3)(2\pi mkT_e)^{3/2} \exp(-e\varphi_e/kT_e). \qquad (5)$$

This density is used appropriately when no electron current is being drawn from the emitter, a case approached in principle only when $V_e - \varphi_e - V_m \to \infty$. When the potential distribution in the interelectrode space is such that all electrons emitted are drawn away from the emitter without return ($V_m = V_e - \varphi_e$) the electron density will be (1/2) n_{eo}. In this case the velocity distribution will contain all values of u and v from $-\infty$ to $+\infty$ but will contain w components from 0 to $+\infty$ only. For intermediate cases such as the one depicted in Fig. 66 where some emitted electrons are returned to the emitter because of a finite potential minimum, the density at the emitter, $n_e(0)$, is

$$n_e(0) = (n_{eo}/2)\left[1 + \mathrm{erf}\,(\eta^{1/2})\right] \qquad (6)$$

TABLE XVI

LIST OF SYMBOLS

c	=	subscript referring to collector electrode
d	=	interelectrode spacing
e	=	subscript referring to emitter electrode: -e = electron charge
h	=	Planck constant
k	=	Boltzmann constant
m	=	electron mass: subscript denoting minimum
$n_c(z)$	=	electron density due to electron flow from collector
$n_e(z)$	=	electron density due to electron flow from emitter
n_{cm}	=	electron density at potential minimum due to electron flow from collector
n_{em}	=	electron density at potential minimum due to electron flow from emitter
n_m	=	total electron density at potential minimum
n_{cd}	=	equilibrium electron density at collector surface
n_{eo}	=	equilibrium electron density at emitter surface
s	=	dummy variable in definition of error integral
u, v, w	=	x,y, and z components of velocity
x, y, z	=	rectangular coordinates
z_m	=	coordinate of potential minimum
F(u,v,w)	=	velocity distribution function
F(u,v,w,V)	=	total energy distribution function
FL	=	Fermi Level; emitter (e) and collector (c) subscript
J_c	=	electron current density flowing from collector
J_e	=	electron current density flowing from emitter
J	=	total electron current density
T_c	=	collector temperature
T_e	=	emitter temperature
V	=	potential
ϕ	=	work function
η	=	normalized potential
ξ	=	normalized coordinate

where

$$\eta = \left[(e/kT_e)(V_e - \varphi_e - V_m)\right] \tag{7}$$

and

$$\mathrm{erf}(\eta^{1/2}) = (2/\pi^{1/2}) \int_0^{\eta^{1/2}} \exp(-s^2)\, ds \tag{8}$$

is the error integral. Since erf (0) = 0, and erf (+∞) = 1, the cases of no electron flow (equilibrium) and electron flow with no return to the emitter discussed above are satisfied by Eq. 6.

Equation 6 is the expression for the density at z = 0 only. To find the density in the interelectrode space where the potential is V(z), the distribution function is written to include the variation in potential:

$$F(u,v,w,V) = F(u,v,w) \exp\left[-(e/kT_e)(V_e - \varphi_e - V)\right], \tag{9}$$

with V ≡ V(z). The electron density as a function of V(z) in the space between the emitter (z = 0) and the potential minimum (z = z_m) is obtained by integrating F(u,v,w,V) over all u and v from -∞ to +∞, and over the velocity w from $-w_1$ to ∞, where

$$\frac{mw_1^2}{2} = e(V - V_m). \tag{10}$$

The velocity w_1 is the minimum velocity in the +z direction that an electron starting at the plane at z ($0 < z < z_m$) must have to pass over the potential minimum. All electrons starting in the plane at z with velocities in the +z direction greater than w_1 pass the potential minimum and proceed into the interelectrode space between z_m and the collector.

These electrons do not return to the emitter and consequently contribute to the space charge only in the region of the emitter during their transport from the emitter to z_m. Since they do not return to the emitter, the distribution of the w component of velocities at the emitter does not contain velocities greater than $|w_1|$ directed in the -z direction.

Similarly, the density of electrons in the interelectrode space between z_m and the collector (z = d) will be found by integrating Eq. 9 over all u and v, and over w from $+w_1$ to ∞. The results are:

$$n_e(z) = (n_{eo}/2) \exp\left[-(e/kT_e)(V_e-\varphi_e-V)\right]\left\{1+\mathrm{erf}\left[(e/kT_e)^{1/2}\ (V-V_m)^{1/2}\right]\right\} \quad (11)$$

for $0 < z < z_m$, and

$$n_e(z) = (n_{eo}/2) \exp\left[-(e/kT_e)(V_e-\varphi_e-V)\right]\left\{1-\mathrm{erf}\left[(e/kT_e)^{1/2}\ (V-V_m)^{1/2}\right]\right\} \quad (12)$$

for $z_m < z < d$. Note that Eq. 11 reduces to Eq. 6 at $V = V_e - \phi_e$. At $z = z_m$, both Eq. 11 and Eq. 12 yield

$$n_e(z_m) \equiv n_{em} = (n_{eo}/2) \exp\left[-(e/kT_e)(V_e-\varphi_e-V_m)\right] . \quad (13)$$

It will be convenient to express Eqs. 11 and 12 in terms of n_{em} instead of n_{eo} and to use the notation

$$\eta_e = e(V-V_m)/kT_e . \quad (14)$$

Eqs. 11 and 12 then can be written

$$n_e(z) = n_{em}\, e^{\eta_e}\left[1 \pm \mathrm{erf}\left(\eta_e^{1/2}\right)\right] , \quad (15)$$

where the positive and negative signs are for the coordinates $z \lesseqgtr z_m$ respectively.

A similar set of expressions is derived in the same manner for the electrons emitted by the collector for the space between the collector and z_m and for the space between z_m and the emitter. These are:

$$n_c(z) = n_{cm}\, e^{\eta_c} \left[1 \mp \text{erf}\left(\eta_c^{1/2}\right)\right] \tag{16}$$

where the negative and positive signs are for $z < z_m$ and $z > z_m$, respectively. The definitions of n_{cm} and η_c are analogous to n_{em} and η_e, in Eqs. 13 and 14; that is

$$n_{cm} = (n_{cd}/2) \exp\left[-(e/kT_c)(V_c - \varphi_c - V_m)\right] \tag{17}$$

and

$$\eta_c = e(V - V_m)/kT_c \tag{18}$$

The total electron density in the plane at z in the interelectrode space is the sum of the densities given by Eqs. 15 and 16. Letting

$$\beta = n_{cm}/n_{em} \tag{19}$$

and writing

$$T_c = (1/\alpha)\, T_e \tag{20}$$

so that $\eta_c = \alpha\eta_e$, the total electron density, n(z), is

$$n(z) = n_{em}\left\{e^{\eta}\left[1 \pm \text{erf}\left(\eta^{1/2}\right)\right] + \beta e^{\alpha\eta}\left[1 \mp \text{erf}\left(\alpha^{1/2}\,\eta^{1/2}\right)\right]\right\} \tag{21}$$

The subscript e has been dropped from η since η now refers only to the emitter and is defined by Eq. 14.

4.2.2 POISSON'S EQUATION FOR THE DOUBLE DIODE

Poisson's equation,

$$d^2V/dz^2 = (e/\epsilon_o)n \tag{22}$$

where $n \equiv n(z)$, can be written in dimensionless form by using η as the dependent variable throughout and replacing the z coordinate by

$$\xi = (z-z_m)/\lambda \tag{23}$$

where λ is the Debye length for electron space charge. λ is given by

$$\lambda = (\epsilon_o kT_e/e^2 n_{em})^{1/2} \tag{24}$$

which, for n_{em} in $(\text{meters})^{-3}$ and λ in meters, is

$$\lambda = 69.0\ (T_e/n_{em})^{1/2}$$

It is frequently useful to express λ in terms of the total electron density at the space charge minimums, $\eta_m = \eta_{em} + \eta_{cm}$. Equation 24 is then

$$\lambda = [\epsilon_o kT_e(1 + \beta)/e^2 n_m]^{1/2}$$

in the notation used here.

The final dimensionless form of Poisson's equation is

$$d^2\eta/d\xi^2 = e^{\eta}\left[1 \pm \text{erf}(\eta^{1/2})\right] + \beta e^{\alpha\eta}\left[1 \mp \text{erf}(\alpha^{1/2}\eta^{1/2})\right] \tag{25}$$

where the positive and negative signs are for $\xi < 0$ and $\xi > 0$, respectively.

4.2.3 COMPUTER SOLUTIONS OF POISSON'S EQUATION

Although Poisson's equation in the form of Eq. 25 can be integrated once in closed form, the second integration must be carried out numerically. Therefore, the integration was programmed for a CDC 3100 computer. A typical family of η versus ξ computer solutions for a temperature ratio $\alpha = 2.022$ and several values of β is shown in Fig. 67. This temperature ratio (α) was selected to match experimental conditions of variable parameter vehicle experiments performed earlier.

Since there is no a priori way to establish the ratio β without knowing the potential distribution, an iterative procedure has to be used to compute a voltage output-versus-spacing curve to compare with experimental data. The procedure has been established and programmed for the computer. Basically, it involves six steps and requires numerical inputs on six parameters obtained from experiment. The experimental parameters are:

a. emitter temperature, T_e
b. collector temperature, T_c
c. emitter work function, ϕ_e
d. collector work function, ϕ_c
e. diode current density, J
f. interelectrode spacing, d

For a given $\alpha = T_e/T_c$, the steps in one iteration are:

a. Select a trial value of the ratio β, say β_1.
b. Using α, T_e, J, and β_1, compute n_{em}. This step utilizes an expression for the diode current density which is derived by summing the current densities from each electrode. The current densities are

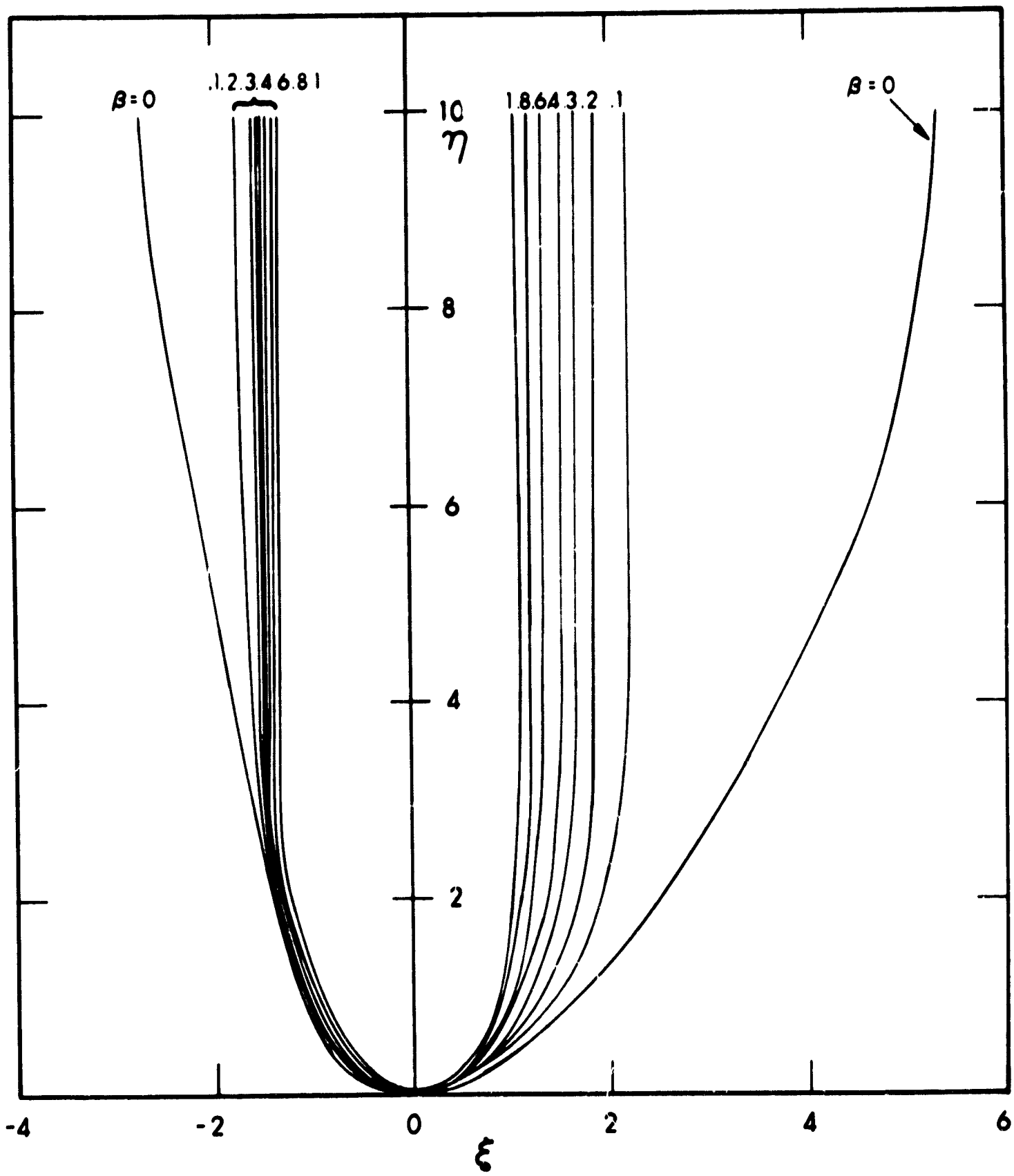

Figure 67. Normalized Potential Distribution (η) versus Normalized Coordinate (ξ) in the Interelectrode Space for the Case of α = 1.94364 and Several Values of β (α and β are defined in the text)

73627769

$$J_e = en_{em}(2kT_e/\pi m)^{1/2}$$

and

$$J_c = -en_{cm}(2kT_c/\pi m)^{1/2}$$

Using the definitions of α and β, the total current density can be written

$$J = e(2kT_e/\pi m)^{1/2} n_{em}(1 - \beta/\alpha^{1/2}) \qquad (26)$$

Thus,

$$n_{em} = J(\pi m/2e^2 kT_e)^{1/2}(1 - \beta/\alpha^{1/2})^{-1} \qquad (27)$$

c. Using a value of n_{eo} computed with Eq. 5 and the value of n_{em} computed with Eq. 27, compute the ratio $n_{eo}/2n_{em}$. This ratio is related through Eq. 13 to the difference in potential (and its equivalent dimensionless η) between the emitter surface and the potential minimum. Consequently, this computation and the curve of Fig. 67 for the trial β establishes a point on the abscissa of Fig. 67 to the left of the potential minimum. Let this point be denoted by ξ_e.

d. Calculate $n_{cd}/2n_{cm} = n_{cd}/2\beta n_{em}$ by the same procedure used in step c. The equation for n_{cd} is identical to Eq. 13 with ϕ_c and T_c substituted for ϕ_e and T_e. This step establishes a second point on the abscissa of Fig. 67 to the right of the potential minimum; call this point ξ_c.

e. Using the experimental value of d, compute d/λ using Eq. 24. Call this ratio ξ_d.

f. Compare $\xi_c - \xi_e$ with ξ_d. If $\xi_c - \xi_e > \xi_d$, the trial value of β is too small: that is, the dimensionless interelectrode spacing calculated using β_1 is smaller than the actual dimensionless spacing, d/λ. If $\xi_c - \xi_e < \xi_d$, the trial value of β is too large.

These six steps are repeated until a trial β is found which yields $\xi_c - \xi_e = \xi_d$. This establishes the proper β and the correct potential distribution for the six experimental conditions itemized above. When the proper β is found, the difference between the dimensionless potentials

at the surface of the electrodes is determined. Converting the dimensionless potentials to dimensional form yields the diode electrode surface potential difference, $V = V_a + \phi_e - \phi_c$. V_a, the applied or generated output voltage, is obtained by subtracting the contact potential difference, $\phi_e - \phi_c$, from V. The net result thus is a calculated output voltage appropriate for the given interelectrode spacing, d.

Prior to setting up the computer program for the interative procedure, each step was carried out with a desk calculator for a specific case.

Experience in use of the computer program for solutions of Poisson's equation led to improvements in the program and a better understanding of the physics involved. The improvements will be discussed as they relate to the computer program sequence.

Completed solutions provide information on the initial value to guess for β with a given set of chosen parameters. This minimizes the number of iterations necessary to find a solution. The computed electrode spacing ($\xi_c - \xi_e$) was found to vary almost linearly with log β. Therefore, the second trial value of β is found by multiplying or dividing the initial value by a chosen constant. When two iterations are complete, each succeeding trail value for β is found by extrapolation or interpolation using the previous two values of β and the resultant computed electrode spacings. The logarithmic variation of β is used in the predicting equation.

There are lower and upper limits on the electrode spacing which may be used in this analysis of a space charge limited thermionic double diode. These limits are determined by the choice of current density in the diode, the electrode surface temperatures, and work functions, which are held constant for each computation.

The lower limit on diode electrode spacing is given by two expressions for the normalized electrode potentials at the emitting and collecting electrode surfaces, respectively:

$$\eta\Big|_e = \ln\left[\frac{2^2\pi mk^2}{h^3}\,T_e^2\,J\left(1 - \frac{\beta}{\alpha^{1/2}}\right)\right] - \frac{e\phi_e}{kT_e} \tag{28}$$

and

$$\eta\Big|_c = \frac{1}{\alpha}\ln\left[\frac{2^2\pi mk^2}{h^3}\,\frac{T_c^{3/2}\,T_e^{1/2}}{}\left(\beta^{-1} - \alpha^{-1/2}\right)\right] - \frac{e\phi_c}{kT_e} \tag{29}$$

The minimum useful electrode spacing for analytical purposes occurs when the collector moves so close to the emitter that its position coincides with that of the space charge potential minimum. It may be observed from Fig. 67 that increasing β decreases the distance between given potential values. Since the normalized collector potential also decreases as β is increased, the maximum allowable value for β may be calculated by solving Eq. 29 for β and allowing the collector potential to approach zero. There is a related higher limit on β set by Eq. 28 but Eq. 29 gives the smallest value since the emitter temperature is higher than the collector temperature. If a chosen electrode spacing is too small in relationship to the other parameters, the computer program will sense the second try of the maximum β (for $\eta\Big|_c = 0$) and print a message stating that the spacing is too small, and then proceed to try the next set of data.

The upper limit of electrode spacing for a given set of chosen parameters of the space charge limited diode is determined by the available input energy. As the spacing approaches the upper limit, the required applied potential increases rapidly. From Fig. 67 it will be noted that $\beta = 0$ gives the largest spacing between given potentials. Also from Eq. 25 when β approaches zero, the relationship between potential and distance becomes independent of α. The approximate value of maximum

normalized spacing may be obtained from Fig. 68. It will be noted that the left branch becomes essentially vertical at $\xi_e = -2.9$ and the right branch becomes essentially vertical at $\xi_c = 5.5$. The normalized spacing thus given is $\xi_d = 8.4$. The physical significance of $\beta = 0$ is, of course, the single diode without electron flow from the collector as developed by Langmuir (Ref. 19). The η and ξ values from Fig. 68 are in agreement with Langmuir's original work and represent the limiting case of the double to single diode.

The Debye length for normalization of the chosen distance includes β as a variable:

$$\lambda = \left[\left(\frac{\epsilon_o k^{3}2^{1/2}}{e\, m^{1/2}}\right) \frac{T_e^{3/2}}{J} \left(1 - \frac{\beta}{\alpha^{1/2}}\right)\right]^{1/2} \qquad (30)$$

Fortunately, as β approaches zero (in the case of large electrode spacing) λ becomes independent of β. In the computer program, the normalized value of the chosen distance is compared with the fixed value 8.4. If the chosen distance is too large, a message stating that fact is printed and the next set of parameters is tried. Of course, the presence of ions in the practical diode will tend to neutralize space charge effects allowing larger spacing of the electrodes. The effect of ions could be included in future models of the computer program.

Figure 69 is a plotted comparison of the computer solution results and experimental data from the variable parameter test vehicle. There is approximate agreement between the two in the output voltage range from 0.70V to 0.90V; however, at very close spacings (~ 0.0001 inch or less) and at 0.0005 inch the agreement is poor for the following reasons: (1) It is impossible to experimentally maintain interelectrode spacings of less than 0.0001 inch, yet in theory the closer the interelectrode

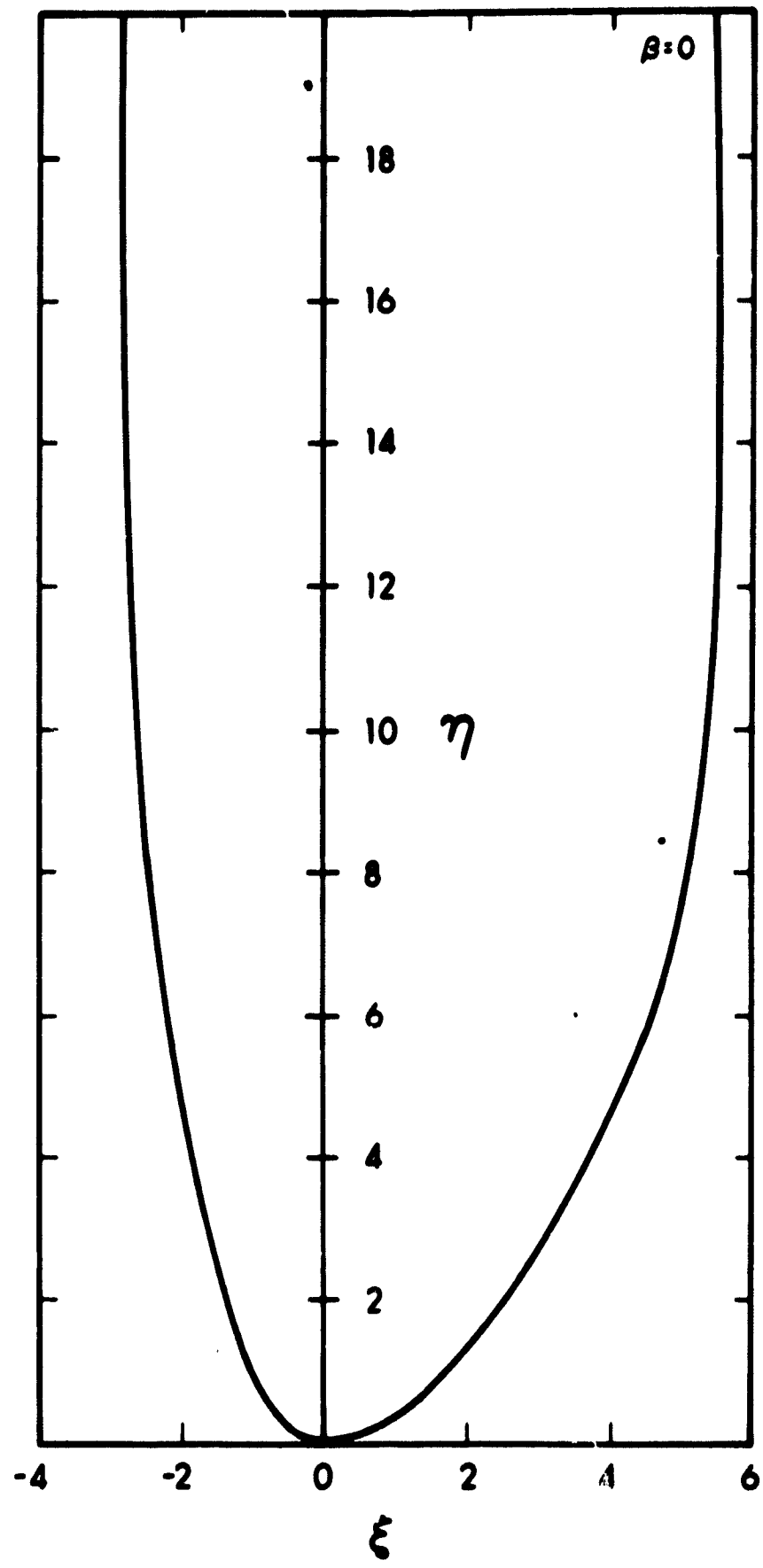

Figure 68. Normalized Potential, η, versus Normalized Distance, ξ, in the Interelectrode Space for $\beta = 0$ (β is defined in the text)

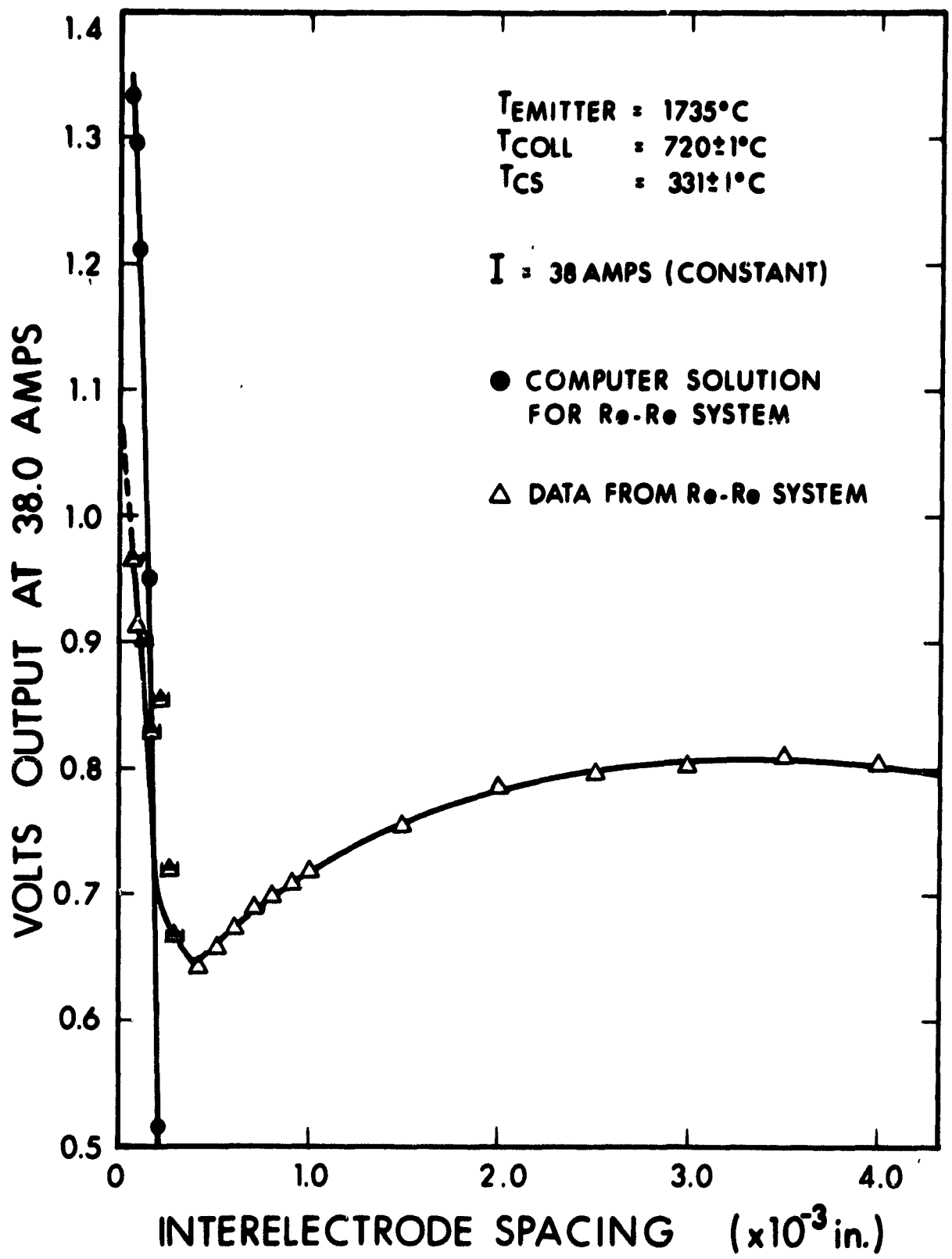

Figure 69. Comparison of Computed Results with Experimental Results

73627771

spacing, the higher the voltage output (the computed solution plot shows this), and (2) at spacings near 0.0005 inch there are probably sufficient collisions between electrons and cesium atoms to create positive ions which reduce the space change minimum. The experimental data indicate this by a reversal in the trend of decreasing voltage output; however, the computer solution has no provision for ions and predicts that less voltage output is available with increased spacing.

4.3 THE TRANSITION REGION

The region of interelectrode spacing between the plasma onset point and the point of maximum output is referred to as the transition region. It was noted in Subsection 4.2 that at spacings of about 0.5 mil , the formation of cesium ions is sufficient to initiate a conducting plasma. Since the exact processes of ionization in an arc-mode converter are unknown, the analysis of this region is most difficult. Qualitatively, therefore, as the spacing increases beyond 0.5 mil , more cesium vapor atoms are available for conversion to positive ions. The result is, for a constant current load, an increase in voltage output to a spacing whose value is determined by the 16-mil-torr relation. A further increase in spacing is subsequently offset by the phenomenon of resistance in the plasma to electron current flow.

4.4 THE POSITIVE COLUMN

In Region III the VPTV shows a decrease in output voltage at constant current as the spacing is increased. The output voltage falloff is a nearly linear function of spacing. The behavior is what might be expected if the increased spacing added length to the positive column with no other change taking place in the discharge.

The resistance of a number of curves taken as a function of spacing at constant current was measured in region III to learn something of the nature of the positive column.

The resistivity in region III was computed and the results are shown in Table XVII. There appears to be only weak dependence on emitter temperature or on the pressure of the cesium vapor. There is, however, a strong dependence of the resistance upon the current. The resistivity ranges from 0.8 ohm-cm at 7 A/cm^2 down to 0.2 ohm-cm at 48 A/cm^2. The cesium plasma pressures covered the range from 9.6 torr to 110 torr, and at a particular current setting the variations in resistivity are within the errors of measurement.

TABLE XVII

POSITIVE COLUMN "RESISTIVITY" VALUES

P_{Cs} (torr)	T_E (^oK)	T_{coll} (^oC)	Resistivity (ohm-cm)		
			7 A/cm^2	2.5 A/cm^2	48 A/cm^2
9.6	1715	750		0.30	
	1715	751	0.84		
17.2	1715	750	0.84	0.26	
	1715	750		0.25	
27.1	1810	750	0.78		
	1715	750	0.89		
	1715	750		0.21	
	1715	750	0.92		
41.0	1715	750		0.26	
	1810	750	0.76		
110	1515	950			0.19

REFERENCES

1. L. G. Schulz, J. App. Phys. 20, 1030-33 (1949)

2. B. D. Cullity, Elements of X-Ray Diffraction, Addison-Wesley, Reading, Mass. (1956)

3. H. F. Webster, (source and date not available)

4. H. J. Kostkowski and R. D. Lee, Theory and Methods of Optical Pyrometry, National Bureau of Standards Monograph 41, p. 24

5. W. Schottky, "Theory of Thermionic Emission," Physik, Z. 38 (1937)

6. E. Guth and C. J. Mullin, Phys. Rev. 59, 575 (1941)

7. E. A. Coomes and I. J. O'Haenens, The Use of Precise Schottky Data in the Analysis of the Metal-Vacuum Surface Barrier for Thermionic Emitters, I-Rhenium, Report AFCRL-67-0189, 1967

8. S. Kitrilakis, et al, Thermionic Research Program, Final Report JPL Contract 951262, Report TE 12-67

9. D. R. Koenig and T. H. Pigford, "Work-Function Depressions and Surface Ionization for Planar (100) Tungsten Exposed to Cesium," 26th Annual Conf., Physical Electronics, MIT, Cambridge, Mass., March 1966

10. H. Johannson, Ann. Phys. 18, 385 (1933) and 21, 274 (1934)

11. K. Spangenberg, Vacuum Tubes, McGraw-Hill, New York, 1948

12. A. O. Jensen, Research Program Related to Vapor Thermionic Converters for Nuclear Application, Electro-Optical Systems, Final Report, NASA Contract 3-2529

13. L. C. Lovell, J. H. Wemmick, "Dislocation Etch Pits and Polygonization in High Purity Copper," JAP, 30, 4, p. 390 (April 1959)

14. D. Schnek, Ann. der Phyzik (1935)

15. A. E. Campbell, High Performance Thermionic Converters, EOS Report 6952-Final, JPL Contract 951225, 2 Sept. 1966

REFERENCES (contd)

16. E. H. Kennard, Kinetic Theory of Gases, McGraw-Hill, New York, 1938

17. A. E. Campbell and A. O. Jensen, "Performance of Thermionic Converters," Thermionic Specialist Conference, Houston, Texas, Nov. 1966

18. Anthony F. Dugan, "Contribution of Anode Emission to Space Charge in Thermionic Power Converters," J. Appl. Phys. 31, 1397 (1960)

19. I. Langmuir, "The Effect of Space Charge and Initial Velocities on the Potential Distribution and Thermionic Current Between Plane Parallel Electrodes", Physical Review, Vol. XXI, No. 4, 19 April 1923.